

AD-A178 653

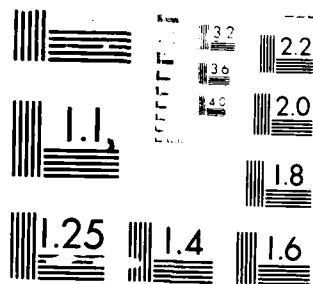
STRATEGIES FOR HIGH-RESOLUTION 3-D MILLIMETER WAVE
IMAGING(U) MOORE SCHOOL OF ELECTRICAL ENGINEERING
PHILADELPHIA PA ELECTR. N H FARHAT FEB 87 EO/NO-9
ARO-20583.13-EL DAAG29-83-K-0120 F/G 14/3

1/2

UNCLASSIFIED

NL





MICROCOPY RESOLUTION TEST CHART
NATIONAL BUREAU OF STANDARDS-1963-A

DTIC FILE COPY

ARO 20583.13-EL

②

AD-A178 653

FINAL REPORT

STRATEGIES FOR HIGH RESOLUTION
3-D MILLIMETER WAVE IMAGING



UNIVERSITY of PENNSYLVANIA
The Moore School of Electrical Engineering
PHILADELPHIA, PENNSYLVANIA 19104-6390

DTIC
ELECTE
APR 06 1987
S E

This document has been approved
for public release and wider its
distribution is unlimited.

87 1 165

2

UNIVERSITY OF PENNSYLVANIA
THE MOORE SCHOOL OF ELECTRICAL ENGINEERING
PHILADELPHIA, PA 19104

FINAL REPORT

STRATEGIES FOR HIGH RESOLUTION
3-D MILLIMETER WAVE IMAGING

PREPARED BY
N. H. FARHAT
FOR
US ARMY RESEARCH OFFICE

UNDER GRANT
DAAG-83-K-0120

FEBRUARY 1987

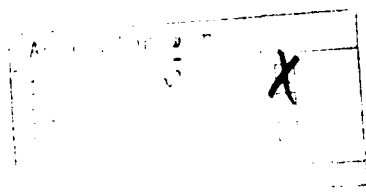
APPROVED FOR PUBLIC RELEASE
DISTRIBUTION UNLIMITED

E.O/MO-REPORT 9
PERIOD
8/15/83-12/31/86

UNCLASSIFIED

ABSTRACT - Continued

than being deliberately programmed to do so as was the case in our preceeding work. Stochastic learning algorithms and fast opto-electronic analog architectures and implementations based on simulated annealing in the context of a Boltzmann machine formalism are being studied. Work in this area is being vigorously pursued as it might have far reaching implications in smart sensing and recognition and artificial intelligence systems. Simulated annealing as an optimization process has also been found in our work to be very useful in phased-array antenna pattern synthesis.



A-1

UNCLASSIFIED

THE VIEW, OPINIONS, AND/OR FINDINGS CONTAINED IN THIS REPORT ARE THOSE OF THE AUTHOR(S) AND SHOULD NOT BE CONSTRUED AS AN OFFICIAL DEPARTMENT OF THE ARMY POSITION, POLICY, OR DECISION, UNLESS SO DESIGNATED BY OTHER DOCUMENTATION.

TABLE OF CONTENTS

	<u>Page</u>
Abstract	i
1. INTRODUCTION	1
2. SUMMARY OF IMPORTANT RESULTS	2
3. LIST OF PUBLICATIONS	16
4. PARTICIPATING SCIENTIFIC PERSONNEL AND ADVANCED DEGREES EARNED	20
5. APPENDICES	21
<p>I. Polarization Effects in Microwave Diversity Imaging of Perfectly Conducting Cylinders</p>	
<p>II. Microwave Diversity Imaging of Objects in the Presence of Severe Clutter</p>	
<p>III. A Multifunctional Microwave/Millimeter Wave Measurement Facility for Multistatic Imaging and Target Classification Studies</p>	
<p>IV. Optical Analogs of Two-Dimensional Neural Networks and Their Application in Recognition of Radar Targets.</p>	
<p>V. A new Iterative Algorithm for Extrapolation of Data Available in Multiple Restricted Regions with Applications to Radar Imaging</p>	
<p>VI. Architectures for Opto-Electronic Analogs of Neural Networks</p>	
<p>VII. Phased Array Antenna Pattern Synthesis by Simulated Annealing.</p>	

UNCLASSIFIED

SECURITY CLASSIFICATION OF THIS PAGE (When Data Entered)

REPORT DOCUMENTATION PAGE		READ INSTRUCTIONS BEFORE COMPLETING FORM	
1. REPORT NUMBER <u>ARO 20583.13-EL</u>	2. GOVT ACCESSION NO. N/A	3. RECIPIENT'S CATALOG NUMBER N/A	
4. TITLE (and Subtitle) STRATEGIES FOR HIGH-RESOLUTION 3-D MILLIMETER WAVE IMAGING		5. TYPE OF REPORT & PERIOD COVERED <u>15 Aug 83 - 31 Oct 86</u> Final	
		6. PERFORMING ORG. REPORT NUMBER EO/MO 9	
7. AUTHOR(s) Nabil H. Farhat		8. CONTRACT OR GRANT NUMBER(s) DAAG29-83-K-0120	
9. PERFORMING ORGANIZATION NAME AND ADDRESS University of Pennsylvania 200 South 33rd Street Philadelphia, PA 19104		10. PROGRAM ELEMENT, PROJECT, TASK AREA & WORK UNIT NUMBERS	
11. CONTROLLING OFFICE NAME AND ADDRESS U. S. Army Research Office Post Office Box 12211 <u>Research Triangle Park, NC 27709</u>		12. REPORT DATE February 1987	
14. MONITORING AGENCY NAME & ADDRESS (if different from Controlling Office)		13. NUMBER OF PAGES 156	
		15. SECURITY CLASS. (of this report) Unclassified	
		15a. DECLASSIFICATION/DOWNGRADING SCHEDULE	
16. DISTRIBUTION STATEMENT (of this Report) Approved for public release; distribution unlimited.			
17. DISTRIBUTION STATEMENT (of the abstract entered in Block 20, if different from Report) NA			
18. SUPPLEMENTARY NOTES The view, opinions, and/or findings contained in this report are those of the author(s) and should not be construed as an official Department of the Army position, policy, or decision, unless so designated by other documentation.			
19. KEY WORDS (Continue on reverse side if necessary and identify by block number) microwave and millimeter wave diversity imaging, target derived reference, image symmetrization, inverse SAR, spot-light imaging mode, super-resolution, sinogram representation, hetero-associative memory, neural networks, collective processing, electromagnetic similitude, self-organization and learning, simulated annealing, Boltzmann machine.			
20. ABSTRACT (Continue on reverse side if necessary and identify by block number) Two strategies or approaches to millimeter wave (mmw) microwave (mw) imaging and recognition are investigated. One approach seeks to produce cost-effective high resolution images of scattering targets and scenes that would resemble as closely as possible their more familiar visual images and therefore can be readily recognized and interpreted by a minimally trained observer. In this approach we have extensively studied the principles and methodologies of a 3-D tomographic mw/mmwave diversity imaging where angular, spectral, and			

UNCLASSIFIED

SECURITY CLASSIFICATION OF THIS PAGE(When Data Entered)

polarization degrees of freedom are combined for efficient imaging of remote scattering objects. This work has lead to images with unprecedented quality with near optical resolution employing a unique experimental microwave imaging facility. At such high resolution, image artifact produced by clutter and multiple reflections on the target can be detrimental as these and specially the latter can make the $\mu\text{w}/\text{mmw}$ image depart noticeably in appearance from the visual image in that ghost detail not corresponding to any physical detail on the target can emerge. For this purpose we have conducted a study of the effect of background clutter and multiple reflections on image quality. It was found that $\mu\text{w}/\text{mmw}$ images can be separated from "ground" or clutter provided that adequate range resolution is available. Artefact caused by multiple reflections is found to be highly dependent on polarization and can be minimized through proper choice of polarization of the transmitting and receiving antenna i.e., by polarization discrimination.

Resolution in $\mu\text{w}/\text{mmw}$ diversity imaging is propositional, among other things, to the width of the spectral window over which data is acquired. Very wide spectral windows can in principle yield images of remote targets e.g., aerospace targets with better than optical resolution. The use of such extended spectral range is not possible in practice because of equipment limitation, frequency band allocation, and atmospheric propagation. It is possible however to conduct measurements over separate segments of an extended spectral range. For this reason a new iterative algorithm for extrapolation of data available in multiple segmented regions covering an extended spectral range has been developed. For objects with discrete scattering centers the algorithm is shown to furnish images with quality equal to the image obtained had the data been collected continuously over the entire extended spectral range. This result has obvious practical implications in that hardware complexity is traded by cheaper and more readily available computational expenditure. At the same time limitations imposed by frequency allocation and atmospheric effects are cleverly bypassed.

The second approach to $\mu\text{w}/\text{mmw}$ target identification is based on machine recognition where no explicit image formation takes place. This approach developed more recently in our research as a result of research in neural net models and their analogs as a new robust, high-speed, and fault tolerant approach to signal processing. A research effort in radar target recognition from partial information based on neural net models and their opto-electronic implementation has been initiated. Sinogram representations of targets of interest are considered as learning sets. The basic assumption here is that sinogram representations and other kinds of signatures, e.g. polarization maps, of scale models of targets of interest can be generated cost-effectively in our anechoic chamber facility to serve as learning sets for a neural processor that can be subsequently used in the recognition of the actual radar targets from few echoes collected by broad-band tracking systems. Careful attention is being given to scaling questions and to the principle of electromagnetic similitude in order to make the "laboratory" generated representations as realistic as possible and therefore useful in the recognition of echoes obtained by any broad-band radar installation. Preliminary results show that a neural net processor is capable of distinguishing between models of three aero-space objects from a few looks on each corresponding to 10 to 20 percent of their corresponding sinogram representations. The neural net processor in this work performed the function of information storage, processing, and labeling of the target recognized simultaneously. Current work is considering the question of self-organization and learning in neural nets as a means for the net to generate its own representations of the items it is supposed to become familiar with rather

UNCLASSIFIED

SECURITY CLASSIFICATION OF THIS PAGE(When Data Entered)

STRATEGIES FOR HIGH-RESOLUTION 3-D MILLIMETER WAVE IMAGING

1. INTRODUCTION

The ultimate aim of active microwave (μ w) and millimeter wave (mmw) imaging systems is recognition and identification of the scattering body or scene under illumination. Examples are found in target identification and classification by ISAR (inverse synthetic aperture radar) and scene analysis in SAR (synthetic aperture radar). Our research under this grant followed two approaches to the problem of target imaging and identification. One is the more traditional approach of producing images intended for recognition by a human observer. Here we are concerned with cost-effective methodologies for imparting to the images formed the possible highest-resolution in order to provide them with near optical quality that makes them easy to recognize or analyze by a human observer. Therefore μ w/mmwave image, acquisition, formation, understanding, and interpretation are of primary concern. The second approach, which emerged later in the course of our research, is less traditional involving automated machine recognition. Here we are concerned with issues of correct recognition from partial or sketchy information and systems that can do this in a robust and fault tolerant manner. In this approach the role of the eye-brain system in recognizing an image is mimicked by the machine making the recognition process "brain-like" in nature. The approach is based on neural net models and their opto-electronic analogs which exploits the fit between what optics can offer (parallelism and massive interconnectivity) and what neural net models can offer (new approach to signal processing that is nonlinear and collective and therefore fast, robust, and fault tolerant). The two approaches are coupled in that automated

machine recognition with artificial neural networks relies on the generation of target or object representations or feature spaces that can lead to "distortion tolerant" recognition i.e., recognition irrespective of target range, orientation, or location within the field of view traditionally referred to as scale, rotation, and shift invariant recognition. The generation of such representations usually involves the same gear employed in traditional μ w/mmwave diversity imaging where spectral, angular, and polarization degrees of freedom are combined to realize images of the scattering targets with near optical resolution. In fact the presentations or feature spaces often contain exactly the same information contained in a μ w/mmwave image of the target except it is arranged in a slightly different format that is more amenable for use in automated recognition schemes. This dual approach has lead to the emergence of a new concept of achieving ultimate resolution through correct recognition of the target by a machine. In other words correct recognition of the target by a machine can be interpreted as equivalent to realizing a very high resolution image with detail sufficient for reliable recognition and even discrimination between closely similar targets by the eye-brain system. Our research findings, presented next, fall within one or the other of these two approaches.

2. IMPORTANT RESEARCH FINDINGS

One facet of our research during the period of this final report has focused on investigating methods that enable the formation of the highest resolution microwave and millimeter wave images of scattering bodies cost-effectively. At such high resolutions, the effect of multiple scattering in images of complex shaped scattering objects become particularly important as an image degrading mechanism or as an effect whose proper understanding and

interpretation can convey additional information about the object. The effect of multiple scattering is to impose on the microwave image artefact or detail that makes it depart from the visually expected "optical" image making it, in some instances, less readily recognized or interpreted by the human observer. For this reason, a systematic theoretical and experimental study of multiple scattering effects in the imaging of simple bodies e.g., consisting of two conducting or dielectric cylinders and the role played by polarization in such effects was conducted (See Appendix I for details). This study of multiple scattering effects between cylinders explained well the artefacts observed in earlier imaging experiments of such objects and their dependence on polarization of the illuminating and receiving antennas. The advantage of using circularly polarized illumination and cross-polarized illuminating and receiving antennas to suppress such artefacts is demonstrated. This work also illustrates dramatically the power of microwave diversity imaging techniques as a tool in the study and understanding of electromagnetic scattering.

Another task studied during the period of this report is evaluation of the capabilities of microwave diversity imaging in the formation of recognizable images in the presence of severe background clutter. This problem is important for certain modalities of radar imaging such as close-range millimeter wave imaging of ground vehicles, space-borne imaging of low-flying aircraft employing a "spot-light" imaging mode, and imaging of internal structure of penetrable dielectric bodies in the presence of strong surface reflections. Details and results of this study are given in Appendix II. There, a projection image of the visible scattering centers of a test object, a 72:1 metalized scale model of the space shuttle, was obtained employing a spectral window of 11 GHz (6.1-17.5 GHz) and an angular window of 90° . The shuttle model was imaged when situated 40 cm above corrugated aluminum ground

planes of different roughness to simulate ground clutter from different terrain. Excellent polarization enhanced images of the target shape, clearly delineated above the image of the ground plane were obtained. These compare very well with flood-lit side-view photographs of the configuration showing the silhouette of the object. The results clearly demonstrate the advantages of using extended spectral and angular windows in this mode of imaging.

Research at the Electro-Optics and Microwave-Optics Laboratory has led over the past decade to the inception and development of **microwave diversity imaging** where angular spectral, and polarization degrees of freedom are combined to form the highest resolution images of complex shaped objects reported to date anywhere. An example is seen in the near-optical resolution image shown in Fig. 1. This is a projection image of the visible scattering centers on a B-52 test object. Copolarized and cross-polarized data sets, each consisting of 128 azimuthal looks at the target extending from head-on to broad-side and at an elevation angle of 30° with each look containing 128 complex frequency points covering a (6-17) GHz spectral window were utilized

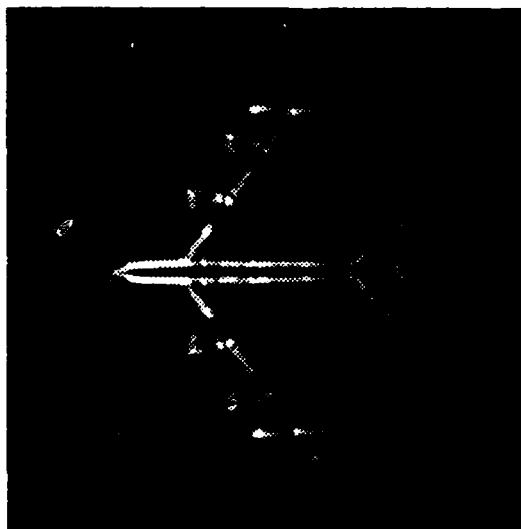


Fig. 1. Examples of Microwave diversity projection image of 100:1 scale model of a B-52. Horizontal streaks are artefacts of the back-projection image reconstruction algorithm utilized.

in obtaining the example shown. Also a novel **target derived reference** technique for correcting the data for undesirable range-phase (or range-phase time-rate (Doppler) when the target is moving) together with an **image symmetrization** method were conceived and painstakingly developed and perfected before the image quality shown could be obtained.

The image of Fig. 1 clearly shows the double-barreled nature of the engines on the B-52. The image was obtained with a new upgraded measurement system described in detail in Appendix III employing a spectral window of (6-17) GHz. This spectral range was chosen to enable comparison with earlier results. The improved accuracy and wider dynamic range of the upgraded system are seen to bring out detail that could not be observed in earlier images (see Fig. 2) obtained employing the original measurement system and the same spectral window. Comparison of the images in Figs. 1 and 2 shows quickly that the back edges of the wings and the tail are now clearly visible primarily due to the wider dynamic range of the measurement system and the laser printer

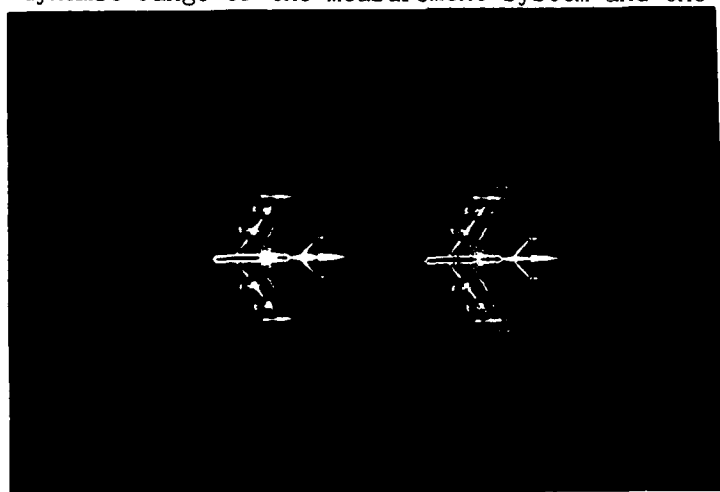


Fig. 2. Microwave diversity projection images of 100:1 scale model of a B-52 obtained with the original measurement system. Unfiltered image (left), filtered image (right).

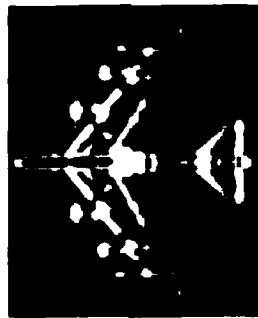
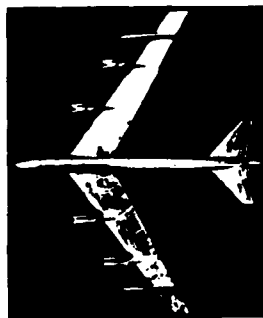
used to record the image of Fig. 1.

Application of the concepts and methodologies developed and demonstrated in this research in practice would entail: either (a) the use of large, albeit highly thinned (sparse), recording imaging apertures to furnish the angular diversity needed or (b) the use of a single radar system that can track and interrogate a moving target from different aspect angles in time as the target changes its orientation relative to the radar system line of sight while it moves to furnish the required angular diversity in an **inverse synthetic aperture radar (ISAR)** or **spot-light imaging mode**. The first approach is prohibitively costly specially when the target is remote and the angular aperture needed to achieve useful resolution is large. The second approach is non-real-time as it requires observing the target over a period of time, that may not be acceptable in many applications, in order to synthesize an adequate angular apertures over a limited observation time and therefore one is faced with the problem of image formation and signal recovery from limited and often sketchy information, i.e., one is faced with the classical problem of **super-resolution** which has evaded general solution until now. In other words, the problem is to recognize the target from a few looks.

More recently in our research progress towards a solution to this problem employing collective robust and fault tolerant processing based on models of neural network has been achieved. Among its many fascinating capabilities such as robustness and fault tolerance, the brain is also able to recognize objects from partial information. We can recognize a partially obscured or shadowed face of an acquaintance or a mutilated photograph of someone we know with little difficulty. The brain has a knack for supplementing missing information. Capitalizing on this feature and on our knowledge of neural models and their collective computational properties, (see 6 and 7 of list of publications) a study of "neural processing" for recognizing objects from

partial information has been initiated. An example of the capabilities of this new and intriguing approach in automated recognition and labeling of radar targets from partial information is given in Fig. 3. Details of this preliminary work is given in Appendix IV.

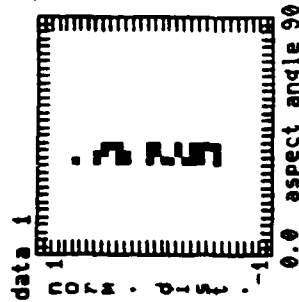
Object recognition employing hetero-associative memory based on models of neural networks may obviate the need for expensive or non real-time image formation in the field. Images of scale models of objects of interest and their **sinogram representations** are produced indoors in our microwave imaging facility at a fraction of the cost of an actual radar system operating to form images of actual targets intended for recognition by the eye-brain system. (See Appendix IV). The sinogram representations which can be viewed also as signatures or feature-spaces of targets of interest are taught to a **hetero-associative memory** by associating them with identifying letter labels. When such a hetero-associative memory is presented with partial sinogram information, that can be as low as 10% of the full sinogram, the memory will supplement the missing information and produce the correct label. This ability of supplementing missing information is synonymous with "super resolution". It is akin to our ability for example to recognize a photograph of someone we know even when part of it is missing or to understand a sentence in a handwritten letter even when some of the words are not legible. Partial sinogram information can be produced much more rapidly, easily, and economically in the field by actual radar systems than producing full sinogram or image. Thus a few looks at the target from slightly different aspects may be sufficient for recognition. The real challenge is to recognize



OPTICAL IMAGE (TOP) AND
RADAR IMAGE (BOTTOM) OF
SCALE MODEL OF B-52 AIR-
CRAFT PRODUCED AT THE
EXPERIMENTAL MICROWAVE
IMAGING FACILITY OF
THE UNIVERSITY OF
PENNSYLVANIA



(TOP) DIGITIZED SINOGRAM
REPRESENTATION OR SIGNA-
TURE OF B-52 TAUGHT WITH
OTHER SINOGRAMS (OF AN
AWAC AND A SPACE-SHUTTLE)
TO A HETERO-ASSOCIATIVE
MEMORY BASED ON MODELS
OF NEURAL NETS. (BOTTOM)
CORRECT LABEL PRODUCED
BY MEMORY WHEN IT WAS
PRESENTED WITH A COMPLETE
SINOGRAM OF THE B-52
SIGNIFYING THEREBY
RECOGNITION



SAME CORRECT LABEL OF
B-52 (BOTTOM) WAS PRODUCED
BY MEMORY WHEN PRE-
SENTED WITH PARTIAL SINO-
GRAM INFORMATION (10% OF
THE SINOGRAM REPRESENTA-
TION (TOP)).

Fig. 3. Example of automated recognition of radar target employing hetero-associative memory based on models of neural network.

the target from one look i.e., from one broadband radar echo and for non-aerospace targets in the presence of clutter. The achievement of this aim employing artificial neural processors is a major objective of our future research. It is important to note that, unlike a conventional memory in a computer, the hetero-associative memory here performs the functions of storage, processing, and recognition simultaneously. As such it is more correct to regard it as a "neural processor". A primary objective of our future research in this area is the generation of realistic target representation employing scale models in an anechoic chamber environment. Careful consideration of scaling issues and of the principle of electromagnetic similitude* are called for in order to be able to generate from scale models feature spaces (e.g., sinogram representations) that resemble those obtained had the real object been interrogated by a realistic broad-band radar system.

Resolution in $\mu\text{w}/\text{mmw}$ diversity imaging depends among other things on the width of the available spectral window. Extended spectral windows covering the μw and portions of the mmw range can lead to resolution on remote targets (e.g., aerospace targets) exceeding those of optical systems which are more susceptible to atmospheric effects than $\mu\text{w}/\text{mmw}$ imaging systems. Hardware and frequency band allocation limit however data acquisition in practice to non-overlapping bands that can cover a wide spectral range. The question then is how to employ information collected in such multiple restricted frequency bands to retrieve an image of the target equivalent or approaching that obtained had the entire spectral range been available by extrapolation into the missing bands.

* J.D. Stratton, Electromagnetic Theory, McGraw Hill, New York (1941), pp. 488-490.

A new iterative method for extrapolation of incomplete segmented data available in multiple separated bands has therefore been proposed and tested. The method uses the Burg algorithm to find the linear prediction parameters and an iterative procedure to improve the estimation of the linear prediction parameters and the extrapolation of the data. This method is especially effective when the spectra (Fourier transform of the observed data) are in discrete forms. In the context of radar imaging represented here, this means the objects consist of discrete or distinctly spaced scattering centers. The advantage of this algorithm were demonstrated using both numerically generated and realistic experimental data pertaining to high resolution radar imaging. Detail of this work is given in Appendix IV.

Our research during this period examined also several approaches to the problem of accessing the 3-D Fourier space of a scattering body undergoing irrotational motion. The criterion for selecting the best approach were speed, accuracy and economy. The method chosen, shown in Fig. 4, exploits recent advances in the state-of-the-art of Microwave instrumentation to enable the study of innovative and efficient approaches to data acquisition that were generally thought not to be feasible a short time ago. The scheme utilizes two capabilities of current microwave instrumentation. High speed computer controlled frequency synthesis and high-speed frequency measurement. These capabilities are combined in the arrangement shown to realize rapid determination of the doppler shift F_D in the signal scattered from the moving scatterer (target) which can then be compensated for in the phase and amplitude measurement of the scattered field carried out by the coherent receiver (hp 8410B Network Analyzer) whose intermediate local oscillator is effectively made to equal $F_{RF} + F_D$ by using an externally synthesized signal

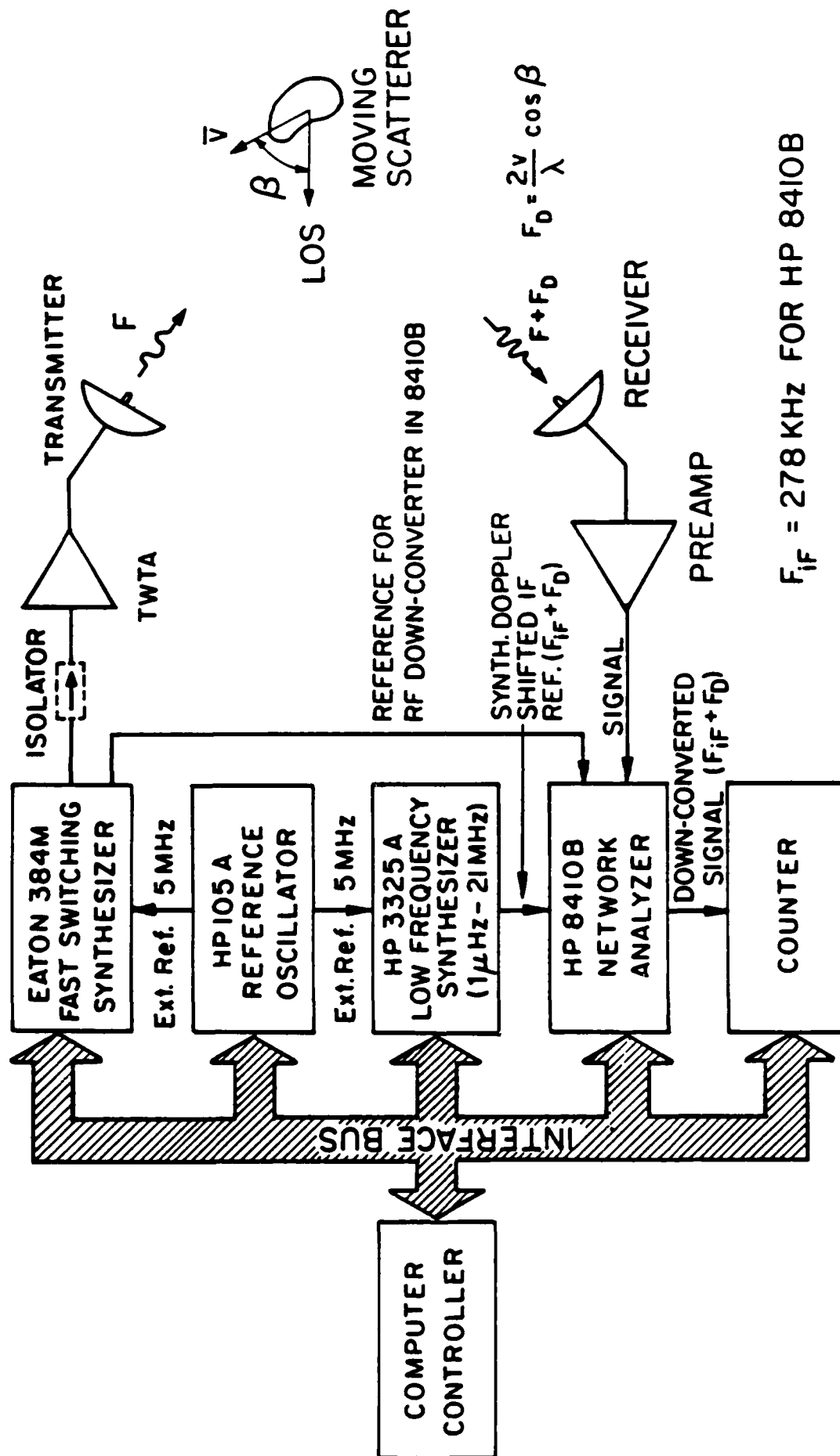


Fig. 4. Doppler compensated arrangement for measuring the stepped frequency response of a moving scatterer.

at frequency $F_{IF} + F_D$ for the reference IF channel of the network analyzer. This eliminates the effect of Doppler shift on the phase measurement and provides data very much similar to that generated had the target been stationary and it merely changes its aspect relative to the line of sight of the interrogating radar system. Note the low frequency synthesizer source of the $F_{if} + F_D$ signal, the hp 3325A synthesizer, is phase-locked to the RF source of illumination of the target. This synthesized source has been carefully chosen because its high frequency resolution which enables setting the doppler shift of the IF reference precisely to the measured value of F_D . This frequency resolution is necessary because any discrepancy between the intermediate frequency (IF) reference signal and the down converted IF version of the target echo signal in the network analyzer results in an undesirable time varying phase error. In this arrangement the complex frequency response of the moving scatterer is measured rapidly in discrete frequency steps following the determination of the doppler shift and the setting of the low frequency intermediate frequency reference synthesizer to $(F_{IF} + F_D)$. If we assume that 100 frequency stepped measurements per second, as limited by the bandwidth of the phase/amplitude measuring segment of the network analyzer, can be performed, then the Doppler shift during this interval is expected to change negligibly for most practical targets including aerospace targets. Therefore the Doppler measurement and doppler compensation operations need not be performed frequently by the system but only occasionally or at most once at the beginning of each digital frequency sweep.

All the instrumentation to verify this scheme is now available in our laboratory with the exception of the hp 3325A low frequency synthesizer. In the next phase of this research we plan to either purchase or lease this

instrument in order to carry out this experiment either with an actual moving target as depicted in Fig. 4 or by means of a more attractive and less costly (no movement of any scatterers are needed) signal simulation method in which the backscatter from a stationary target can be effectively doppler shifted by using two phase-locked fast switching synthesizers one for illuminating the stationary target with a signal $F_{RF} + F_D$ and one for furnishing an RF reference of frequency F_{RF} to the coherent receiver (network analyzer). Since in this case the synthesized Doppler shift and hence the equivalent target velocity is under our control the time scale of the measurement can be increased. In that case we plan to use an available (.05-26.5) GHz microwave synthesizer of conventional speed to furnish the RF reference frequency. The effective doppler shift in the stationary object illumination can be programmed during frequency stepping to simulate any object motion law. Furthermore computer controlled versatile phase and frequency modulations capabilities of the Eaton synthesizer, used to produce the target illumination, will also enable the simulation and study of the effect of doppler broadening in the target echo as a result of vibrations and slight relative periodic and nonperiodic motion amongst the different parts of a complex shaped rigid but flexing target such as an aircraft for example whose linear motion is distorted by wind buffeting and mechanical resonances. This signal simulation scheme may provide a cost-effective means for the study of microwave diversity imaging and identification of moving target since stationary scale models of the actual target can be used instead of actual targets in flight reducing the incurred cost and facilitating significantly the execution of the study. For this reason work on removing the effect of phase ambiguity when two or more oscillators are repeatedly phase locked after altering their frequency is in progress.

In one of the preceeding research tasks, the smart sensing capabilities of our μ w/mmW diversity imaging approach were exploited to generate target representations (sinogram representations or feature spaces) which were used in turn to compute the synaptic connectivity matrix of the neural net processor. This operation is equivalent to deliberate programming of the neural net processor to perform certain pattern recognition task. One of the most intriguing and potentially useful properties of neural nets is that of self-organization and learning where the net can form its own internal representations of the associations it is presented with by internally altering the weights of interconnections between its neurons in accordance to some learning algorithm. We have initiated a study of **self-organization** and learning particularly in opto-electronic analogs of neural nets where synaptic modification is assumed to be realizable by means of programmable spatial light modulators (SLMS). Stochastic learning through a simulated annealing process in the context of a **Boltzmann machine** is considered. An architecture for partitioning the "neurons" in an opto-electronic analog of a neural net into groups or layers to enable stochastic self-organization and learning has been arrived at and is described in some detail in Appendix VI. We envision this work will lead to neural net processors that learn by example. Such processors can be very useful in many applications of interest to the Army Research Office. It is our belief that self-organization and learning is one of the most intriguing properties of neural net processing. It is one of their attributes that sets them apart from other approaches to signal processing. It can play an important role in the development of smart sensing, artificial intelligence, and high-speed knowledge processing systems.

Simulated annealing is known to be an effective tool in the solution of combinatorial optimization problems where an "energy" or "cost" function is to

be minimized as a means of finding a solution. It has been applied in the solution of a wide range of combinatorial optimization problems. We have found recently that it can also be an effective tool in phased array antenna design where simulated annealing is applied to determine the binary (+1,-1) weights of the phase array elements that yield an optimal radiation pattern as far as beamwidth and side-lobe level are concerned. Detail of this work is given in Appendix V.

3. LIST OF PUBLICATIONS

Journal and Conference Proceeding Publications:

1. N.H. Farhat, "Projection Imaging of 3-D Microwave Scatterers with Near Optical Resolution", in Indirect Imaging, J.A. Roberts (Ed.), Cambridge University Press (1984).
2. N.H. Farhat, C.L. Werner, and T.H. Chu, "Prospects for Three-Dimensional Projective and Tomographic Imaging Radar Networks", Radio Science, Vol. 19, September-October, 1984, p. 1347-1355.
3. N. Farhat, C.L. Werner and T.H. Chu, "Prospects for 3-D Tomographic Imaging Radar Networks", Proc. URSI Symp. on Electro-Magnetic Theory, Santiago De Compostela, Aug. 1983, pp. 279-301.
4. D.L. Jaggard and A.K. Jordan, "Inversion Theory for Almost Periodic Media", Radio Science, Vol. 19, September-October, 1984, pp. 1333-1341.
5. N.H. Farhat, et. al., "Optical Implementation of the Hopfield Model", Applied Optics, Vol. 24, May 1985, pp. 1469-1475.
6. N. Farhat and T.H. Chu, "Tomography and Inverse Scattering," Proc. ICO-13, 13th Congress of the International Commission on Optics, Sapporo, Japan, 1984.
7. N.H. Farhat, et. al., "Optical Implementation of the Hopfield Model", Applied Optics, Vol. 24, May 1985, pp. 1469-1475.
8. D. Jaggard and Y. Kim, "Accurate One-Dimensional Inverse Scattering Using Nonlinear Renormalization Technique", J. Opt. Soc., Part A, Vol. 2, 1985
9. D.L. Jaggard and K.e. Olson, "Numerical Reconstruction for Dispersionless Refractive Profiles", J. Opt. Soc., Part A, Vol. 2, Oct. 1985.
10. Y. Kim and D.L. Jaggard, "Inverse Blackbody Radiation: An Exact Closed-Form Solution", IEEE Trans. Antenna and Prop., Vol. AP-33, July. 1985. pp. 797-800
11. D. Psaltis and N. Farhat, "A New Approach to Optical Information Processing Based on the Hopfield Model", 13-th Congress of the International Commission on Optics, ICO-13, Conference Digest pp. 24-25, Published by the Organizing Committee of ICO-13, Sapporo, Printed in Japan SML 8408, 1984.
12. N. Farhat, et. al., "Optical Analog of Two-Dimensional Neural Networks and Their Application in Recognition of Radar Targets", In Neural Networks and Computing, J.S. Denker (Ed.), Am. Inst. of Phys., New York, 1986, pp. 146-152.
13. N. Farhat, "Robust Signal Recovery and Recognition with Optical Analogs of Neural Nets and Spurious Memory Discrimination", SPIE Vol. 700, 1986, pp. 283-288.

14. T.H. Chu and N. Farhat, "Polarization Effects in Microwave Diversity Imaging of Perfectly Conducting Cylinders", IEEE Transactions on Antennas and Propagation, Accepted for publication.
15. H-J Li and N. Farhat, "A New Iterative Algorithm for Extrapolation of Data Available in Multiple Restricted Regions with Application to Radar Imaging", IEEE Trans. on Antennas and Propagation, Accepted for publication.
16. N. Farhat and B. Bai, "Phased Array Pattern Synthesis by Simulated Annealing", Proc. IEEE (Letters), Accepted for publication.

Conference Presentations

1. N.H. Farhat and T.H. Chu, "Tomography and Inverse Scattering" in Optics in Modern Science and Technology, Proc. ICO-13, Sapporo, Japan, Aug. 1984, pp. 62-63.
2. D.L. Jaggard, et. al., "Tomographic Microwave Imaging", XXI General Assembly of the International Union of Radio Science, Florence, Italy, August-September 1984.
3. D. Psaltis and N. Farhat, "A New Approach to Optical Information Processing Based on the Hopfield Model", 13-th Congress of the International Commission on Optics, ICO-13, Sapporo, Japan.
4. N. Farhat and D. Psaltis, "Optical Implementation of the Hopfield Model", OSA Annual Meeting, San Diego, Oct. 1984.
5. D. Psaltis and N. Farhat, "Optical Computing Based on the Hopfield Model", OSA Topical Meeting on Optical Computing, Lake Tahoe, March 1985.
6. N. Farhat and D. Psaltis, "Opto-Electronic Implementations of the Hopfield Model", OSA Topical Meeting on Optical Computing, Lake Tahoe, March 1985.
7. N. Farhat and Y. Shen, "Microwave Imaging of Objects in the Presence of Severe Clutter", OSA Annual Meeting, Wash. D.C., 1985.
8. N. Farhat, et. al., "High Speed Fourier Camera", OSA Annual Meeting, Wash. D.C., 1985.
9. K.S. Lee and N. Farhat, "Content Addressable Memory with Smooth Transition and Adaptive Thresholding", OSA Annual Meeting, Wash. D.C., 1985.
10. N.H. Farhat and D. Psaltis, "Architectures for Optical Implementation of 2-D Content Addressable Memories", OSA Annual Meeting, Wash. D.C., 1985.
11. N.H. Farhat, T.H. Chu, C.L. Werner and Y. Shen, "Microwave Diversity Imaging with Near Optical Resolution", IEEE AP-S/URSI Meeting, Phila., 1986.

12. T.H. Chu and N. Farhat, "Multiple-Scattering Effects in Microwave Diversity Imaging", IEEE AP-S/URSI Meeting, Phila. 1986.
13. N.H. Farhat and S. Miyahara, "Super-Resolved Target Recognition and Classification Based on Models of Neural Networks", IEEE AP-S/URSI Meeting, Phila., 1986.
14. N.H. Farhat and Y. Shen, "Microwave Diversity Imaging of Objects in the Presence of Severe Clutter", IEEE AP-S/URSI Meeting, Phila., 1986.
15. C.L. Werner and N.H. Farhat, "Tomographic Imaging of 3-D Incoherent Objects Employing Spectrally Selective Correlation Measurements", IEEE AP-S/URSI Meeting, Phila., 1986.
16. N.H. Farhat, Y-J Li and Y. Shen, "Radar Cross-Section Management Studies Employing Microwave Diversity Imaging", IEEE AP-S/URSI Meeting, Phila., 1986.

Invited Talks

During the period of this report the following invited presentations to DARPA Army Laboratory personnel were made by N. Farhat:

1. "Microwave Diversity Imaging and Automated Recognition," presented at the Reconnaissance, Surveillance and Target Acquisition (RSTA) SYMPOSIUM HELD AT THE HARRY DIAMOND LABORATORIES, ADELPHI, MD, JAN. (28-30) 1986.
2. "Optical Analogs of Neural Nets and their Potential Applications", informal briefing, U.S. Army Research Office, Research Triangle Park, N.C., March 17, 1986.
3. N. Farhat, "Neural Networks and Optical Computing", DARPA Briefing, April 1985.

Also the following invited talks and seminars were presented by N. Farhat.

4. "Radar Imaging" California Inst. of Technology, Pasadena, Oct. 1984.
5. "3-D Tomographic Imaging Radar", General Dynamic, Ft. Worth Division, Ft. Worth Texas, Oct. 26, 1984. A video cassette recording of this lecture has been furnished courtesy of General Dynamics. A copy of this video tape was furnished to ARO with our Progress Report covering the period 1 July 1984 to 31 December 1984.
6. "Smart Sensing and Recognition", Jet Prop. Laboratory, Pasadena, Aug. 1985.

7. "Tomographic Radar Imaging with Near Optical Resolution", Drexel University, Jan. 1986.
8. "Tomographic Radar Imaging", AT&T Technology Systems and Bell Laboratories National Engineering Week Lecture Series, Reading, PA, Feb. 1985.
9. "Optical Processing for 3-D Tomographic Imaging Radar", Sigma Xi Initiation Dinner, Bucknell, Univ., March 1985.
10. "Optical Computing Implementation for Neural Processing in the Eye-Brain System", Computer chapter, IEEE, N.J., Coast Section Seminar, 1985.
11. "Optical Implementation of Neural Nets", Workshop on Neural Networks for Computing, Santa Barbara, May, 1985.
12. "Neural Nets and Their Applications", Jet Propulsion Laboratory, Aug. 1986.
13. "Microwave Diversity Imaging and Automated Target Recognition", Univ. of California, Elect. Engrg. Dept., Feb. 1986.
14. "Smart Sensing and Image Recognition Based on Models of Neural Networks", AT&T Bell Communications Research Seminar, Feb. 1986.

N. Farhat has been invited to participate in the NATO Advanced Study Institute on "EM Modelling and Measurements for Analysis and Synthesis Problem" to be held Aug. 1987 in Il Ciocco, Italy where he will lecture on "Microwave Diversity Imaging and Automated Target Recognition."

4. PARTICIPATING SCIENTIFIC PERSONNEL AND LIST OF DEGREES AWARDED;

N.H. Farhat - Principal Investigator
D.L. Jaggard - Co-Investigator
K.S. Lee - Graduate Student (50%)
P. Frangos - Graduate Student (50%)
Y. Shen - Graduate Student (50%)
K. Schultz - Graduate Student (50%)
S. Miyahara - Graduate Student (self-supported)
C.L. Werner - Graduate Student (self-supported)

The following degrees were awarded during the period of this report:

- P. Frangos (Ph.D.) - "One-Dimensional Inverse Scattering: Exact Methods and Applications",
- C.L. Werner (Ph.D.) - "3-D Imaging of Coherent and Incoherent Sources Utilizing Wave-vector Diversity",
- S. Miyahara (Ph.D.) - "Automated Radar Target Recognition Based on Models of Neural Networks",

The following graduate students are in the last stages of completing their Ph.D. dissertations:

- K.S. Lee, "Smart Sensing and Recognition" (manuscript near completion)
- Y. Shen (Ph.D.), "Dynamic Microwave Imaging", (manuscript near completion).

5. APPENDICES

- I. Polarization Effects in Microwave Diversity Imaging of Perfectly Conducting Cylinders.
- II. Microwave Diversity Imaging of Objects in the Presence of Severe Clutter.
- III. A Multifunctional Microwave/Millimeter Wave Measurement Facility for Multistatic Imaging and Target Classification Studies.
- IV. Optical Analogs of Two-Dimensional Neural Networks and their Application in Recognition of Radar Targets.
- V. A New Iterative Algorithm for Extrapolation of Data Available in Multiple Restricted Regions with Applications to Radar Imaging.
- VI. Architectures for Opto-Electronic Analogs of Neural Networks.
- VII. Phased Array Antenna Pattern Synthesis by Simulated Annealing.

APPENDIX I

POLARIZATION EFFECTS IN MICROWAVE DIVERSITY IMAGING
OF PERFECTLY CONDUCTING CYLINDERS

Tah-Hsiung Chu
RCA David Sarnoff Research
Center
Rm 3-231, P.O. Box 432
Princeton, NJ 08540

Nabil H. Farhat
University of Pennsylvania
The Moore School of Electrical
Engineering
200 S. 33rd Street
Philadelphia, PA 19104

ABSTRACT

A theoretical vector development of the directly and mutually scattered wavefield of two cylinders in a bistatic measuring system is presented. The two scattered fields are shown to be polarization dependent, the images reconstructed from the directly or mutually scattered far field of each polarization include different features of the scattering object. An automated microwave imaging system employing frequency, polarization, and angular diversity is utilized to verify the theoretical results. Analytical and experimental results are shown to be in good agreement. The polarization effects of multiscatterers are also discussed. The results presented illustrate the utility of imaging methods in the study of electromagnetic scattering problems and in image understanding in general.

I. INTRODUCTION

The use of polarization diversity over an extremely broad spectrum in coherent scattering measurements as a means of acquiring more information about the scattering object has been the subject of extensive study at the Electro-Optics and Microwave-Optics Laboratory at the University of Pennsylvania [1-4]. An excellent review of the role of polarization in conveying useful information about the scatterer's characteristics is found in [5], and a discussion of the polarization effects and symmetry is given in [6]. In this paper the results of a detailed examination of polarization effects associated with the far field scattered from two conducting cylinders is presented. The influence of polarization on microwave images of the cylinders and on the occurrence of image artefact is determined analytically and verified experimentally.

A theoretical vector development of the far field scattered by perfectly conducting cylinders in a bistatic measuring system is derived in Section II. The approach is first to derive an expression for the field scattered from a single cylinder illuminated by a right-hand circularly polarized (RHCP) plane wave. This expression is then extended in Section III to the case of the directly scattered (or first order) field of two cylinders. The mutually scattered (or second order) field from two cylinders is then formulated in terms of a coherent summation of the scattered field from each cylinder due to the incident wave scattered from the other cylinder. Theoretically, one should proceed in this fashion to calculate the n -th order scattered field. However those higher order scattering terms are found to become negligibly small when the spacing between the two

cylinders is large compared to their radius and to the illuminating wavelength. Therefore in order to simplify computational tasks, only the second order scattered field is analytically derived in this paper. This is called the mutually scattered field. The total wavefield scattered by two cylinders becomes the coherent superposition of the directly scattered component and the mutually scattered component for each polarization. In Section IV, the use of an automated microwave imaging facility employing frequency, polarization and angular diversity to verify the results of theoretical analysis is described. The analytical and experimental results are shown to be in good agreement. The results show that depolarization effects in the mutually scattered field component are more pronounced than in the directly scattered component. Depolarization is taken to be the term describing the change of the polarization of an electromagnetic wave from one state to another brought about by the scattering process.

The notation used in describing the state of polarization in this paper is given next. Referring to Fig. 1, consider a plane containing the z-axis perpendicular to the plane of the paper and the incident wave vector \hat{k}_i . The quantities E_z^i and E_ϕ^i are orthogonal components of a linearly polarized incident plane wave lying respectively parallel and perpendicular to this plane. When right-hand and left-hand circularly polarized fields E_R^i (RHCP) and E_L^i (LHCP) are used they can be related to E_z^i and E_ϕ^i by [7],

$$\begin{bmatrix} E_R^i \\ E_L^i \end{bmatrix} = \frac{1}{\sqrt{2}} \begin{bmatrix} 1 & -j \\ 1 & j \end{bmatrix} \begin{bmatrix} E_z^i \\ E_\phi^i \end{bmatrix} \quad (1)$$

Similarly, we can express the right-hand E_R^s and left-hand E_L^s circularly

polarized components of the scattered field in terms of the scattered fields E_z^s and E_ϕ^s as

$$\begin{bmatrix} E_R^s \\ E_L^s \end{bmatrix} = \frac{1}{\sqrt{2}} \begin{bmatrix} 1 & -j \\ 1 & j \end{bmatrix} \begin{bmatrix} 1 & 0 \\ 0 & -1 \end{bmatrix} \begin{bmatrix} E_\phi^s \\ E_z^s \end{bmatrix} \quad (2)$$

$$= \frac{1}{\sqrt{2}} \begin{bmatrix} 1 & j \\ 1 & -j \end{bmatrix} \begin{bmatrix} E_\phi^s \\ E_z^s \end{bmatrix}$$

where the additional matrix $\begin{bmatrix} 1 & 0 \\ 0 & -1 \end{bmatrix}$ accounts for the coordinate system changing "polarization handedness" upon reflection from the scatterer. Furthermore, because of the change in "handedness", E_L^s and E_R^s will be called the co-polarized and cross-polarized (or depolarized) components of the scattered wavefield when the incident wave is RHCP namely E_R^i .

II. POLARIZATION EFFECTS IN SCATTERING FROM A SINGLE INFINITELY LONG CYLINDER

A. Formulation

Consider an infinitely long cylinder of radius a illuminated by a RHCP plane wave E_R^i as depicted in Fig. 1. The cylinder axis is in the z -direction. From eq. (1) the incident electric field can be expressed as

$$E_R^i = \frac{1}{\sqrt{2}} (E_\phi^i - jE_z^i) \quad (3)$$

where from [7,8],

$$E_z^i = E_0 e^{-jkR \cos(\phi_r - \phi_i)} \quad (4)$$

and

$$E_\phi^i = \frac{1}{j\omega\epsilon_0} (\nabla \times H_z^i \hat{z})_\phi \quad (5)$$

with

$$H_z^i = H_0 e^{-jkR \cos(\phi_r - \phi_i)} \quad (6)$$

are the parallel and perpendicular polarized components of the incident wave, $E_0 = \eta_0 H_0$, η_0 being the intrinsic impedance of free space, ϕ_i and ϕ_r are the angles between the x-axis and the directions of incidence and observation, and $\phi_r = \pi - \phi_i$ in a bistatic measurement system

Equations (4) and (5) can be expressed in a Fourier-Bessel series as [7, 8],

$$E_z^i = E_0 \sum_{n=-\infty}^{\infty} (-j)^n J_n(kR) e^{jn(\phi_r - \phi_i)} \quad (7)$$

$$H_z^i = H_0 \sum_{n=-\infty}^{\infty} (-j)^n J_n(kR) e^{jn(\phi_r - \phi_i)} \quad (8)$$

where $J_n(x)$ is the Bessel function of the first kind of order n , and E_0 and H_0 are the electric and magnetic field amplitudes of the incident plane wave.

The scattered wavefield components E_z^s and E_ϕ^s determined from the boundary conditions,

$$(-j E_z^i + E_z^s) \Big|_{R=a} = 0 \quad (9)$$

and

$$(E_{\phi}^i + E_{\phi}^s) \Big|_{R=a} = \frac{1}{j\omega\epsilon_0} [\nabla \times (H_z^i + H_z^s) \hat{z}]_{\phi} \Big|_{R=a} = 0 \quad (10)$$

where R designates radial distance (see Fig. 1), are given by,

$$E_z^s = jE_0 \sum_n (-j)^n \frac{J_n(ka)}{H_n^{(2)}(ka)} H_n^{(2)}(kR) e^{jn(\phi_r - \phi_i)} \quad (11)$$

and

$$E_{\phi}^s = -jE_0 \sum_n (-j)^n \frac{J'_n(ka)}{H_n^{(2)'}(ka)} H_n^{(2)}(kR) e^{jn(\phi_r - \phi_i)} \quad (12)$$

where the summations over n here and in subsequent equations is understood to range from $-\infty$ to ∞ , $H_n^{(2)}(x)$ is the Hankel function of the second kind, and $H_n^{(2)'}(x)$ is its derivative with respect to the argument x .

If $kR \gg 1$, i.e., under the far field approximation, the bistatic scattered field ($\phi_i \neq 0$, and $\phi_r = \pi - \phi_i$) becomes

$$E_z^s = j \sqrt{\frac{2j}{\pi kR}} e^{-jkR} E_0 \sum_n \frac{J_n(ka)}{H_n^{(2)}(ka)} e^{jn(\pi - 2\phi_i)} \quad (13)$$

$$E_{\phi}^s = - \sqrt{\frac{2j}{\pi kR}} e^{-jkR} E_0 \sum_n \frac{J'_n(ka)}{H_n^{(2)'}(ka)} e^{jn(\pi - 2\phi_i)} \quad (14)$$

Using the transform relationship given in eq. (2), the scattered fields expressed in terms of circular polarization are

$$E_R^S = \frac{1}{\sqrt{2}} (E_\phi^S + jE_z^S)$$

$$= \sqrt{\frac{j}{\pi k R}} e^{-jkR} E_0 \sum_n \left(-\frac{J_n'(ka)}{H_n^{(2)'}(ka)} - \frac{J_n(ka)}{H_n^{(2)}(ka)} \right) e^{jn(\pi-2\phi_i)} \quad (15)$$

and

$$E_L^S = \frac{1}{\sqrt{2}} (E_\phi^S - jE_z^S)$$

$$= \sqrt{\frac{j}{\pi k R}} e^{-jkR} E_0 \sum_n \left(-\frac{J_n'(ka)}{H_n^{(2)'}(ka)} + \frac{J_n(ka)}{H_n^{(2)}(ka)} \right) e^{jn(\pi-2\phi_i)} \quad (16)$$

Equations (15) and (16) indicate that the far field scattered from a cylinder illuminated by a RHCP plane wave is elliptically polarized in the bistatic case and also in the monostatic scattering case ($\phi_i=0$ and $\phi_r=\pi$) because E_z^S and E_ϕ^S in eqs. (13) and (14) differ in magnitude and are not in phase. The observed scattered far field, measured for example by a coherent receiver, can be separated into two parts: one containing the range term $\exp(-jkR)/\sqrt{R}$ appearing outside the summation terms which accounts for the propagation time delay or phase shift from the coordinate origin to the receiver; and the summation terms which can be viewed as the equivalent to the "Bojarski identity" [9,10] which strictly speaking conveys information about the object in the high frequency limit ($ka \gg 1$).

It was shown by Bojarski and Lewis assuming physical optics and Born approximations hold and neglecting polarization effects, that a Fourier transform relationship exists between the shape of a perfectly conducting object and its range-corrected backscattered far field frequency response. In the next section, numerical examples are given to examine and elucidate

the Fourier inversion reconstruction for each of the circularly polarized fields given in eqs. (15) and (16) in the microwave regime. Note that in arriving at the results in eqs. (15) and (16) the physical optics approximation was not involved and hence they hold for any value of the wavenumber k .

B. Numerical Results

The range-corrected scattered far field component E_L^S and E_R^S were calculated from the summation terms in eqs. (15) and (16) using 33 terms for n ranging from -16 to 16 for the frequency range (6-17) GHz for a cylinder of radius 3.8 cm and a bistatic angle of $\phi_i = 6^\circ$. The results are shown in Fig. 2(a) and (b). The spectral range (6-17) GHz is chosen to coincide with the measurement capabilities of the system utilized in the experimental portion of the study. The depolarized component E_R^S of the scattered field is shown to be about 25dB lower than the co-polarized component E_L^S and is seen to decrease as the frequency approaches the optical regime [11].

One-dimensional Fourier inversion of the range-corrected E_L^S component with respect to k gives the range profile of the illuminated cylinder shown in Fig. 2(c). The peak in the profile corresponds to specular reflection from the front surface of the cylinder. The range profile reconstructed from the range-corrected depolarized component E_R^S shown in the same figure is seen, however, to contain two peaks. The first peak is caused also by specular reflection from the front surface of the cylinder, while the second peak which is about 20dB weaker is due to the effect of creeping wave associated with the surface wave propagating around the cylinder [7]. The contribution from the creeping wave is known also to decrease as the cylinder radius increases.

Since the range resolution is inversely proportional to the spectral range of the illuminating signal, the ability to pinpoint the reflection location on the scattering cylinder is greatly enhanced by gathering data over a broad frequency range. A long cylinder can therefore be used as a calibration object for characterizing broadband microwave scattering system used in frequency and polarization diversity measurement [4]. In Section IV, the scattered field E_R^S and E_L^S from two cylinders will be measured in an anechoic chamber using a single cylinder as the calibration object for system characterization.

III. POLARIZATION EFFECTS IN SCATTERING FROM TWO INFINITELY LONG CYLINDERS

A. Formulation of Direct Scattering

The directly scattered wavefield from two conducting infinitely long parallel cylinders illuminated by a RHCP plane wave as shown in Fig. 3 can be obtained by superposition using eqs. (11) and (12). This leads to a summing of eqs. (11) and (12) with each multiplied by a phase term due to the offset distance b from the coordinate origin to each cylinder. The resultant field expressions referring to the quantities shown in Fig. 3

$$\begin{aligned}
 l_{E_z}^S &= l_{E_z^+}^S + l_{E_z^-}^S \\
 &= j E_0 \sum_n (-j)^n \left\{ \frac{J_n(ka)}{H_n^{(2)}(ka)} [H_n^{(2)}(kR_+) e^{jn(\phi_+ - \phi_1)} e^{-jkb \cos(\theta_+ - \phi_1)} \right. \\
 &\quad \left. + H_n^{(2)}(kR_-) e^{jn(\phi_- - \phi_1)} e^{jkb \cos(\theta_- - \phi_1)}] \right\} \quad (17)
 \end{aligned}$$

and

$$\begin{aligned}
l_{E\phi}^s &= l_{E\phi}^s + l_{E\phi}^s \\
&= -j E_0 \sum_n \{ (-j)^n \frac{J_n'(ka)}{H_n^{(2)}(ka)} [H_n^{(2)}(kR_+) e^{jn(\phi_+ - \phi_i)} e^{-jkb \cos(\theta_{\rightarrow} - \phi_i)} \\
&\quad + H_n^{(2)}(kR_-) e^{jn(\phi_- - \phi_i)} e^{jkb \cos(\theta_{\rightarrow} - \phi_i)}] \} \quad (18)
\end{aligned}$$

where the superscript 1 is used here to designate the direct scattering, as the superscript 2 will be used later to designate the doubly scattered field or mutual scattering case. The subscripts + and - are used to distinguish the two cylinders and θ_{\rightarrow} is the angle between the line connecting the centers of the two cylinders and the x-axis.

In the far field approximation, $kR \gg 1$, we can use the following approximations

$$\begin{aligned}
R_+ &\sim R + b \cos(\theta_{\rightarrow} + \phi_i) \\
R_- &\sim R - b \cos(\theta_{\rightarrow} + \phi_i) \quad (19)
\end{aligned}$$

and

$$\phi_- \sim \phi_+ \sim \pi - \phi_i \quad (20)$$

Therefore, after normalizing the range term $\exp(-jkR)/\sqrt{R}$, eqs. (17) and (18) become

$$l_{Ez}^s = j \sqrt{\frac{2j}{\pi k}} 2E_0 \cos(2kb \cos\theta_{\rightarrow} \cos\phi_i) \sum_n \frac{J_n(ka)}{H_n^{(2)}(ka)} e^{jn(\pi - 2\phi_i)} \quad (21)$$

$$l_{E_{\phi}}^s = - \sqrt{\frac{2j}{\pi k}} 2E_0 \cos(2kb \cos\theta_{\rightarrow} \cos\phi_i) \sum_n \frac{J'_n(ka)}{H'_n(2)(ka)} e^{jn(\pi-2\phi_i)} \quad (22)$$

or

$$l_{E_R}^s = 2 \cos(2kb \cos\theta_{\rightarrow} \cos\phi_i) E_R^s \quad (23)$$

$$l_{E_L}^s = 2 \cos(2kb \cos\theta_{\rightarrow} \cos\phi_i) E_L^s \quad (24)$$

where E_R^s and E_L^s are the expressions for the scattered fields from one cylinder as given by eqs. (15) and (16) excluding the range terms. Eqs. (23) and (24) are equal to eqs. (15) and (16) (excluding the range term) multiplied by a sum of two linear phase terms contributed from the projected distances $\pm b \cos\theta_{\rightarrow} \cos\phi_i$ from each cylinder to the coordinate origin.

B. Numerical Results

Figure 4 shows the range profiles derived from the LHCP and the RHCP components of the directly scattered field for the case of $\theta_{\rightarrow} = 0^\circ$ and $a=3.8\text{cm}$, $b=13.7\text{cm}$. These are near replicas of single cylinder profiles displaced by distance $\pm b \cos\phi_i$.

By measuring the backscattered field components for different closely spaced values of θ_{\rightarrow} , correcting them for the range factor $\exp(-jkR)/\sqrt{R}$, and presenting them in polar format in which the polar angle is θ_{\rightarrow} and radial distance represents frequency, we can obtain a slice in the Fourier space of the object [3,4]. Fourier inversion of the slice data after interpolation onto a rectangular format using a four nearest neighbor interpolation algorithm [12] yields in accordance to the projection-slice

theorem [13] a projection image representing the projection of the scattering centers of the object on a plane parallel to the plane of the Fourier space slice.

Figure 5(a) and (b) shows Fourier plane slices obtained from the ${}^1E_L^s$ and ${}^1E_R^s$ components presented in a polar format consisting of 256 radial lines equally spaced over 360° , with each line containing 64 equally spaced frequency points covering (6-17) GHz range. Considering that the radial (frequency) and angular (aspect) sampling criterion needed to avoid aliasing are respectively $\delta f \leq c/4b$ and $\delta \theta \leq \lambda_{\min}/2b$ [4], the acquired data in the above polar format is somewhat oversampled. The reconstructed images for each circularly polarized component as obtained via a two-dimensional Fourier transformation, are given in Fig. 6. Several observations can be made based on the images shown. First, the ${}^1E_L^s$ component gives two distinct circles representing the external cross-sectional outline images of the two cylinders. The radii and spacings of the cylinders in the two images correspond quite closely to the values a and b of the object. This result agrees with the physical optics diffraction theory given by Bojarski and Lewis in the context of their inverse scattering theory [9,10]. However the ${}^1E_R^s$ component, ignored in the scalarized physical optics approximation, also gives two faint circles which are contributed from the weak depolarization and creeping wave effects. In the next section, we will analyze the mutual scattering between two cylinders in each polarization state.

C. Formulation of Mutual Scattering

First we consider the case when the "-" cylinder is illuminated by the directly scattered wave from "+" cylinder to obtain the contribution

of the "-" cylinder to the second order mutually scattered wavefield. The contribution of the "+" cylinder to the mutually scattered wave by re-scattering the directly scattered wave from "-" cylinder can be obtained by interchanging the "+" and "-" subscripts in the resulting expressions.

The scattered wave from the "+" cylinder incident on the "-" cylinder is rewritten from the first terms in eqs. (17), (18) and (5) as

$$\begin{matrix} 2 \\ - \\ E_z \end{matrix}^i = \begin{matrix} 1 \\ + \\ E_z \end{matrix}^s = \sum_n \begin{matrix} 1 \\ + \\ A_n \end{matrix} H_n^{(2)}(kR_+) e^{jn\phi_+} \quad (25)$$

$$\begin{matrix} 2 \\ - \\ H_z \end{matrix}^i = \begin{matrix} 1 \\ + \\ H_z \end{matrix}^s = \sum_n \begin{matrix} 1 \\ + \\ B_n \end{matrix} H_n^{(2)}(kR_+) e^{jn\phi_+} \quad (26)$$

where

$$\begin{matrix} 1 \\ + \\ A_n \end{matrix} = jE_0 (-j)^n \frac{J_n(ka)}{H_n^{(2)}(ka)} e^{-jkb \cos(\theta \rightarrow -\phi_1)} e^{-jn\phi_i} \quad (27)$$

$$\begin{matrix} 1 \\ + \\ B_n \end{matrix} = -H_0 (-j)^n \frac{J'_n(ka)}{H_n^{(2)}(ka)} e^{-jkb \cos(\theta \rightarrow -\phi_i)} e^{-jn\phi_i} \quad (28)$$

where R_+ in accordance to Fig. 3 is now the distance between the center of the "+" cylinder and an observation point on the surface of the second cylinder. The second order mutually scattered wavefield from the "-" cylinder can then be expressed in terms of the cylindrical wave function [7,8] as

$$\begin{matrix} 2 \\ - \\ E_z \end{matrix}^s = \sum_n \begin{matrix} 2 \\ - \\ A_n \end{matrix} H_n^{(2)}(kR_-) e^{jn\phi_-} \quad (29)$$

and

$$\begin{matrix} 2 \\ - \\ H_z \end{matrix}^s = \sum_n \begin{matrix} 2 \\ - \\ B_n \end{matrix} H_n^{(2)}(kR_-) e^{jn\phi_-} \quad (30)$$

where the scattering coefficients ${}^2_{-}A_n$ and ${}^2_{-}B_n$ are determined from the boundary conditions

$$\left. \begin{aligned} & {}^2_{-}E_z^i + {}^2_{-}E_z^s \Big|_{R_-=a} \\ &= \sum_m \frac{1}{+} A_m H_m^{(2)}(kR_+) e^{jm\phi_+} + \sum_n \frac{2}{-} A_n H_n^{(2)}(kR_-) e^{jn\phi_-} \Big|_{R_-=a} = 0 \end{aligned} \right. \quad (31)$$

and

$$\left. \begin{aligned} & {}^2_{-}E_\phi^i + {}^2_{-}E_\phi^s \Big|_{R_-=a} \\ &= \frac{1}{j\omega\epsilon_0} [\nabla \times \left(\sum_m \frac{1}{+} B_m H_m^{(2)}(kR_+) e^{jm\phi_+} \right. \\ & \left. + \sum_n \frac{2}{-} B_n H_n^{(2)}(kR_-) e^{jn\phi_-} \right) \hat{z}]_\phi \Big|_{R_-=a} = 0 \end{aligned} \right. \quad (32)$$

and in using eqs. (25) and (26) to write eqs. (31) and (32) we have changed the summation variable from n to m .

In order to impose the boundary conditions at $R_-=a$, the term $H_m^{(2)}(kR_+)$ must be expressed in terms of the cylindrical wave referred to the coordinate of the "-" cylinder. Using the additional theorem [14], which is valid for $2b>a$, we can obtain

$$H_m^{(2)}(kR_+) e^{jm\phi_+} = \sum_n H_{n-m}^{(2)}(2kb) J_n(kR_-) e^{jn\phi_-} e^{-j(n-m)\theta_{-+}} \quad (33)$$

Substituting eq. (33) into eqs. (31) and (32) and equating the coefficients of $\exp(-jn\phi_-)$ to zero, the mutual scattering coefficients,

$$2_{-A_n} = - \frac{J_n(ka)}{H_n^{(2)}(ka)} \sum_m 1_{+A_m} H_{n-m}^{(2)}(2kb) e^{-j(n-m)\theta_{-+}} \quad (34)$$

and

$$2_{-B_n} = - \frac{J'_n(ka)}{H_n^{*(2)}(ka)} \sum_m 1_{+B_m} H_{n-m}^{(2)}(2kb) e^{-j(n-m)\theta_{-+}} \quad (35)$$

are found where 1_{+A_m} and 1_{+B_m} are given in eqs. (27) and (28). Note eq. (34) which is the scattering coefficient of the $2_{-E_z^s}$ component is the same as that derived by Twersky [15] for the second order scalar scattering coefficient of two cylinders. The other scattering coefficient 2_{-B_n} in eq. (35) belongs to the $2_{-E_\phi^s}$ component of the mutually scattered field from "-" cylinder and reflects for the vector formulation developed here.

Therefore

$$2_{-E_z^s} = -jE_0 e^{-jkb \cos(\theta_{-+} - \phi_i)} \sum_n \frac{J_n(ka)}{H_n^{(2)}(ka)} H_n^{(2)}(kR_-) e^{jn\phi_-} \\ \sum_m (-j)^m \frac{J_m(ka)}{H_m^{(2)}(ka)} e^{-jm\phi_i} H_{n-m}^{(2)}(2kb) e^{-j(n-m)\theta_{-+}} \quad (36)$$

and

$$2_{-H_z^s} = H_0 e^{-jkb \cos(\theta_{-+} - \phi_i)} \sum_n \frac{J'_n(ka)}{H_n^{*(2)}(ka)} H_n^{(2)}(kR_-) e^{jn\phi_-} \\ \sum_m (-j)^m \frac{J'_m(ka)}{H_m^{*(2)}(ka)} e^{-jm\phi_i} H_{n-m}^{(2)}(2kb) e^{-j(n-m)\theta_{-+}} \quad (37)$$

As $kr \gg 1$, the range-corrected scattered far field from the "-" cylinder due to the incoming wave from the "+" cylinder for each linear polarization will be,

$$\begin{aligned} \frac{2E_z^s}{-E_z} = & -j \sqrt{\frac{2j}{\pi k}} e^{-j2kbsin\phi_i} \sin\theta \rightarrow E_0 \sum_n \sum_m (-j)^{n+m} \frac{J_n(ka) J_m(ka)}{H_n^{(2)}(ka) H_m^{(2)}(ka)} \\ & e^{-j(n+m)\phi_i} H_{n-m}^{(2)}(2kb) e^{-j(n-m)\theta} \rightarrow \end{aligned} \quad (38)$$

and

$$\begin{aligned} \frac{2E_\phi^s}{-E_\phi} = & \frac{1}{j\omega\epsilon_0} (\nabla \times \frac{2E_z^s}{-E_z} \hat{z})_\phi \\ = & \sqrt{\frac{2j}{\pi k}} e^{-j2kbsin\phi_i} \sin\theta \rightarrow E_0 \sum_n \sum_m (-j)^{n+m} \frac{J'_n(ka) J'_m(ka)}{H'_n(2) (ka) H'_m(2) (ka)} \\ & e^{-j(n+m)\phi_i} H_{n-m}^{(2)}(2kb) e^{-j(n-m)\theta} \rightarrow \end{aligned} \quad (39)$$

By interchanging the subscripts "+" and "-" in eqs. (38) and (39), we can obtain the mutually scattered far fields $\frac{2E_z^s}{+E_z}$ and $\frac{2E_\phi^s}{+E_\phi}$ from "+" cylinder due to the incoming wave or directly scattered from the "-" cylinder. The mutually scattered field from two cylinders for each linear polarization is the summation of these two terms i.e.,

$$^2E_z^s = ^2E_z^s + ^2E_z^s$$

$$= -j \sqrt{\frac{2j}{\pi k}} E_0 \sum_n \sum_m (-j)^{n+m} \frac{J_n(ka) J_m(ka)}{H_n^{(2)}(ka) H_m^{(2)}(ka)} e^{-j(n+m)\phi_i - j(n-m)\theta_{\rightarrow}}$$

$$H_{n-m}^{(2)}(2kb) \begin{cases} 2 \cos(2kb \sin\phi_i \sin\theta_{\rightarrow}) & \text{---- } n+m \text{ even} \\ -j2 \sin(2kb \sin\phi_i \sin\theta_{\rightarrow}) & \text{---- } n+m \text{ odd} \end{cases} \quad (40)$$

and

$$^2E_\phi^s = ^2E_\phi^s + ^2E_\phi^s$$

$$= \sqrt{\frac{2j}{\pi k}} E_0 \sum_n \sum_m (-j)^{n+m} \frac{J'_n(ka) J'_m(ka)}{H_n^{(2)}(ka) H_m^{(2)}(ka)} e^{-j(n+m)\phi_i - j(n-m)\theta_{\rightarrow}}$$

$$H_{n-m}^{(2)}(2kb) \begin{cases} 2 \cos(2kb \sin\phi_i \sin\theta_{\rightarrow}) & \text{---- } n+m \text{ even} \\ -j2 \sin(2kb \sin\phi_i \sin\theta_{\rightarrow}) & \text{---- } n+m \text{ odd} \end{cases} \quad (41)$$

From which the circular polarization expression,

$$^2E_R^s = (^2E_\phi^s + j^2E_z^s)/\sqrt{2} \quad (42)$$

and

$$^2E_L^s = (^2E_\phi^s - j^2E_z^s)/\sqrt{2} \quad (43)$$

can be obtained. Also here, because of the unequal magnitude and phase angle of the RHCP and LHCP scattered components in the above equations, the mutually scattered far field $^2E^s$ from two conducting cylinders illuminated with RHCP plane wave is elliptically polarized.

It is interesting to note that eqs. (38) and (39) have leading phase terms $\exp(j2kbsin\phi_i \sin\theta_{\pm})$. This implies that contributions to the image reconstructed from ${}^2_{-}E^s$ (or ${}^2_{+}E^s$) will have an additional displacement $bsin\phi_i$ (or $-bsin\phi_i$) in the y-direction. The resulting image detail can be useful therefore in some applications for determining the bistatic scattering angle, if it is not known, from the received scattered far field of a two-cylinder object.

It can be seen that the second order scattering coefficients consist of sums of products of two scattering coefficients of the single cylinder and terms depending on the distance between the two cylinders. This mutually scattered far field expression can be then physically interpreted as arising from two scattering processes as the incident plane wave is doubly scattered by one cylinder onto the other and back. The second order scattering coefficient will approach zero for large separation between the two cylinders due to the behavior of the Hankel function $H_{n-m}^{(2)}(2kb)$. This implies the higher order scattering coefficients could be neglected when the cylinder spacing is large compared to the illuminating wavelength.

In the next section we will examine the mutual scattering of two cylinders for each polarization using numerical simulation.

D. Numerical Results

Shown in Fig. 7 is the mutually scattered field components ${}^2_{E_L^s}$ and ${}^2_{E_R^s}$ calculated from eqs. (42) and (43) for aspect angle $\theta_{\pm} = 90^\circ$ with n and m in the summations ranging from -16 to 16. The magnitude of the depolarized component ${}^2_{E_R^s}$ is seen to be up to about 15dB greater than that of ${}^2_{E_L^s}$ due to the effect of the mutual scattering between the two cylinders. The corresponding range profiles reconstructed from each polarization component are

given in Fig. 7(c). Each of these shows two primary peaks whose separation is related to the bistatic angle ϕ_i . In addition the profile derived from the ${}^2E_L^s$ component shows additional weaker peaks and also the higher order terms ignored in our analysis. The value of $\phi_i = 6^\circ$ is used and those of a and b are as before.

The numerically generated Fourier space slices obtained by computing ${}^2E_R^s$ and ${}^2E_L^s$ as a function of frequency and rotation angle θ_{\rightarrow} are shown in Fig. 8. The same polar format used earlier i.e., 64 equally spaced frequency points covering the range (6-17) GHz per radial line and 256 radial lines covering an angular range of 360° , is utilized. The images obtained by Fourier inversion of these slices are shown in Fig. 9. The reconstructed images exhibit the effect of mutual scattering between two cylinders. The effect consists of two symmetrical "smile patterns" with width $2(b-a)$. The two peaks presented in Fig. 7 correspond to a cross-sectional view of the "smile pattern" at $\theta_{\rightarrow} = 90^\circ$. The lip separation, given by $b\sin\phi_i$, is determined by the bistatic angle. It becomes wider as the bistatic angle increases as indicated in Fig. 9(c) for which the bistatic angle ϕ_i is 8° as compared to $\phi_i = 6^\circ$ in (a) and (b) of the figure. The smile pattern will merge into a "ring pattern" as shown in Fig. 9(d) when $\phi_i = 0^\circ$ i.e., the case of monostatic scattering. This suggests that the bistatic angle spanned by transmitting and receiving antennas can, if necessary, in certain situations be determined from the lip separation of the cross-polarized image of a two cylinder test target.

The total scattered wavefield from two cylinders is the superposition of directly scattered components given in eqs. (23), (24) and the mutually scattered components given in eqs. (42), (43) for each state of polarization. Fourier space slices, obtained from the computed total RHCP and LHCP

components, and their reconstructed images are shown in Fig. 10. Due to the pronounced depolarization effect contributed from the mutual scattering, the RHCP component dominated by the ${}^2E_R^s$ wavefield, is about up to 15dB greater than ${}^1E_R^s$. Therefore the reconstructed image consists of two distinct image of the smile pattern bridging two adjacent faint circles representing the projection image of the two cylinders. The slight spacing at the corners of the "smile pattern", as compared to the narrower spacing in the experimental results presented in the following section, is attributed to the finite number of terms taken in the calculation of eqs. (40) and (41). The LHCP component gives the same image as Fig. 6(a) of the directly scattered data which is merely the projection of the two cylinders because for this case ${}^2E_L^s$ is more than 20dB weaker than ${}^1E_L^s$ and hence this image is seen to be free of any depolarization effects. Note in the strict sense of imaging, the "smile patterns" in Fig. 9 do not correspond to any physical detail of the two cylinders and hence represent "ghost images" or image artefact.

IV. EXPERIMENTAL RESULTS

Due to continuing advances in microwave instrumentation and technology, it is now possible to develop efficient and highly accurate computer-controlled microwave measurement system capable of collecting full vector information of the scattered wavefield including amplitude, phase, frequency and polarization [1-4]. The experimental arrangement used to acquire wideband polarization-selective scattering data of test objects is shown in Fig. 11. The test object, consisting of two metallic cylinders 27.4 cm apart, each 100 cm long and 3.8 cm in radius, is mounted on a computer controlled positioner situated in an anechoic chamber. The

entire measurement sequence consisting of angular positioning of the test object in azimuth in increments of 1.4° , incremental frequency stepping over a (6-17) GHz spectral range, switching of antenna polarization, digitization and storage of the amplitude and phase of the scattered field measured by the coherent receiver, is carried out under computer control which also performs the required digital signal processing. As mentioned earlier in Section II, a single metallic cylinder is used to characterize the system frequency response including determination of the range information needed to correct for the range term. Further detail on this and on the removal of clutter signals in anechoic chamber measurements are found in [3,4].

Results of two circular polarization measurements, shown in Fig. 12, are obtained with the system using RHCP plane wave illumination produced by a parabolic reflector antenna and an electronically switchable RHCP and LHCP dual-polarization horn receiving antenna. The Fourier slice data and corresponding reconstructed images for each measured polarization are shown. Several observations can be made. First, both the RHCP and LHCP scattered fields and their reconstructed images agree well with the analytical results given in Fig. 10. Secondly, the RHCP component gives a distinctive image of the "smile pattern" and two faint circles. This experimental result shows that the higher order scattering terms, beyond $-16 < n < 16$ used in our computations, are negligibly small when the cylinders spacing is chosen to be greater than the radius of each cylinder and than the illuminating wavelength. Thirdly, the depolarized image of ${}^2E_L^s$ is nearly not visible because it is 40db lower in image intensity (corresponding to 20dB weaker amplitude) than the ${}^1E_L^s$ component.

V. DISCUSSION

In an attempt to clarify the role of polarization diversity in microwave image formation, a systematic analytical and experimental study of the directly and mutually scattered wavefields of two cylinders in an orthogonal polarization basis was undertaken. The results show that the analytical and experimental results obtained and reported here are in good agreement. These results suggest that in the case of dual-cylinder objects illuminated with a RHCP plane wave, the LHCP scattered field primarily determined by specular reflections from the illuminated surfaces of cylinders is free of any noticeable depolarization effects arising from multiple scattering between the two cylinders. Two-dimensional Fourier inversion of the LHCP Fourier slice data gives a projection image showing the shape and location of scattering centers on the two cylinders. Thus RHCP plane wave illumination and LHCP scattered field measurement can be used to suppress multiple scattering effects, and therefore artefacts, in microwave imaging of cylinders and other more complex multiple segment objects. The RHCP measurement, on the other hand, gives the mutual scattering information. The image information in this case is an "artefact" as it does not correspond to any actual physical detail or optical image of the object. The mutual scattering information carries further detail about the scatterers and the scattering geometry. For example as shown here the artefact image detail can be related to the bistatic angle and the cylinder spacing.

The results presented here lead to better understanding of the role of polarization in microwave imaging in conveying more information about multiple simple-body scatterers e.g., cylinders considered here, and more complex objects in general. The methods presented also serve to illustrate

the power of microwave imaging techniques in the analysis and understanding of electromagnetic scattering problems.

VI. ACKNOWLEDGEMENT

The authors wish to thank C.L. Werner and R.E. Marx for their interest and useful discussion. This research was supported by the Air Force Office of Scientific Research, Air Force Systems Command, under grant no. AFOSR-81-0240F, the Army Research Office, under grant DAAG-29-83-K-0120 PO2 and the RCA Corporation.

References

- [1] C. L. Werner, "An Automated Frequency Response and Radar Cross-Section Measurement Facility for Microwave Imaging", Master Thesis, University of Pennsylvania, 1980
- [2] T. H. Chu, "Optimal Methodologies in Inverse Scattering Utilizing Wavelength, Polarization and Angular Diversity", Ph.D Dissertation, University of Pennsylvania, 1983
- [3] N. H. Farhat, C. L. Werner and T. H. Chu, "Prospect. for Three-dimensional Projective and Tomographic Imaging Radar Network", Radio Science, Vol.19, No.5, Sep.-Oct. 1984, pp.1347-1355
- [4] N. H. Farhat and T. H. Chu, "Projection Image of 3-D microwave Scatterers with Near Optical Resolution" in Indirect Imaging, J. A. Robert Ed., Cambridge University Press, 1984, pp.33-40
- [5] W-M. Boerner, "Polarization Utilization in Electromagnetic Inverse Scattering", Ch.7 in Inverse Scattering Problems in Optics, H. P. Baltes, Ed., Vol.20, New York:Springer Verlag, 1980
- [6] G. E. Heath, "Bistatic Scattering Reflection Asymmetry, Polarization Reversal Asymmetry, and Polarization Reversal Reflection Symmetry", IEEE trans. on Antennas and Propagation, Vol.AP-29, No.3, May 1981, pp.429-434
- [7] G. T. Ruck, D. E. Barrick, W. D. Stuart and C. K. Krichbaum, Radar Cross Section Handbook, Ch.4, Vol.1, New York:Plenum 1970
- [8] R. F. Harrington, Time-Harmonic Electromagnetic Fields, Ch.5, New York: McGraw-Hill 1961
- [9] N. N. Bajarski, "Three-Dimensional Electromagnetic Short Pulse Inverse Scattering", Syracuse University Res. Corp., Syracuse, N.Y., Feb. 1967
- [10] R. M. Lewis, "Physical Optics Inverse Diffraction", IEEE trans. on Antennas and Propagation, Vol.AP-17, No.3, May 1969 pp.308-314
- [11] T. M. Smith and S. L. Borison, "Depolarization of a Circularly Polarized Wave by an Infinite Cylinder", IEEE trans. on Antennas and Propagation, Vol.AP-22, No.6, Nov. 1974, pp.796-798
- [12] R. M. Mersereau and A. V. Oppenheim, "Digital Reconstruction of Multidimensional Signals from Their Projections", Proc. of the IEEE, Vol.62, No.10, 1974, pp.1319-1338
- [13] G. T. Herman Ed., Image Reconstruction from Projections Implementation and Applications, Topics in Applied Physic, Vol.32, New York:

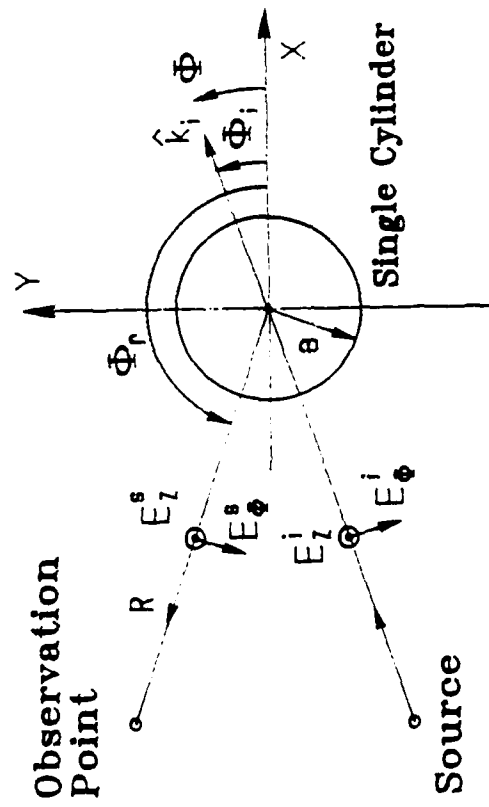
Springer-Verlag, 1979

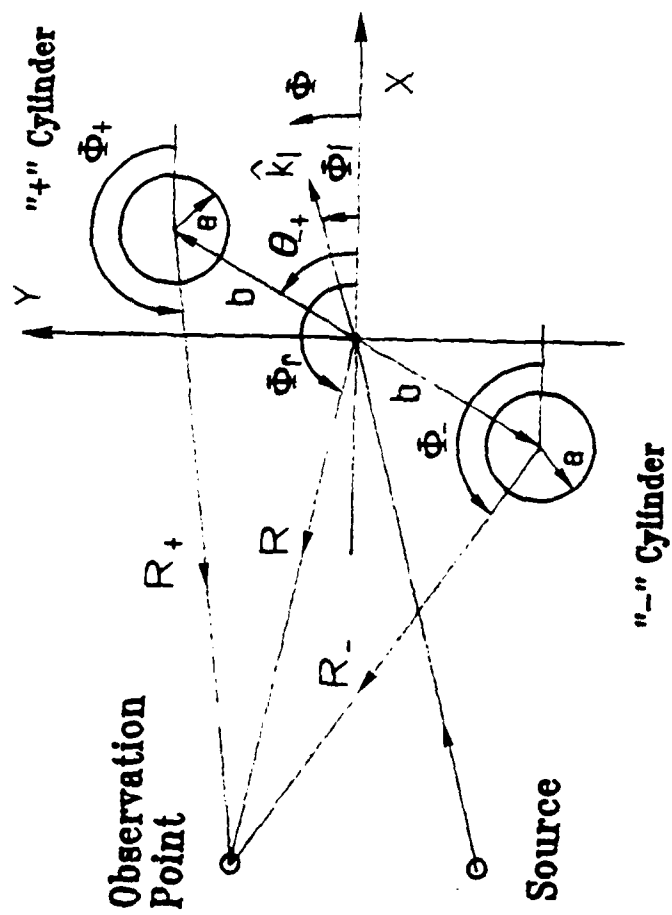
[14] G. N. Watson, A Treatise on the Theory of Bessel Functions, Cambridge University Press. Ch.11, London, 1958

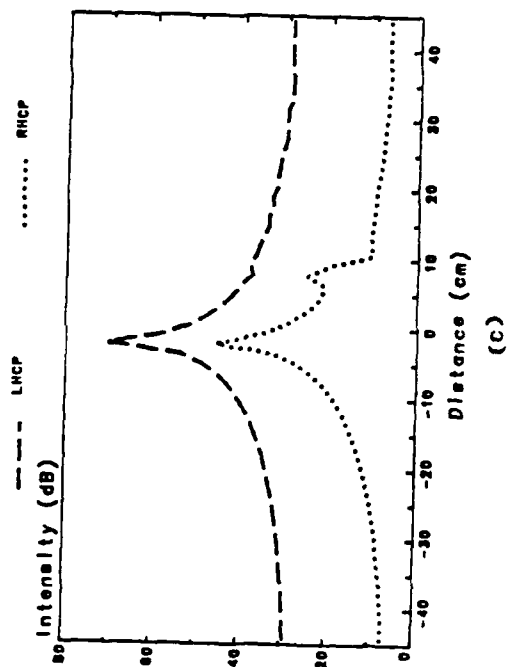
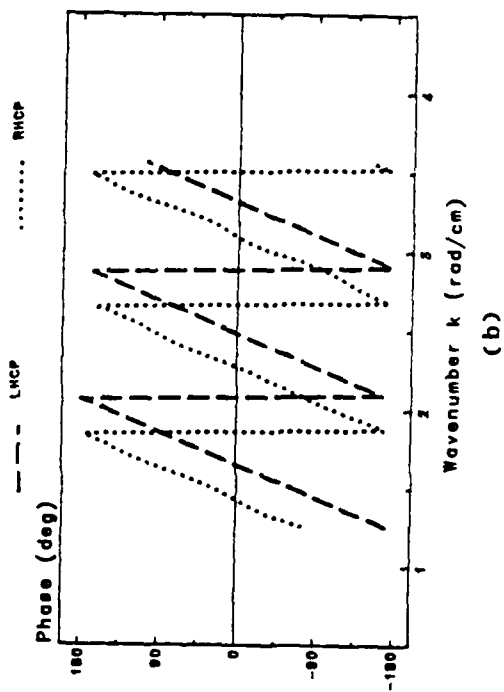
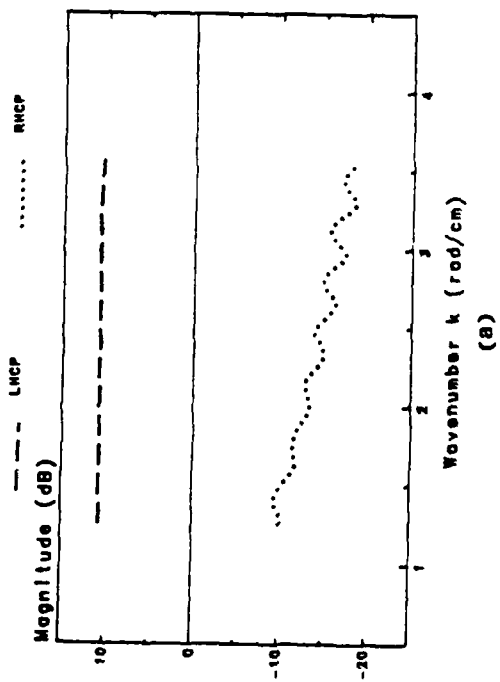
[15] V. Twersky, "Multiple Scattering of Radiation by an Arbitrary Configuration of Parallel Cylinders", The Journal of the Acoustical Society of America, Vol.24, No.1, Jan. 1952, pp.42-46

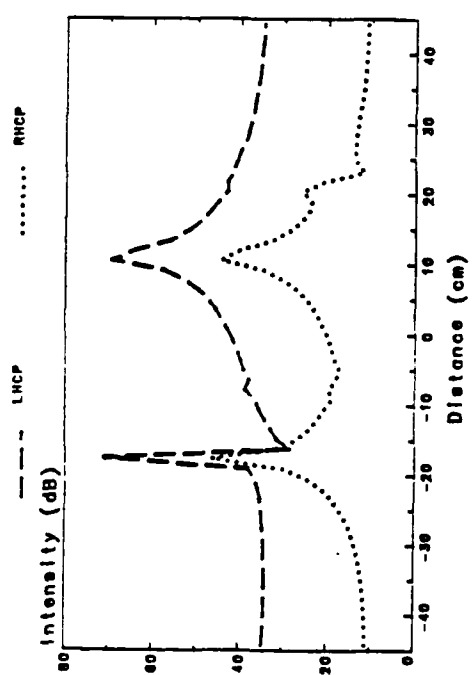
LIST OF FIGURES

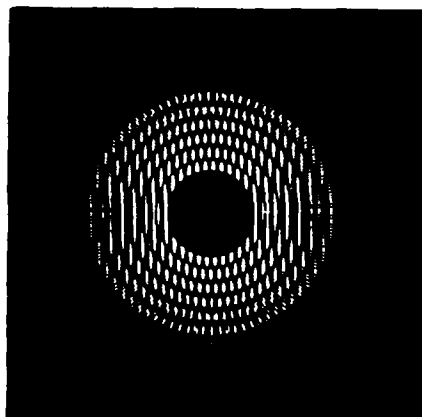
- Fig. 1. Scattering geometry of a single infinitely long cylinder.
- Fig. 2. Magnitudes (a) and phases (b) of the LHCP and RHCP components of the directly scattered field from a single cylinder of radius $a=3.8$ cm illuminated by a RHCP plane wave obtained for a range $4.79 < ka < 13.57$ and (c) reconstructed range profiles.
- Fig. 3. Scattering geometry of two parallel infinitely long cylinders.
- Fig. 4. Reconstructed range profiles of the LHCP and RHCP directly scattered fields of two cylinders.
- Fig. 5. Polar plots of (a) LHCP and (b) RHCP directly scattered fields of two cylinders.
- Fig. 6. Results of reconstructed images of two cylinders from (a) LHCP and (b) RHCP directly scattered fields data.
- Fig. 7. Magnitude (a) and phase (b) of the RHCP and LHCP mutually scattered fields of two cylinders, and (c) reconstructed range profiles for $\phi_i = 6^\circ$.
- Fig. 8. Polar plots of (a) RHCP and (b) LHCP mutually scattered fields of two cylinders.
- Fig. 9. Reconstructed images of two cylinders from numerically generated (a) RHCP and (b) LHCP mutually scattered field data for $\phi_i = 6^\circ$, and from RHCP data for (c) $\phi_i = 8^\circ$ and (d) $\phi_i = 0^\circ$.
- Fig. 10. Polar representations of (a) RHCP and (b) LHCP scattering data of two cylinders and associated images obtained by Fourier inversion.
- Fig. 11. Measurement system situated in an anechoic chamber environment.
- Fig. 12. Experimentally obtained polar representations of (a) RHCP and (b) LHCP scattering data and associated images obtained by Fourier inversion.



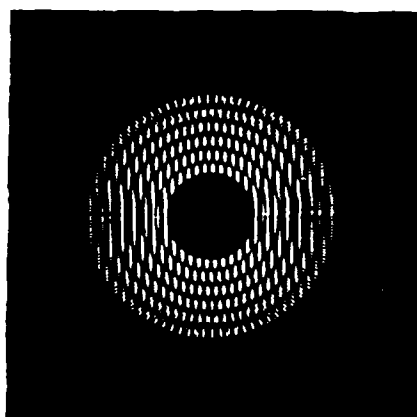






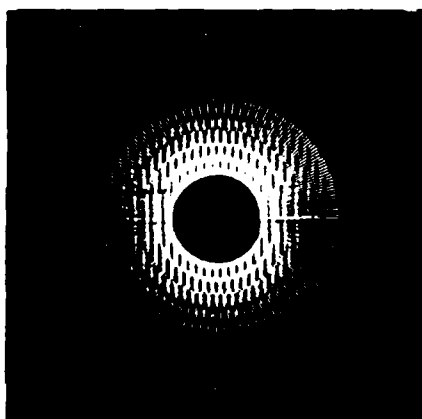


Real part

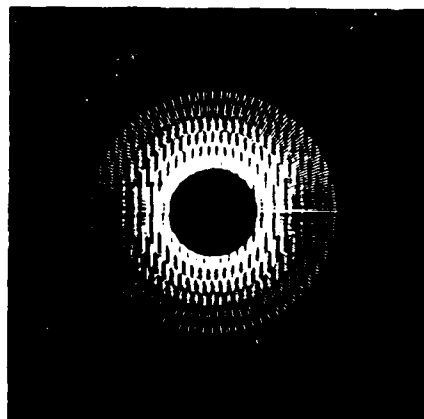


Imaginary part

(a)

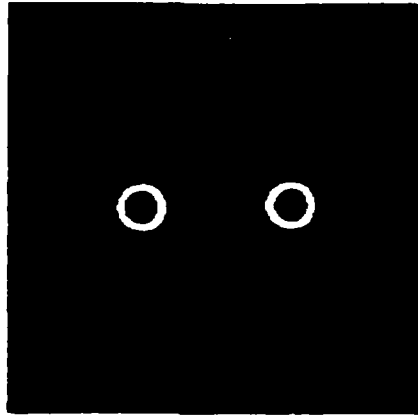


Real part

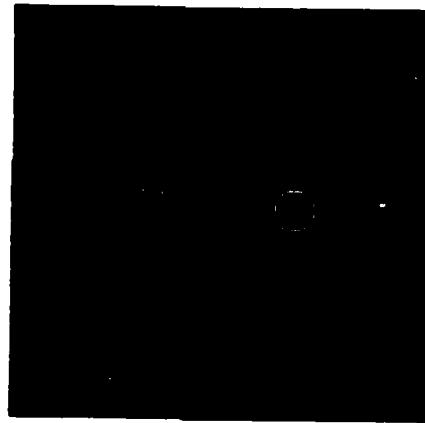


Imaginary part

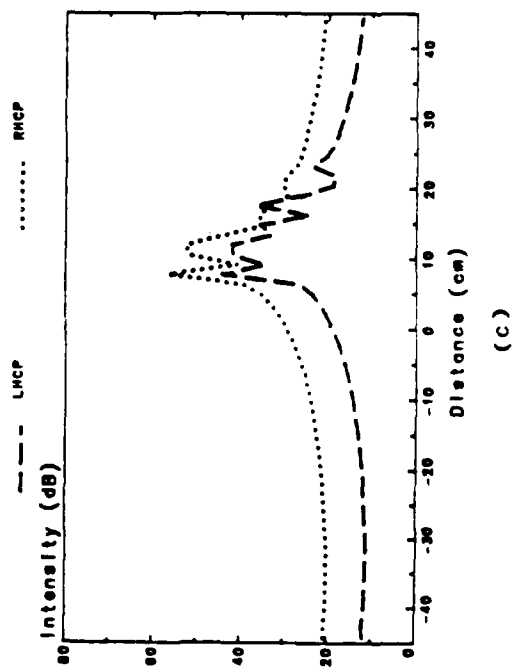
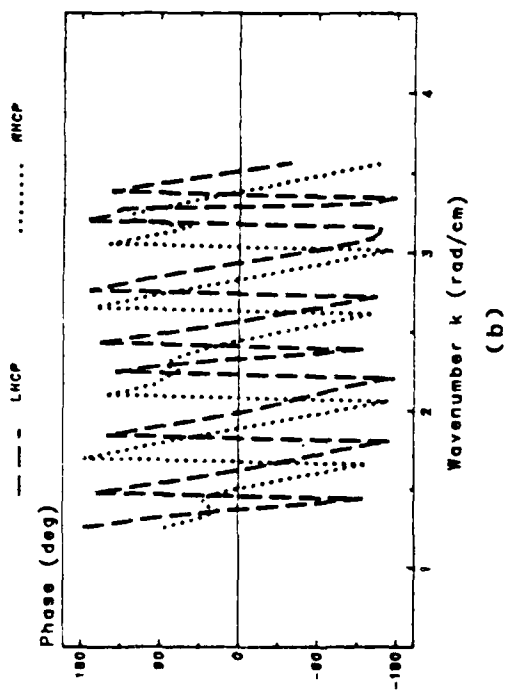
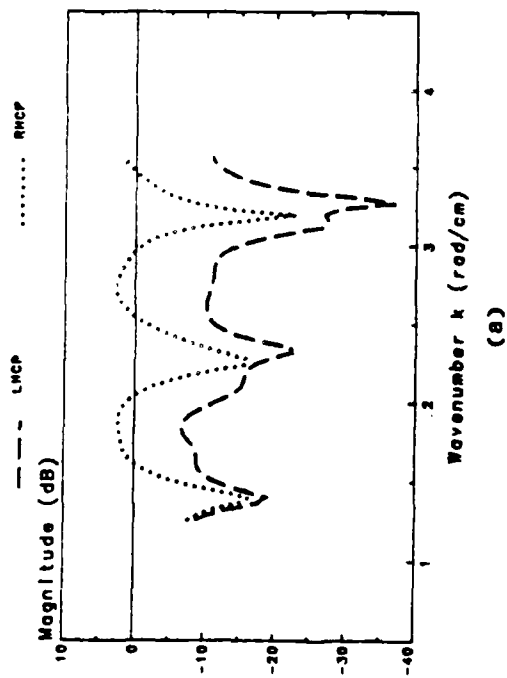
(b)

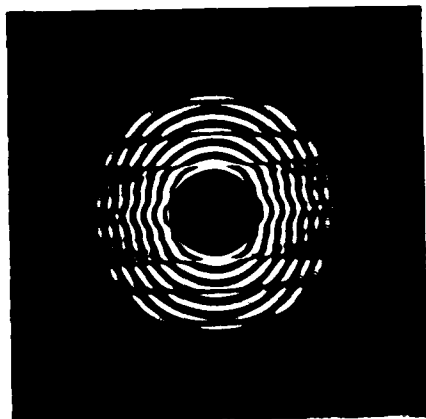


(a)

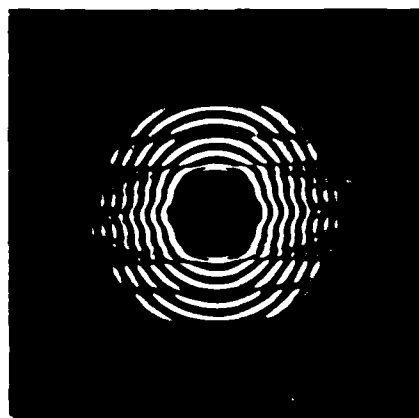


(b)



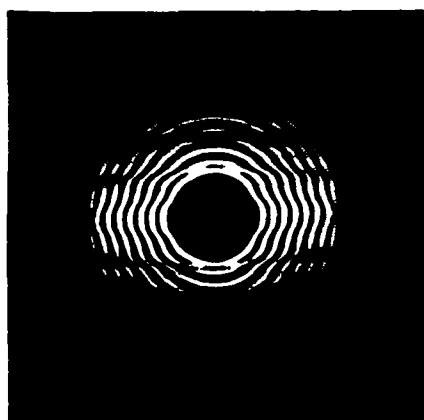


Real part

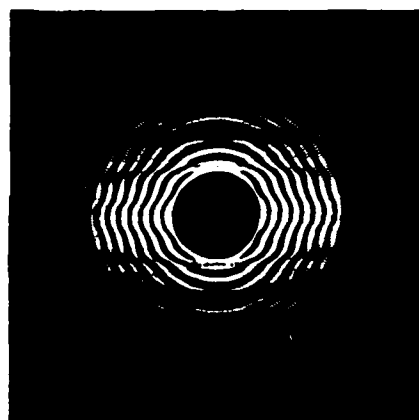


Imaginary part

(a)

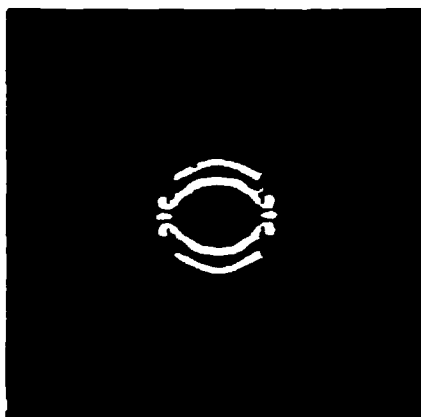


Real part

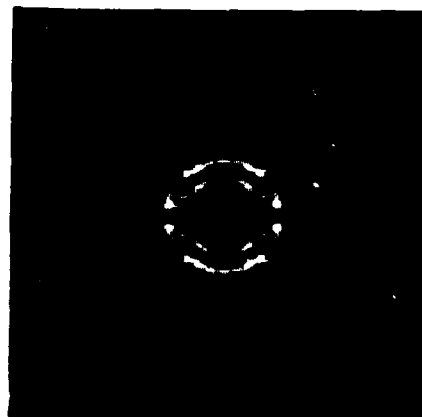


Imaginary part

(b)



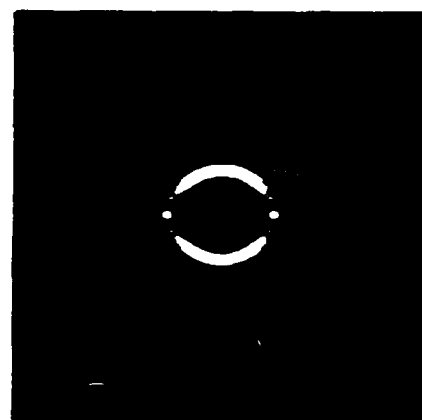
(a)



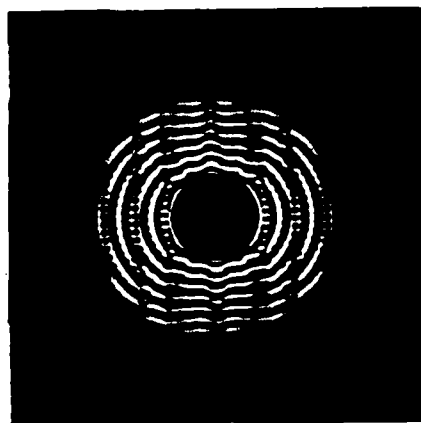
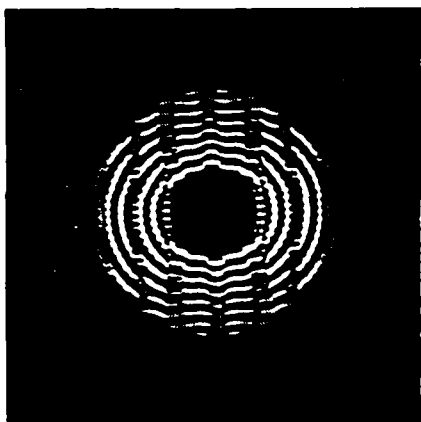
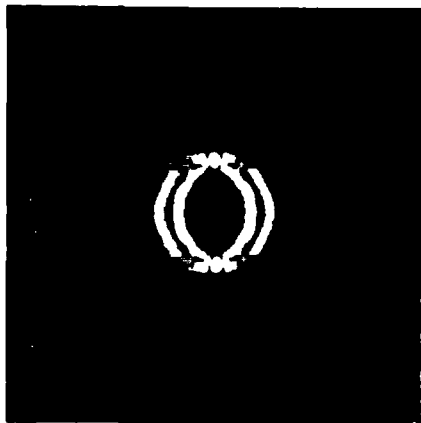
(b)



(c)



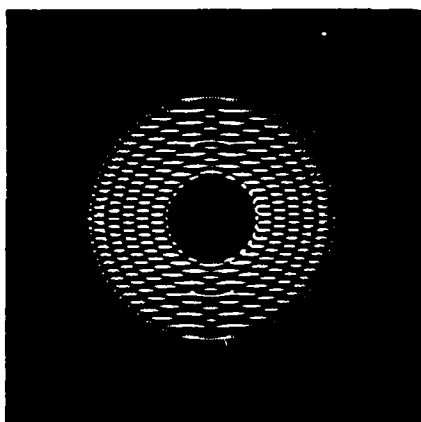
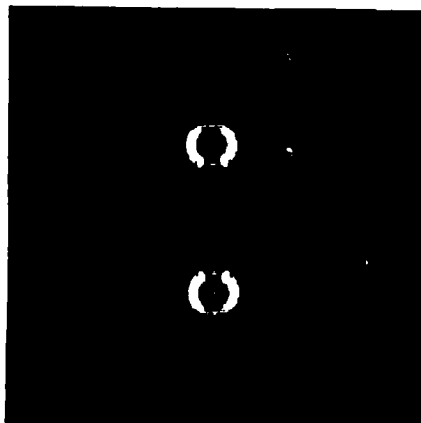
(d)



Imaginary part

(a)

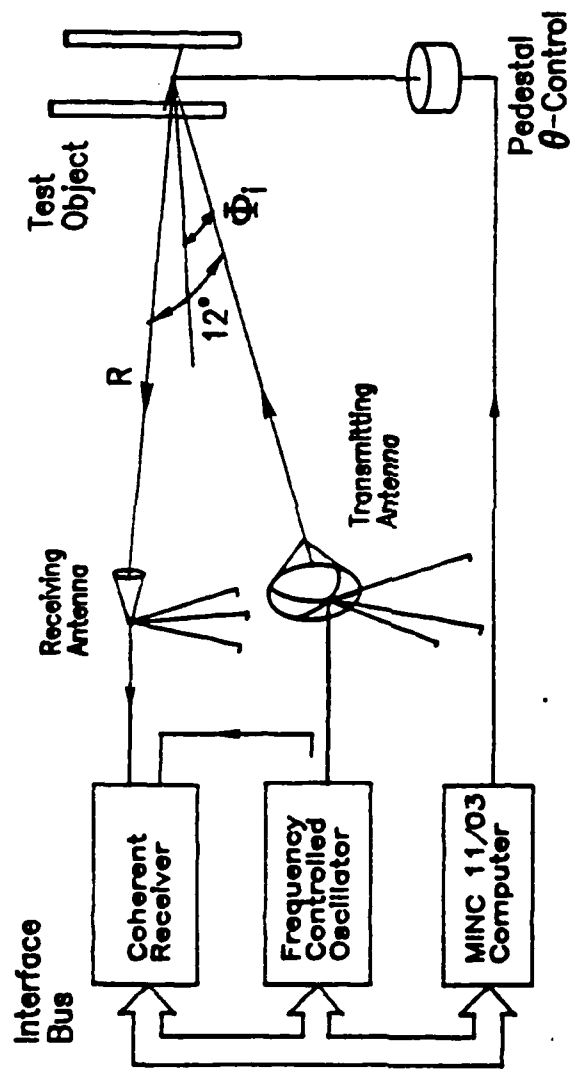
Real part

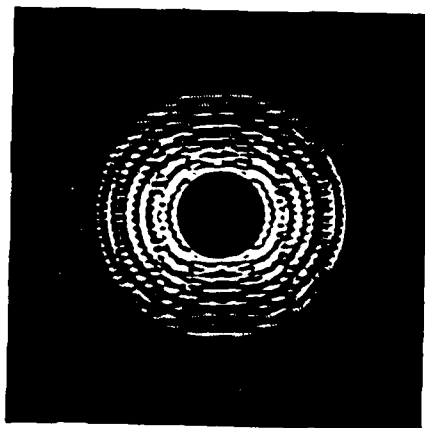
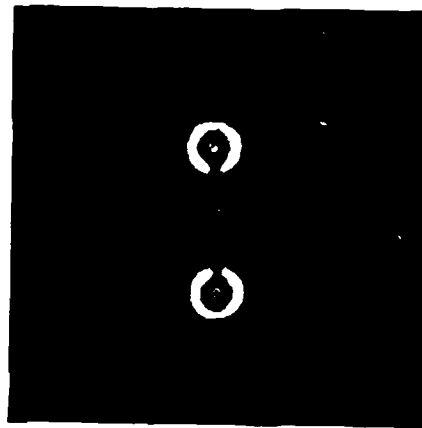
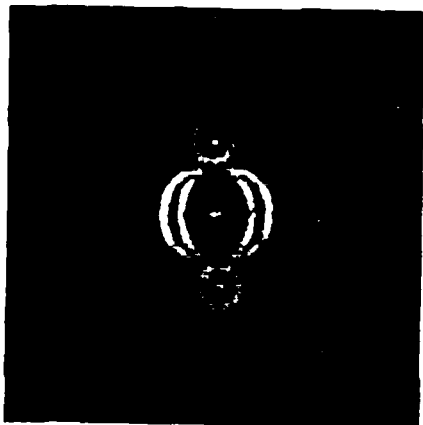


Imaginary part

(b)

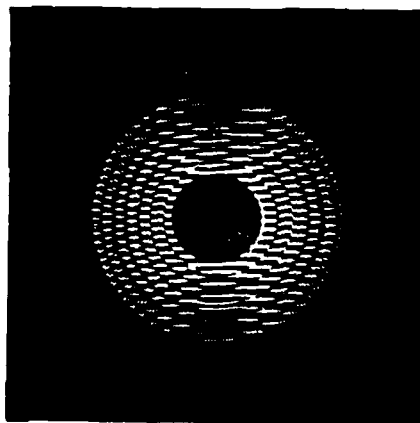
Real part





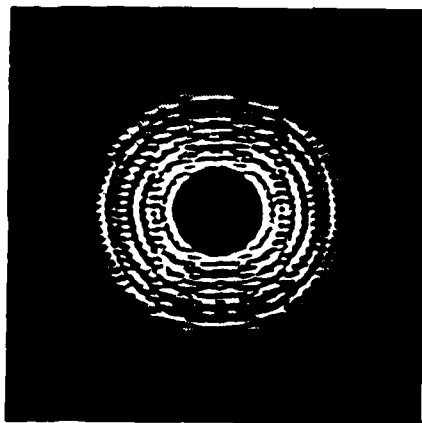
Imaginary part

(a)

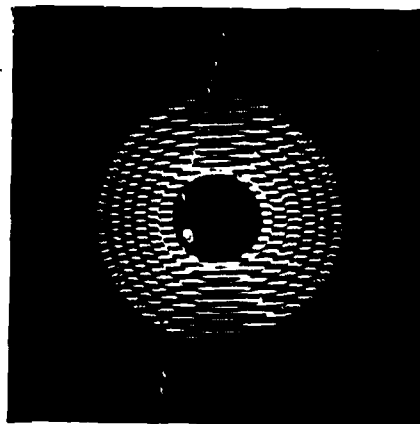


Imaginary part

(b)



Real part



Real part

APPENDIX II

MICROWAVE DIVERSITY IMAGING OF OBJECTS IN THE PRESENCE
OF SEVERE CLUTTER

Nabil H. Farhat and Yuhsyen Shen

University of Pennsylvania
The Moore School of Electrical Engineering
Electro-Optics and Microwave-Optics Laboratory
Philadelphia, PA 19104

ABSTRACT

Microwave diversity imaging techniques in which spectral angular (aspect dependent) and polarization degrees of freedom are employed in image formation are shown to be effective in high resolution projection imaging of targets in the presence of severe clutter. Principles, methodologies, and experimental results demonstrating this capability are presented. Implications of the results for air-borne or space-borne down looking imaging radars and imaging of internal structure of penetrable objects are also discussed.

I. INTRODUCTION

Frequently microwave imaging situations arise where the object being imaged is situated against a strongly reflecting background that produces severe clutter or is obstructed by clutter producing surfaces or foreground. Examples are found in air-borne or space-borne down-looking imaging radars and systems for the imaging of internal structure of penetrable bodies. The aim of this paper is to demonstrate the capability of a high resolution microwave diversity imaging system in discriminating objects of interest in the presence of such severe clutter. The approach is based on a *spot-light* imaging mode in which spectral, angular, and polarization diversities are utilized to access the three-dimensional Fourier space of a coherently illuminated microwave scene. A brief theoretical review of the principle is presented followed by a description of the microwave imaging configuration employed in collecting realistic data of a representative situation: that of a low flying aircraft. The antennas in the imaging configurations studied are positioned as if they were space-borne looking downward towards the target and the ground. Only one two-dimensional slice of the three-dimensional Fourier space is obtained; hence the reconstructed image is a projective side-view. The reconstructed images show clearly the ability to distinguish the object image from the background clutter simulated in our experiments by ground planes overlaid by crumbled aluminum foil. The

polarization-enhanced microwave images obtained are comparable visually to high contrast side-view photographs of the scene taken with flood light illumination. Finally the effect of relative motion and how to account for it in the measurement is discussed. The results shown demonstrate clearly the ability to form recognizable high resolution images of complex scatterers in the presence of severe clutter.

II. THEORETICAL BACKGROUND

It has been demonstrated that by combining angular, spectral, and polarization diversities in a coherent imaging system, projective or tomographic images of complex shaped conducting bodies can be obtained with near optical resolution [1]. The principles on which such a system is based are obtained from inverse scattering theory [2,3,4], which shows that under the physical optics and Born approximations, the scalar component associated with one polarization of the fields scattered in the direction of the unit vector \hat{l}_R and observed at a distance R from an object illuminated by a plane wave incident in the direction of the unit vector \hat{l}_i is given by [5]

$$\psi(\bar{p}, R) = \frac{jAk}{2R} e^{-jkR} \int_{-\infty}^{\infty} \gamma(\bar{r}) e^{j\bar{p} \cdot \bar{r}} d\bar{r} \quad (1)$$

where $\gamma(\bar{r})$ is the object scattering function which is a function of positional vector \bar{r} referred to an arbitrarily chosen reference origin in the object. $\gamma(\bar{r})$ represents the 3-D distribution of scattering centers on the target, assumed to be non-dispersive, i.e., γ is independent of frequency ω , and as such is closely related to the surface contour of the object. The vector $\bar{p} = k(\hat{l}_R - \hat{l}_i)$, is the positional vector in the Fourier space. In particular, $\bar{p} = 2k\hat{l}_R$ in the monostatic case, i.e., when transmitter and receiver (T/R) antennas are closely positioned. $k = \omega/c$ is the wavenumber, c being the velocity of light.

By correcting for the range-related term in front of the integral in eq. (1), we obtain a three-dimensional Fourier transform relationship between the corrected data and the object scattering function,

$$\Gamma(\bar{p}) = \int_{-\infty}^{\infty} \gamma(\bar{r}) e^{j\bar{p} \cdot \bar{r}} d\bar{r} = -j \frac{2\pi R}{Ak} e^{jkR} \psi(\bar{p}, R) \quad (2)$$

This permits the retrieval of $\gamma(\bar{r})$ by Fourier inversion of the measured data ψ corrected for the range dependent factor preceding the integral in eq. (1). Techniques for determining R with sufficient accuracy to perform the range correction and for correcting for the frequency response of the measurement system were described elsewhere [1]. Note that the \bar{p} -space data, or $\Gamma(\bar{p})$, can be acquired over different values of \bar{p} by varying \hat{l}_R , \hat{l}_I , and k . *Angular diversity*, or angular degrees of freedom involve changing \hat{l}_R and/or \hat{l}_I while varying k involves spectral degrees of freedom and is referred to as *spectral diversity*. The object scattering function depends generally on polarization, which allows us to exploit *polarization diversity* to further enrich the accessed volume of the Fourier space with polarization related information about the object. Even though physical optics considerations predict no depolarization in monostatic scattering measurements some depolarization exists in practice. (Depolarization effects become markedly noticeable for the bi-static case). In the experiments described below the co-polarized and cross-polarized components of the scattered field are measured for different status polarization of the incident illumination and the image intensities formed from them are added to obtain a polarization enhanced image. A more detailed discussion of the role of polarization in microwave diversity imaging will be given elsewhere [5].

The reconstructed image quality depends on the size of the \bar{p} -space accessed by measurement. The size of \bar{p} -space depends on the values of \bar{p}

realized in the measurements as imposed by the spectral and angular windows realized by the measurement gear. In order to avoid aliasing of the retrieved image care must be taken to choose the values of \bar{p} so as to satisfy the Nyquist criterion.

The inherently two-dimensional nature of most image display devices leads to two types of two-dimensional presentation that are of prime interest. One is *tomographic*, or cross-sectional, presentation of a three-dimensional object. Given the acquired $\Gamma(\bar{p})$ data in three-dimensional \bar{p} -space, one may use the *weighted projection-slice theorem* [6], which is the generalization of the well-known *projection-slice theorem* [7], to reconstruct and display a specific tomogram of the three-dimensional object. The other presentation is a *projective image* of the three-dimensional body. From the projection-slice theorem, the projective image can be reconstructed from a central slice, or meridional slice of \bar{p} -space data. The imaging geometry to be described in the next section accesses one such meridional slice, hence the retrieved images presented here are projective.

III. SIMULATION GEOMETRY AND EXPERIMENT

Figure 1 depicts the situation to be simulated, in which a space-borne imaging platform containing a coherent broad-band T/R system is looking downward toward an aircraft flying at low altitude. The imaging platform tracks the aircraft in a *spot-light* fashion. For simplicity, we assume that the platform moves relatively much faster than the aircraft, and that during the period in which the platform acquires data for one aspect look of the aircraft, the change in aircraft is negligible. In actual situations, this assumption is not valid. Doppler shift caused by the variation of distance between the platform and the aircraft during the data acquisition period of

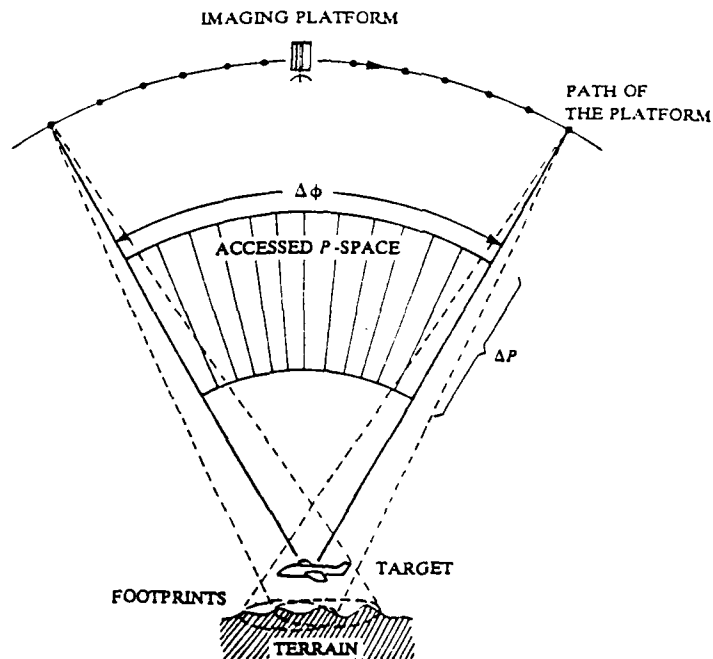


Fig. 1. Simulated imaging geometry.

one look complicates the data acquisition as well as data processing. What we simulate here is an ideal case which removes the unwanted complexity to show what can ultimately be achieved with an imaging system that can account for the doppler shift and hence can access the 3-D Fourier space of target in the presence of relative motion. Also shown in Fig. 1 is the \bar{p} -space data accessed, where $\Delta p = 2\Delta k = 2\Delta\omega/c$, is proportional to the spectral window $\Delta\omega/2\pi$ utilized. Note that the data lie on a polar grid. It represents a meridional slice of the three-dimensional \bar{p} -space or Fourier space of the object. Thus the retrieved images will be projective, with projection direction perpendicular to the plane of the \bar{p} -space slice.

To simulate strong ground clutter, a light caruboard plate covered with a layer of crumbled aluminum foil is employed as a roughened ground plate or background. Two such plates are used; one with rms height variation greater than the mean wavelength of the spectral window employed, the other with rms

height variations less than the mean wavelength. The clutter plate is mounted on a styrofoam support with a 75:1 metalized scale model of the space shuttle placed in front of the plate at a distance representing altitude as depicted in Fig. 2. The transmitting/receiving (T/R) antennas are oriented as if they were looking downward towards the target. A small bistatic angle $\alpha \approx 15.6^\circ$ between the T/R antennas, is used to allow insertion of an absorbing isolating screen to minimize coupling between them. Thus the scattering geometry is not strictly monostatic and the effect of finite α can be seen from $\vec{p} = k(\hat{l}_R - \hat{l}_i) = 2k \cos \frac{\alpha}{2} \hat{l}_p$ where \hat{l}_p is a unit vector in the \vec{p} direction bisecting α and α is the bistatic angle. The effective frequency is therefore the actual frequency multiplied by $\cos(\alpha/2)$.

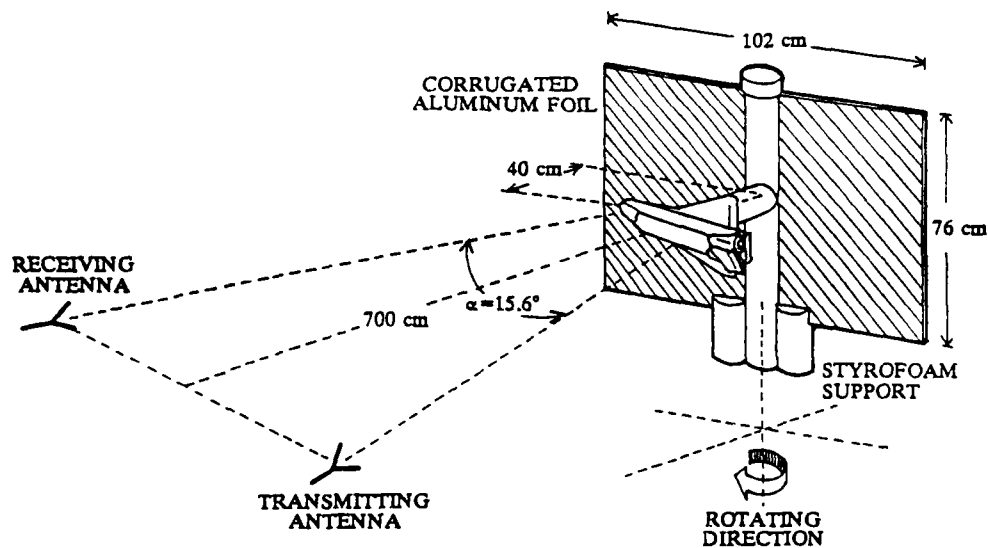


Fig. 2. Experimental imaging arrangement.

High resolution can be achieved through the use of wide spectral and angular windows. In principle narrow impulsive illumination with wide spectral content can be used to achieve good range resolution, but usually is difficult to implement with sufficient power. Dispersed pulses together with post-detection com-

pression may provide both the power and spectral window width needed. But this approach can be restricted by the detector bandwidth, which is typically a fraction of the central frequency. The availability of computer-tunable wide band RF sources, e.g., sweep oscillators and synthesizers, makes it feasible to generate effectively an extremely narrow pulse using frequency synthesis. This indirect pulse synthesis is the approach we take to achieve high resolution. Typically a spectral window of $\Delta f \approx 11$ GHz covering a frequency range from 6.1 to 17.5 GHz is used. The number of frequency increments used to cover this spectral range was 128. This provides a range resolution $\delta R = c/2\Delta f$ of better than 1.5 cm. The angular window $\Delta\phi$, seen in Fig. 1, used in acquiring data in the results presented below covered 90 degrees. The number of angular samples or looks in each window is 128.

Data for four possible combinations of circular polarization states of the T/R antennas are collected. These are designated in accordance to the receiver and transmitter polarizations following the nomenclature used in [8]. For example, RL represents the data collected by a right hand circularly polarized (RHCP) receiving antenna when the object is illuminated by a left hand circularly polarized (LHCP) plane wave produced by a LHCP transmitting antenna. When the T/R antennas are of opposite polarization states, we call the measurement co-polarized, because of the phase reversal of the incident wave upon reflection from a metalized object. On the other hand, and for the same reason, cross-polarization applies to measurement when the T/R antennas have identical polarization states. Polarization enhanced images are obtained by incoherent combination of the images retrieved from co- and cross-polarized Fourier space data.

IV. EXPERIMENTAL RESULTS

Techniques for minimizing anechoic chamber clutter and for correcting the data for the measurement system response and for the range-related term in eq. (1) are described in details in [1]. After the correction, the \bar{p} -space data, which is obtained in polar format, are interpolated onto a Cartesian grid to facilitate image retrieval by Fourier inversion using the fast Fourier transform (FFT) algorithm. A four nearest neighbors interpolation [6] is used. The real (top) and imaginary (bottom) parts are shown on the left together with the reconstructed image on the right. The data and the image shown are of the space shuttle alone without the clutter plate in position when the receiver is LHCP and the transmitter is RHCP i.e., a co-polarized image, hence the designation LR in the caption of this figure.

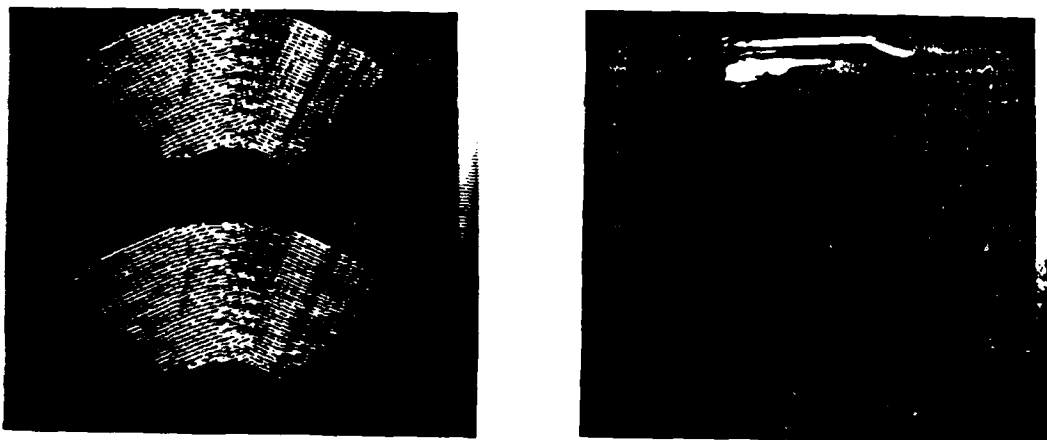


Fig. 3. Interpolated \bar{p} -space data (left) and image (right) of the space shuttle. Co-polarized or LR case (R-LHCP, T-RHCP).

The \bar{p} -space data and the image of the same polarization states when the rougher clutter plate was placed as background behind the shuttle are shown in Fig. 4. We note that the fringes in the \bar{p} -space data are dominated now by those produced by the clutter plate, and that only at central aspect looks one can distinguish fringe structure due to the shuttle.

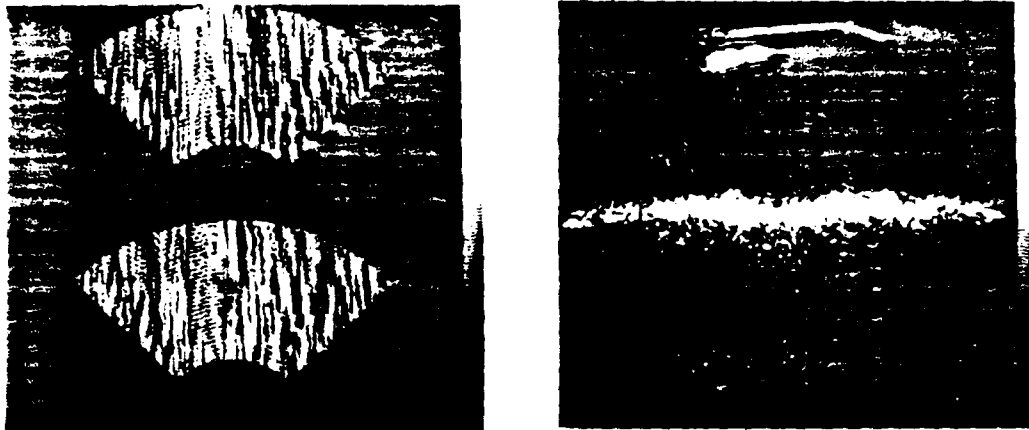


Fig. 4. \bar{P} -space data (left) and image (right) of the shuttle above the rougher ground plate. Co-polarized or LR case. (R-LHCP, T-RHCP).

Figure 5 shows the results obtained with the same conditions of Fig. 4 except that the polarization state is now RR. It can be seen that the image of the clutter plate is seen to be similar to the LR case, but the image of the specularly reflecting shuttle model is somewhat different containing some complementary information.



Fig. 5. \bar{P} -space data (left) and image (right) of the shuttle above the rougher ground plate. Cross-polarized case (R-RHCP, T-RHCP).

The polarization enhanced image, the result of adding the image intensities of Figs. 4 and 5, is shown in Fig. 6 together with a high contrast pictorial side view of the space shuttle on its mount shown for comparison taken under flood-light conditions to emphasize similar outline. The similarity of the two images is striking. Most of the features of the shuttle are present without much degradation by the influence of the clutter plate. This is attributed primarily to the wide dynamic range of the measurement system estimated to be 68 dB, which enables the delineation of weak scattering detail in the presence of strong scatterers, and due to the excellent range resolution (~ 1.5 cm) which enables isolating the clutter image spatially.

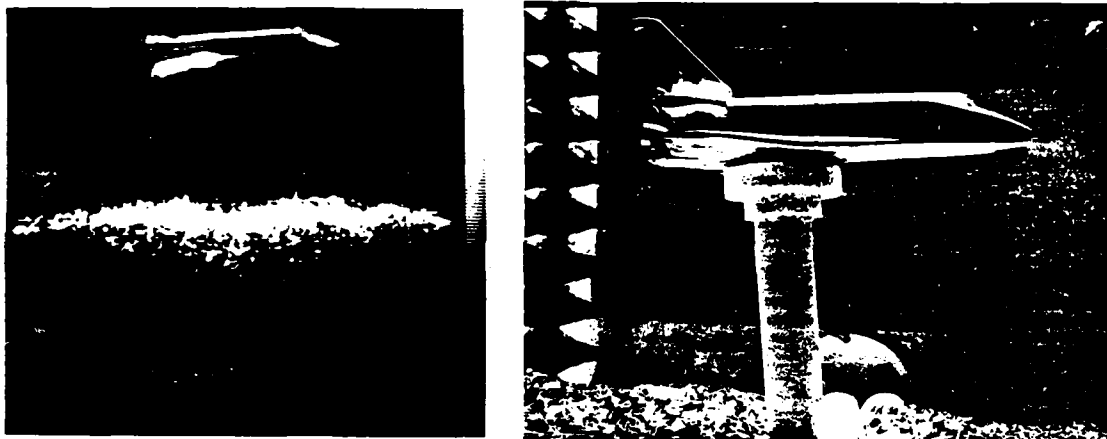


Fig. 6. Polarization enhanced image (RR+LR) (left) and optical image (right).

Enhanced images of the shuttle with each of the two clutter plates (of different rms height variations) are shown in Fig. 7. The image with the smoother clutter plate compares less favorably to that with rougher clutter plate. The shuttle is less visible and artifact is present in the clutter image. The weaker shuttle image is believed to be due to the less diffuse nature of scattering from the smoother plate which tends to produce stronger

backscatter signals than from the rougher plate. One conjecture for the artifact is the multiple reflection between the shuttle, styrofoam support, and the plate. Notice also the appearance of a weak "reflection" image of the shuttle in the smoother clutter plate.

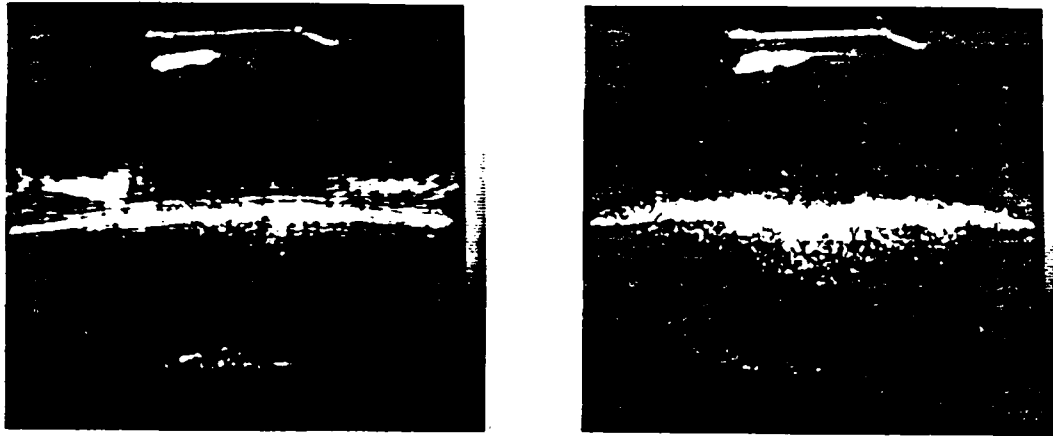


Fig. 7. Polarization enhanced images of the shuttle with different plates. (left: rms height < mean wavelength; right: rms height > mean wavelength.)

V. DISCUSSIONS AND CONCLUSIONS

We have demonstrated for the first time that despite the presence of the relatively strong background clutter, images of high quality can be obtained with a high resolution system. The microwave images are comparable visually to their visual counterparts under mono-directional floodlight illumination. Although for the images shown here a 90 degree angular window is utilized, reduction of the window size down to 30 degrees continued to yield discernible, though somewhat degraded, images of the target.

Separation of the target from the clutter may be desirable. Spatial filtering in the image plane can be employed to achieve this. Coherent subtraction in the \bar{p} -space is another way in which the \bar{p} -space data of the

ground plate alone is subtracted from the \bar{p} -space data of the shuttle plus the ground plate. We find that this latter approach is not easy to implement with our present set-up because of the difficulty of duplicating the exact aspect looks at different runs of experiments. Slight change of the object aspect may not change the magnitude of the \bar{p} -space data, but the phase can be altered noticeably, which makes the coherent removal of the clutter difficult. In actual situations, this strategy is impractical since it requires measurement of the same clutter at exactly the same aspect looks twice; once when the target is present, the other without. The more feasible practice as stated earlier is separating the clutter in the image space by spatial filtering. The one-dimensional FFT of the data at each look is the range profile of the scene at that aspect look. With good range resolution, detail belonging to the image of the object and that of the clutter can be separated.

As mentioned earlier, the simulated conditions in the above study are ideal, i.e., the target motion is ignored. In actuality, the imaging platform and the target are in relative motion. It is however the change of aspect of the object scene during motion that provides image formation; i.e., it is the changes of their relative orientations that contributes to image formation. This has been the central process in the spot-light imaging scheme studied here. The effect of relative motion is merely to introduce doppler shift in the frequency of the received echo. Compensating for the doppler shift in the measurement methodology described here would allow accessing the \bar{p} -space of a moving target in the manner described above. Methods for removing the doppler shift caused by relative motion are currently under study. One promising method being studied utilizes what we call "orchestrated frequency response measurement" in which the doppler shift of the echo relative to the

transmitted signal is rapidly determined and the information used to set the frequency of a synthesized source used as local oscillator for the receiver to a value needed to compensate for doppler shift. The L.O. synthesizer in this scheme is phase-locked to a transmitter synthesizer providing the object illumination. Equipment for performing this study obtained under a \$350K DoD/URIP grant is presently being assembled. The result of this study will be reported on in the near future.

VI. ACKNOWLEDGEMENT

The work reported here was supported by a grant from General Electric Co. and under partial support from the Air Force Office of Scientific Research.

VII. REFERENCES

1. N.H. Farhat, et. al., "Prospects for Three-dimensional Projective and Tomographic Imaging Radar Networks," Radio Science, Vol. 19, No. 5, pp. 1347-1355, Sept.-Oct. 1984. (see also Appendix I of this document)
2. R.M. Lewis, "Physical Optics Inverse Diffraction," IEEE Trans. on Antennas & Propagations, Vol. AP-17, pp. 308-314, 1969.
3. N. Bojarski, "Inverse Scattering," Final Report N000 19-73-C-0312F, Nav. Air Syst. Command, Warminster, PA., February 1974.
4. S.R. Raz, "On Scatterer Reconstruction from Far-field Data," IEEE Trans. on Antennas & Propagations, Vol. AP-24, pp. 66-70, 1976.
5. T.H. Chu and N.H. Farhat, "Polarization Effects in Microwave Diversity Imaging of Conducting Cylinders," submitted for publication.
6. C.K. Chan and N.H. Farhat, "Frequency Swept Tomographic Imaging of Three-Dimensional Perfectly Conducting Objects," IEEE Trans. on Antennas & Propagations, Vol. AP-29, pp. 321-319, 1981.
7. R.M. Mersereau and A.V. Oppenheim, "Digital Reconstruction of Multidimensional Signals from Their Projections," Proc. IEEE, Vol. 62, pp. 1319-1338, 1978.
8. G.T. Ruck, et. al., Chapter 2 in Radar Cross Section Handbook, Vol. 1, G.T. Ruck (Ed.), Plenum Press, New York, 1970.

APPENDIX III

A MULTIFUNCTIONAL MICROWAVE/MILLIMETER WAVE MEASUREMENT FACILITY FOR MULTISTATIC IMAGING AND TARGET CLASSIFICATION STUDIES

N. Farhat and Y. Shen

I. INTRODUCTION

A measurement system capable of acquiring data covering the microwave/millimeter-wave ($\mu\text{w/mm}$) region of the spectrum is a valuable tool in many areas of research. For example, in the study of inverse scattering, the scattered fields from a test object are dependent on the wavelength of the illumination, therefore the availability of scattered data over a wide bandwidth would be important in gaining insight into the scattering phenomenon and in characterizing the object. In the areas of coherent imaging, the wide bandwidth implies better range resolution which leads to high resolution images that are suited for recognition by the human eye-brain system as in microwave and millimeter wave diversity imaging where angular, spectral, and polarization degrees of freedom are combined to cost-effectively form images of scattering objects with near optical resolution.

It is well known that combinations of different polarization states of the incident field and of the antennas receiving the scattered field provide different information about the scatterer. A total of four polarization state combinations, corresponding to the four elements of the scattering matrix, is therefore needed to fully characterize scattering by an object,

provided that other factors such as antenna positions remain fixed. Thus being able to change the polarization states of the incident field and of the antennas measuring the scattered field is important in the study of depolarization effects and target identification utilizing polarization descriptors. It is also worth noting that polarization effects are more pronounced in multistatic and bistatic measurements than monostatic measurement.

Besides the bandwidth and the polarization considerations, the scattered fields are also dependent on the locations and the directions of the transmitting and the receiving (T/R) antennas. A system that allows change in the locations and the orientations of the T/R antennas is useful in aperture synthesis and in bistatic and multistatic scattering and imaging studies. The system can also be used to study the scattering effects in different radiation zones, e.g. near field versus far field coherent imaging.

In summary, a system that provides wide bandwidth, variable polarization states of the incident field and the measured field, and relocatable positions of the transmitting and receiving antennas relative to the object is a highly desirable tool for the study of uw/mmwave scattering, imaging, and target representation. The aforementioned features are also referred to as wavelength, polarization, and positional or angular (aspect related) diversities respectively. In the following sections, a measurement system designed to meet these desirable features is described. The system is an upgraded version of the original 9-2018 GHz system configuration residing at the Electro-Optics & Microwave-Optics Laboratory of the Moore School of Electrical Engineering at the University of Pennsylvania which was utilized in our earlier microwave diversity imaging studies. The upgraded system is intended to extend operational capabilities to 60 GHz and beyond.

multistatic scattering measurements employing the same operation principles as in the original system but employing different gear.

II. ORIGINAL SYSTEM CONFIGURATION

Shown in Fig. 1 is a schematic diagram of the present system operating from 2 to 18 GHz (S, C, X, and Ku bands in the radar letter-band nomenclature). Two microwave sources, a sweeper oscillator (HP-8620C) and a sweep synthesizer (HP-8340A), are available; either one can be used as the illuminating source. The coherent detector is a network analyzer (HP-8410B or HP-8510A) with a reflection/transmission test unit (HP-8743 or HP-8513). The combination of HP-8620C/8410B can operate from 2 to 18 GHz, while HP-8340A/8510A combination allows operation from 40 MHz to 18 GHz. The illuminating signal is amplified by a solid state amplifier (Litt-Meade 100) which furnishes 1 watt in the 2-18 GHz range, and by a TWT amplifier (Varian VEM609K3) with maximum 10 Watts output power in 2-18 GHz range. In the case of the transmitting antenna, the TWT is required to provide 100 Watts or more gain. This is the reason for the use of the TWT in the low frequency range of the 2-18 GHz range. With good network analyzer, the system can be used for

[illegible]

A parabolic reflecting antenna (EM Ar 12) is used with a feed horn which may or may not have a circular and both hands in the polarization (EM Ar 13) (Fig. 1). Transverse plane is used in the EM Ar 12 antenna, which is only suitable for illumination. The receiving antenna is a half-wave antenna (EM Ar 14) with a 90 degree hybrid for circular polarization measurement. To obtain measurements of horizontal and vertical (H/V) polarizations, a pair of dual polarization horns (EM Ar 15) is used without the hybrid. For circular

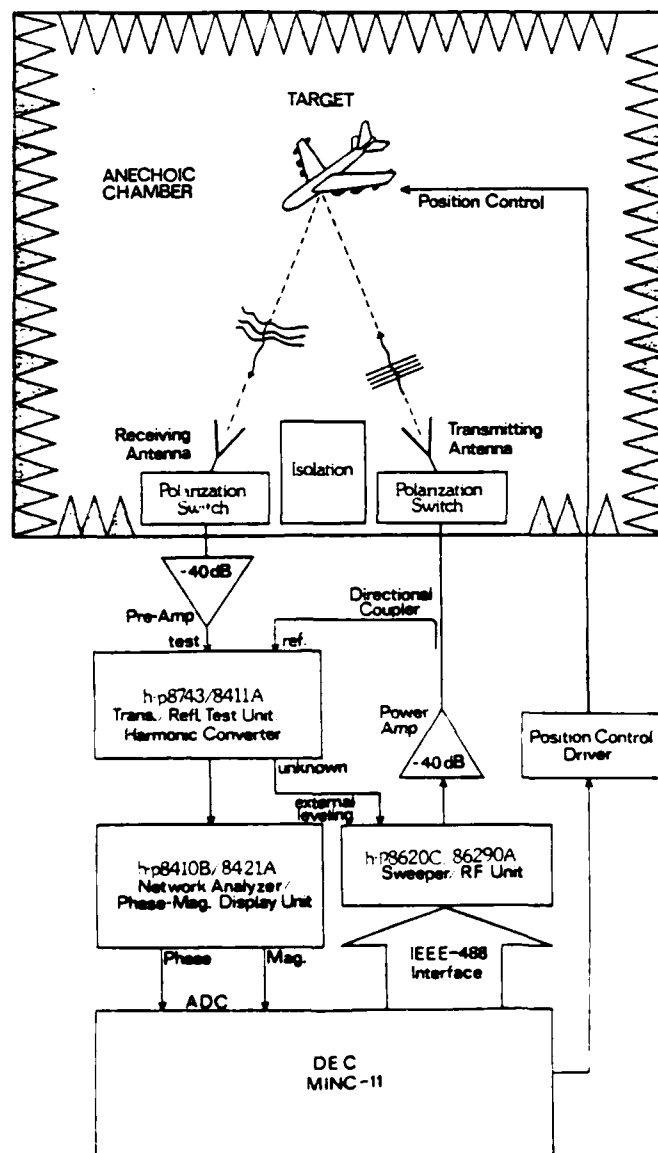


Fig. 1. Experimental Microwave Measurement and Imaging Facility (original system configuration)

polarization states of the RHCP/LHCP measurements are switched manually, while those of the H/V polarization measurements can be switched electronically.

The received field is amplified by low noise solid-state amplifiers, an Avantek AWT-8035M in 2-8 GHz and an Avantek AWT-18039M in 8-18 GHz, with both having about 50 db gain. The pre-amplifiers are switched manually. The amplified signal is then fed to the test channel of the reflection/transmission test set operating in transmission mode, and detected by the network analyzer.

The test range is a rectangular anechoic chamber with dimensions 50' long, 20' wide, and 20' high. The test object is mounted on a pedestal located at the center of the chamber. The T/R antennas are located at one end of the chamber, with slight angular separation between them for insertion of electromagnetic wave absorbing materials to minimize mutual coupling. The main beams of the T/R antennas are manually steered toward the test object for better signal-to-noise ratio. Aside from the slight bistatic angle between the T/R, the arrangement is essentially monostatic. The pedestal is rotated by a stepping motor to change the aspect angles of the test object relative to the T/R which are stationary.

III. UPGRADED SYSTEM CONFIGURATION

The new system to be described next is an upgraded version of the original system described in the preceeding section with several new salient features added. Many of the components used in the original system are incorporated into the new system. Added features of the new system include:

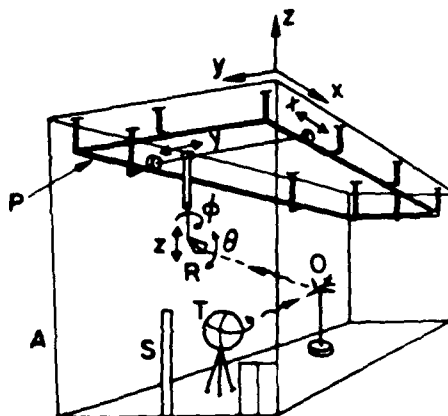
1. Wide bandwidth coverage ranging from 2 GHz to 60 GHz. Thus the operating bandwidth is nearly tripled, covering the microwave region and a

lower segment of the millimeter-wave region. In conventional radar letter-band nomenclature, the system coverage is from S band up to U band. Small frequency gaps may exist between bands due to hardware limitations.

2. Most of the switching between components of different bands are controlled electronically. That part that cannot be switched remotely is due to unavailable hardware. But the system may become fully automated in the future as broadband switches become available.

3. An x, y, z, θ, ϕ positioner that enables positioning a broadband receiver module to nearly any coordinate location in the anechoic chamber and enables orienting the receiver module towards the stationary target greatly enhances the versatility of the new system. Bistatic and multistatic measurements for polarization and aperture synthesis studies that were impossible or difficult earlier can be performed readily with the new system. A sketch of the anechoic chamber depicting the positioner and showing the scattering object located on a separate elevation over azimuth positioner to change the target aspect relative to the receiving module and a stationary transmitter antenna is given in Fig. 2.

Figure 3 depicts the basic blocks of the upgraded system. A central consideration in the design of the upgraded system is the realization of a (2-60) GHz receiver module that is translatable for carrying out bistatic and multistatic scattering measurements. The source generates highly accurate and stable RF signals from 2 to 60 GHz in either sweep mode or stepped frequency CW mode. The transmitter assembly comprises a bank of power amplifiers and the switches needed to guide the signal through an appropriate signal path in accordance with its frequency as detailed in Fig. 4. Part of the amplified signal is coupled out and downconverted to within 18 GHz as the



- A-Anechoic chamber
- T-Transmitting antenna (illuminator)
- O-Test object (scatterer) mounted on its own elevation over azimuth positioner
- R-Positioner mounted receiver module
- P-Positioner frame
- S-Window for cable connections to external instrumentation

Fig. 2. Sketch of anechoic chamber showing receiver module R mounted on x, y, z, θ, ϕ positioner and scattering object O mounted on an elevation over azimuth positioner in front of a stationary illuminating antenna T.

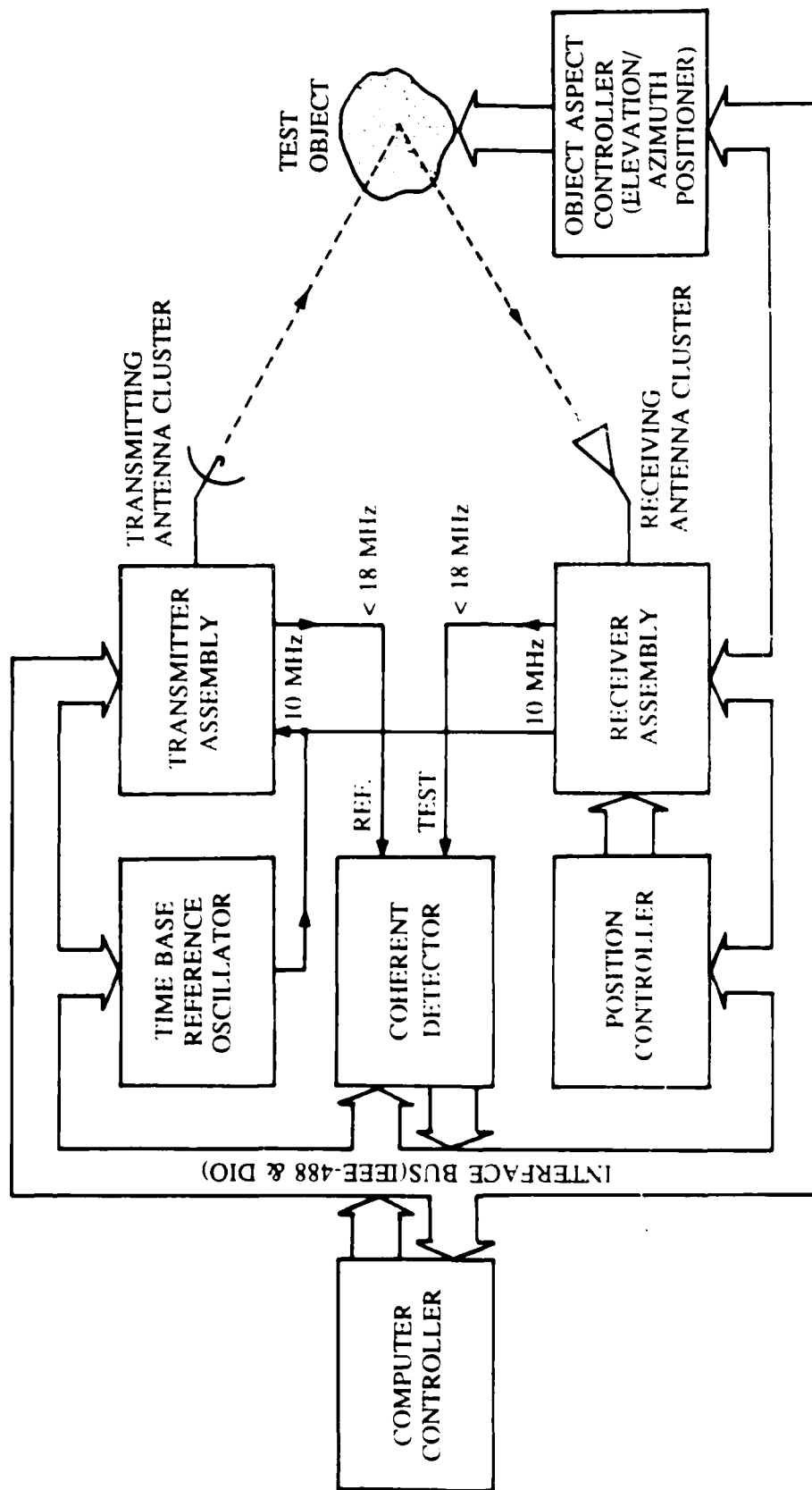


Fig. 1. Block diagram of radar system.

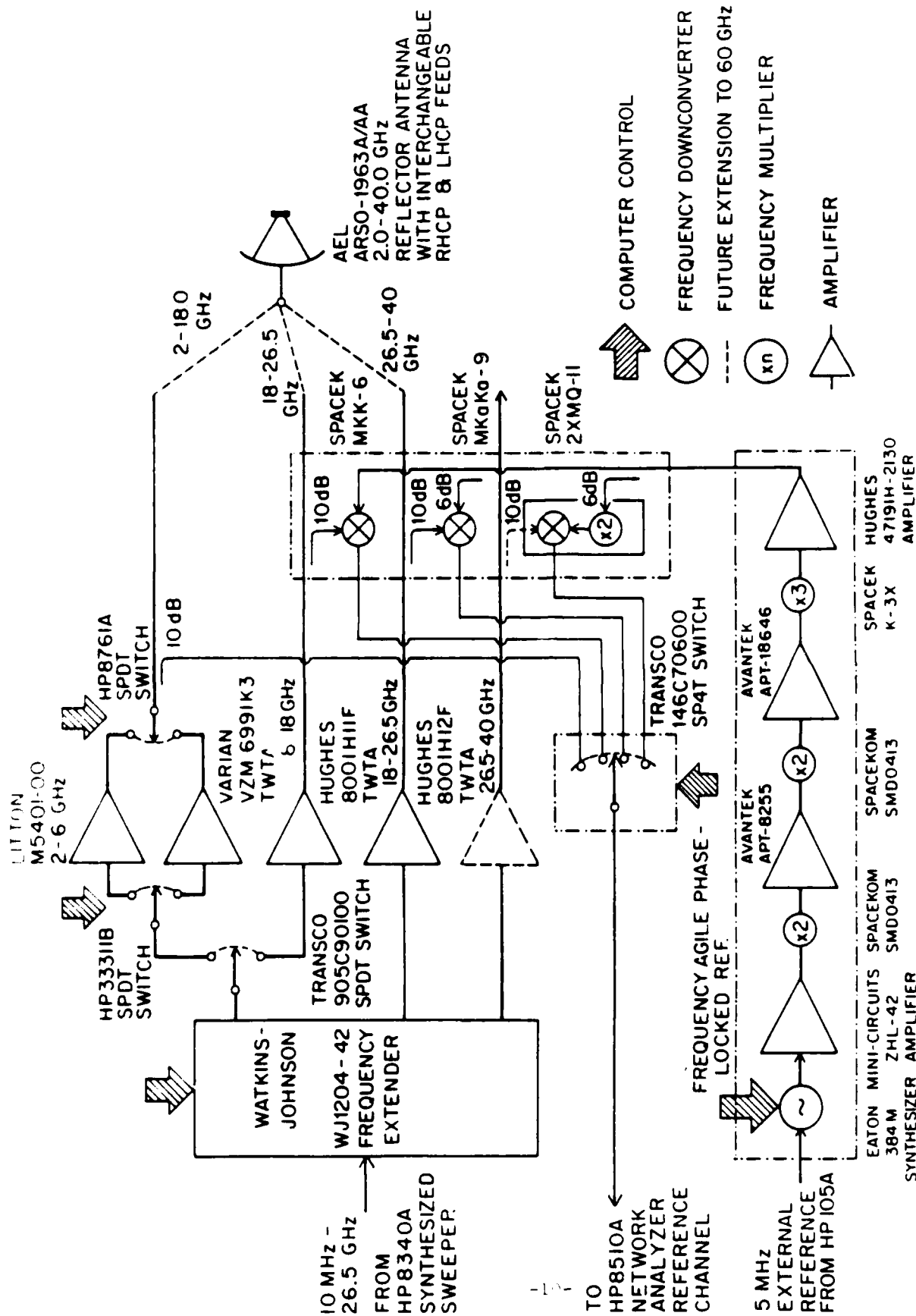


Fig. 4. Detail of (2-60) GHz transmitter assembly.

reference signal for the coherent detector (HP-8510A network analyzer). A local oscillator, phase-locked to a 10 MHz or 5 MHz external reference derived from the time base reference oscillator of the source, furnishes 26.5 GHz for the down-conversion. The major portion of the amplified signal radiates through the transmitting antenna cluster, which consists of high gain antennas of different bands. Further details of the transmitter assembly are given in Fig. 5.

The scattered field is captured by the receiving antenna cluster, the front end of the receiver assembly, shown schematically in Figs. 6 and 7 which consists of several antennas of different bands. The received signal is passed through a bank of switches to effect polarization diversity reception and a bank of low noise amplifiers to attain sufficient signal level for downconversion. Again, a local oscillator, also phase-locked to the 10 MHz or 5 MHz signal derived from the time base reference oscillator of the source, provides the 26.5 GHz reference to downconvert the signal to below 18 GHz. The downconverted signal is then passed through a second bank of amplifiers to increase the power level before being fed to the test channel of the coherent detector (HP 8510A network analyzer) via a low-loss flexible coaxial cable.

The coherent detector is in essence the HP-8510A network analyzer with the HP-8513 reflection/transmission test set. The reference channel input, derived from the transmitted signal, and the test channel input, which is the downconverted returned signal, are again downconverted twice, first to 20 MHz in the HP-8513, then to 100 KHz inside the HP-8510A, before being sampled and fed to the amplitude-phase detector portion of the HP 8510A. The network analyzer is always phase-locked to the reference channel input.

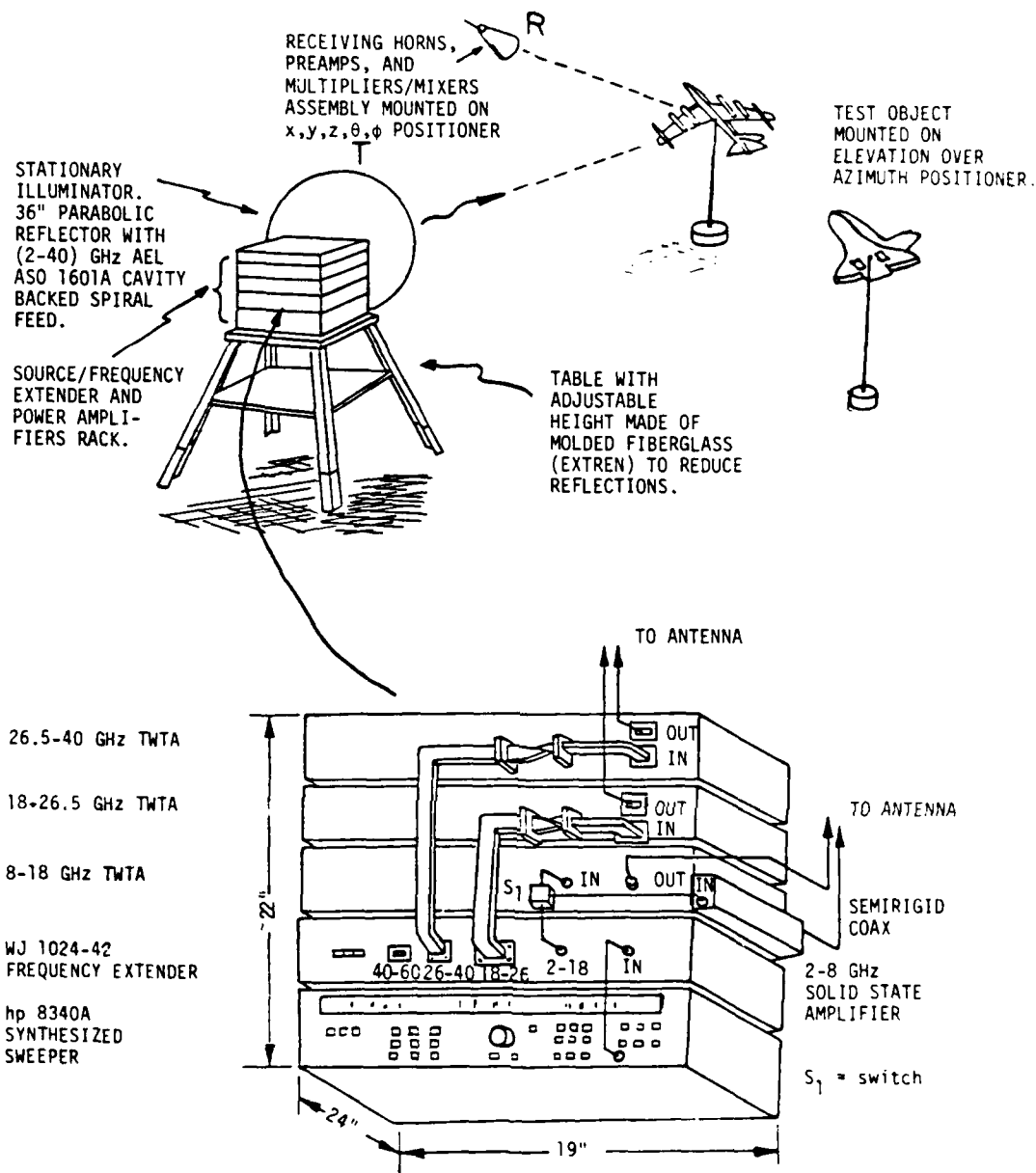
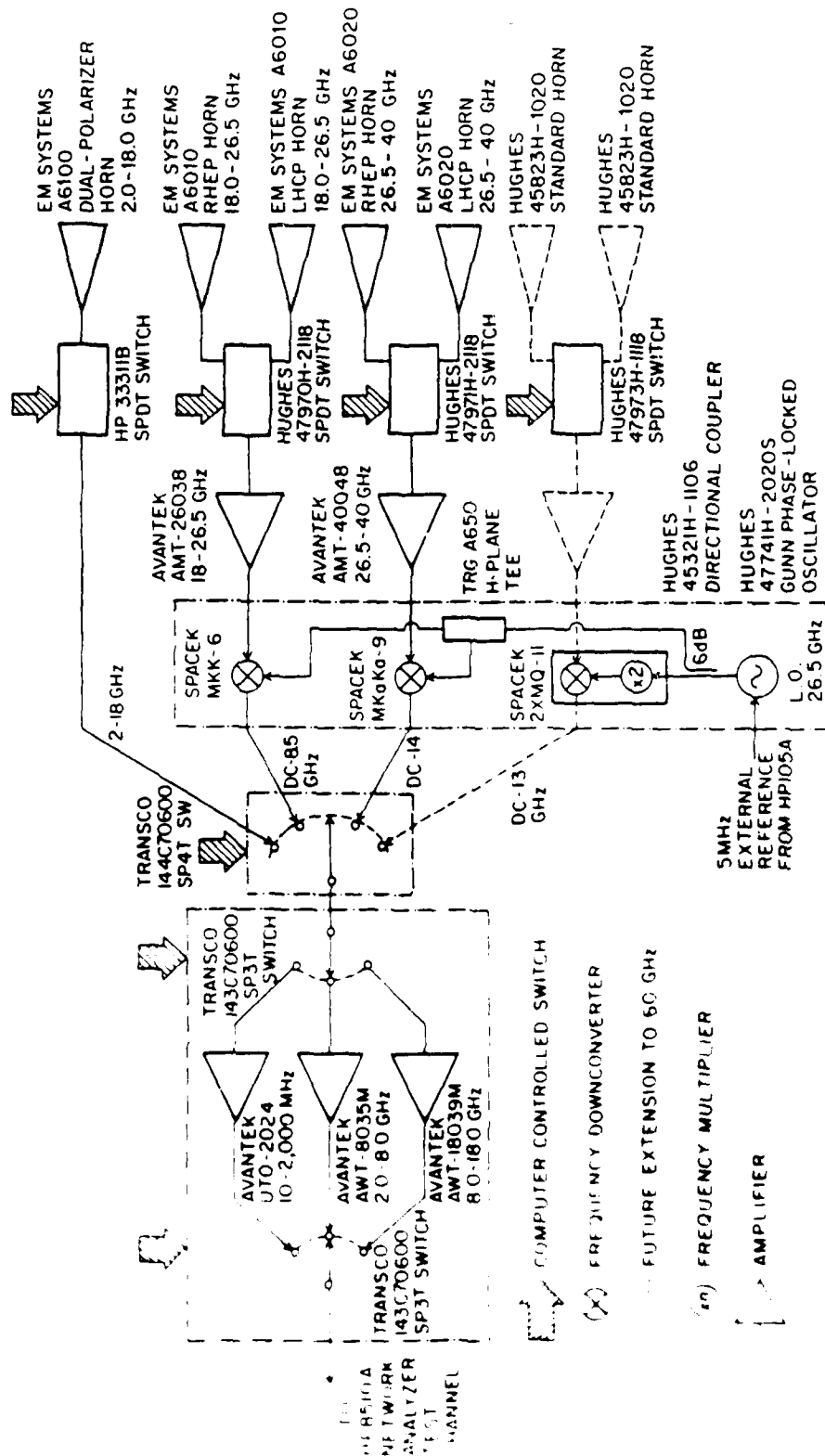


Fig. 5. Transmitter assembly consisting of microwave source (synthesized sweeper), frequency extender, power amplifier pack, and parabolic reflector antenna for use in the study of monostatic and bistatic λ and polarization diversity imaging in an anechoic chamber environment.

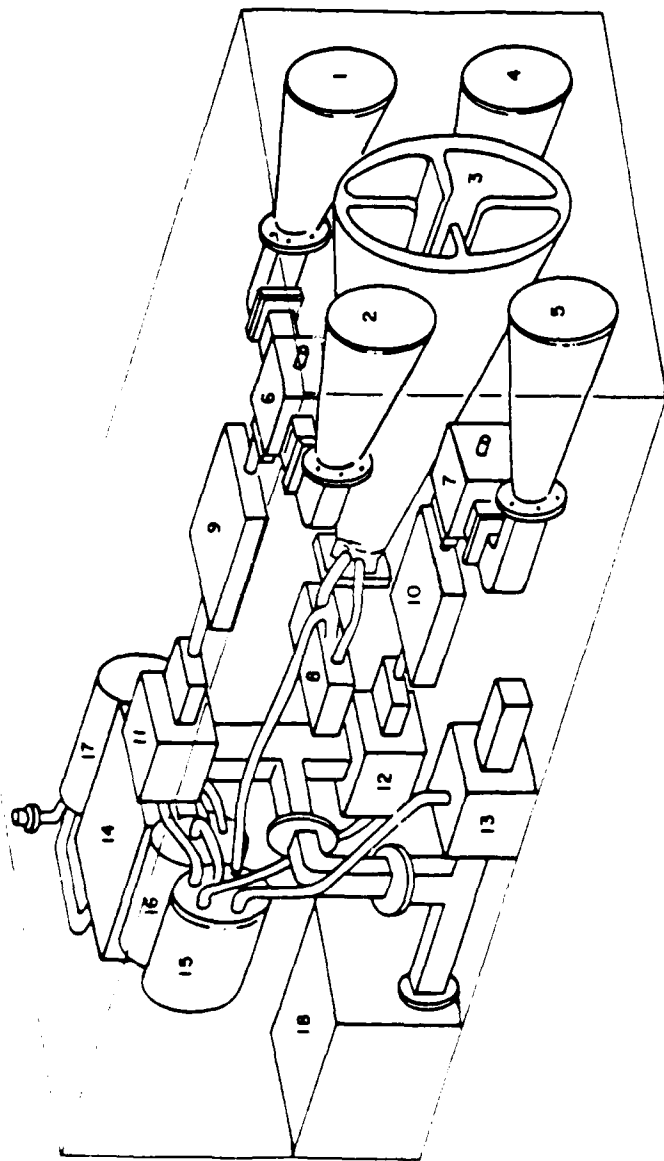
There are two position control interfaces: one is for the receiver module (receiver assembly with the receiving antenna cluster), and the other for the test object aspect control. The receiver module can be moved to almost any location in the anechoic chamber, and be oriented so that the antenna cluster is aiming toward the test object. The test object aspect control is realized by mounting it on an elevation over azimuth positioner. All these units, including the source, the transmitter/receiver assemblies, the coherent detector, and the position controls, are under the coordination of a computer/controller shown in the block diagram of Fig. 3. The computer/controller controls these units via the IEEE-488 bus and parallel digital I/O lines. Next we'll describe each block in Fig. 3 in more detail.

IV. THE SOURCE

A simplified version of the source is shown in Fig. 8. It is comprised of two parts: a HP-8340A sweeper synthesizer and a Watkins-Johnson WJ-1204-42 frequency extender, (see also Figs. 4 and 5). This combination delivers signals with greater than 0 dBm unlevelled power and synthesized frequencies over 0.1-60 GHz range. The HP-8340A covers frequency range 10 MHz to 26.5 GHz with minimum levelled power output of about 5 dBm over the entire frequency range. Levelled power output is somewhat higher for lower frequency. For the WJ-1204-42 frequency extender, 0 dBm input power is sufficient. The synthesizer operates in either CW mode, stepped frequency mode, or sweep mode. The synthesizer is controlled by the IEEE-488 GPIB. A highly stable internal time base at 10 MHz of the synthesizer is also used as the phase-locked signal for the local oscillators in the transmitter/receiver assemblies.



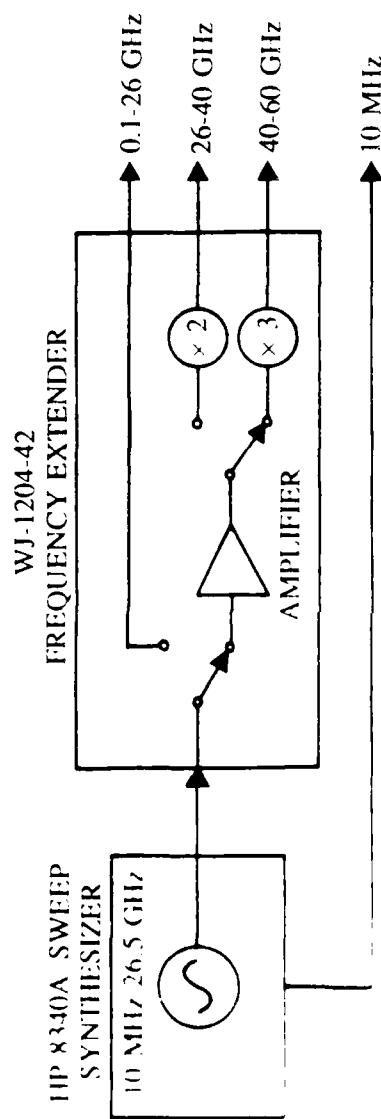
Receiver channel is extendable to 60 GHz. Future extension to 60 GHz is possible. Future extension to 60 GHz is possible. Future extension to 60 GHz is possible.



1. EM Systems A6010 RHCP Horn
2. EM Systems A6010 LHCP Horn
3. EM Systems A6100 Dual-polarized Horn
4. EM Systems A6020 RHCP Horn
5. EM Systems A6020 LHCP Horn
6. HUGHES 47970H-2118 SPDT Switch
7. HUGHES 47971H-2118 SPDT Switch
8. HP 33311B SPDT Switch
9. AVANTEK AMT-26038 Amplifier
10. AVANTEK AMT-40048 Amplifier
11. SPACEK NKK-6 Frequency Downconverter

12. SPACEK Mkaka-9 Frequency Downconverter
13. SPACEK 2xMQ-11 Frequency Multiplier & Downconverter
14. AVANTEK UTO-2024, AWT-8035M, AWT-18039M Amplifiers
15. TRANSCO 144C70600 SP4T Switch
16. TRANSCO 143C70600 SP3T Switch
17. TRANSCO 143C70600 SP3T Switch
18. HUGHES 47741H-2020S Gunn Phase-Locked Oscillator

Fig. 7. Mechanically translatable (2-40) GHz receiver module.



AD-A178 653

STRATEGIES FOR HIGH-RESOLUTION 3-D MILLIMETER WAVE
IMAGING (U) MOORE SCHOOL OF ELECTRICAL ENGINEERING
PHILADELPHIA PA ELECIR. N H FORMAT FEB 87 TO MO-9
ARO-20583.13-EL DANC29-83-K-0120 F/G 14/3

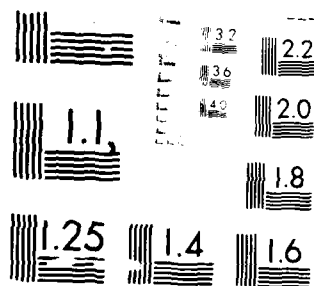
2/2

UNCLASSIFIED

NL



END
DATE
FILMED
5787
DTI



MICROCOPY RESOLUTION TEST CHART
NATIONAL BUREAU OF STANDARDS-1963-A

The WJ-1204-42 frequency extender is in essence a frequency multiplier. It passes the RF 0.1-26.5 GHz signal from the source to one of the three output ports without much attenuation. For higher frequencies, the RF signal is amplified, then switched to either a doubler or a tripler, with the former providing frequencies in the 26.5-40 GHz range, and the latter in the 40-60 GHz range. The minimum unlevelled output power at these ports is -3 dBm at 24.0 GHz. The selection of any of the three output ports is by digital I/O, 3 bits at TTL level.

V. TRANSMITTER ASSEMBLY

A simplified schematic of the transmitter assembly is shown in Fig. 9. The transmitter assembly is a complex of power amplifiers and switches. It also provides the reference signal for the coherent detector as shown earlier in Figs. 4 and 5. The output from the WJ-1204-42 extender is fed into a bank of 5 amplifiers through proper switching. After the amplification, the major part of the signal is directed to the transmitting antenna cluster for illuminating the scattering object, while a fraction of it is extracted to provide the reference signal. The extracted signal is downconverted to below 18 GHz depending on band by a local reference at 26.5 GHz, which is generated by a local oscillator, phase-locked to the time base of the source. The downconverted signal is to be used as the reference for the coherent detector.

The antenna cluster consists of a broadband parabolic reflector (2-40 GHz, 3' diameter). Other antennas covering the 40-60 GHz band are yet to be purchased.* There are two spiral feeds for the parabolic dish, corresponding

*Unanticipated increases in the cost of several components of the system prevented the purchase of these antennas and a 26.5 GHz phase-locked local oscillator. We expect these items to be purchased from future grants in order to extend operation to 60 GHz.

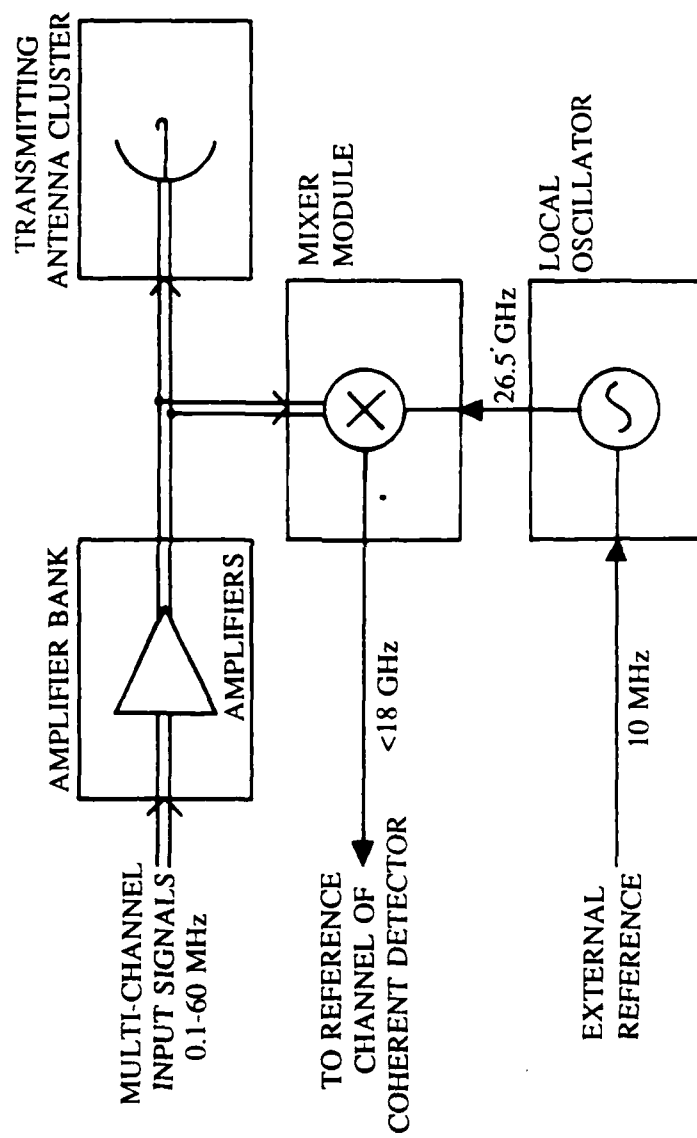


Fig. 9. Simplified version of transmitter assembly shown in Fig. 4.

to RHCP and LHCP respectively. The switching problem between the output of the amplifier bank to the transmitting antenna cluster prevents at present the complete automation of the system. The recent commercial introduction of an electronically controllable switch covering the 2 to 40 GHz band by Tektronix will alleviate this problem. Another problem is the switching of RHCP/LHCP spiral feeds. At present this can only be done manually. A Cassegrain reflector may allow mechanical rotation of the primary feeds if full automation is desirable. Even though semi-automated the present (2-60) GHz system will be of great utility.

VI. RECEIVER ASSEMBLY

The receiver assembly or module is encased in a box (see Figs. 6 and 7), and will be attached to the end of the retractable z-coordinate boom of the x,y,z, θ , ϕ positioner. In addition to the translational movement, the receiver module can be steered angularly to aim the antenna main beams towards the test object. Shown in Fig. 10 is a simplified schematic of the receiver assembly. The front end of the receiver assembly is a cluster of seven horn antennas; one dual-polarizer horn for the 2-18 GHz band, one pair of horns of opposite circular polarization for the 18-26.5 GHz band, and another similar pair for 26.5-40 GHz, and finally a pair of standard gain horns for 40-60 GHz where at present only linear polarization measurements can be conducted. Immediately following the antennas are polarization switches to control the polarization component of the scattered field to be received. The received signal is then amplified to get sufficient power for downconversion to within 18 GHz. A local oscillator, phase-locked to the reference oscillator source time base, provides the 26.5 GHz reference signal

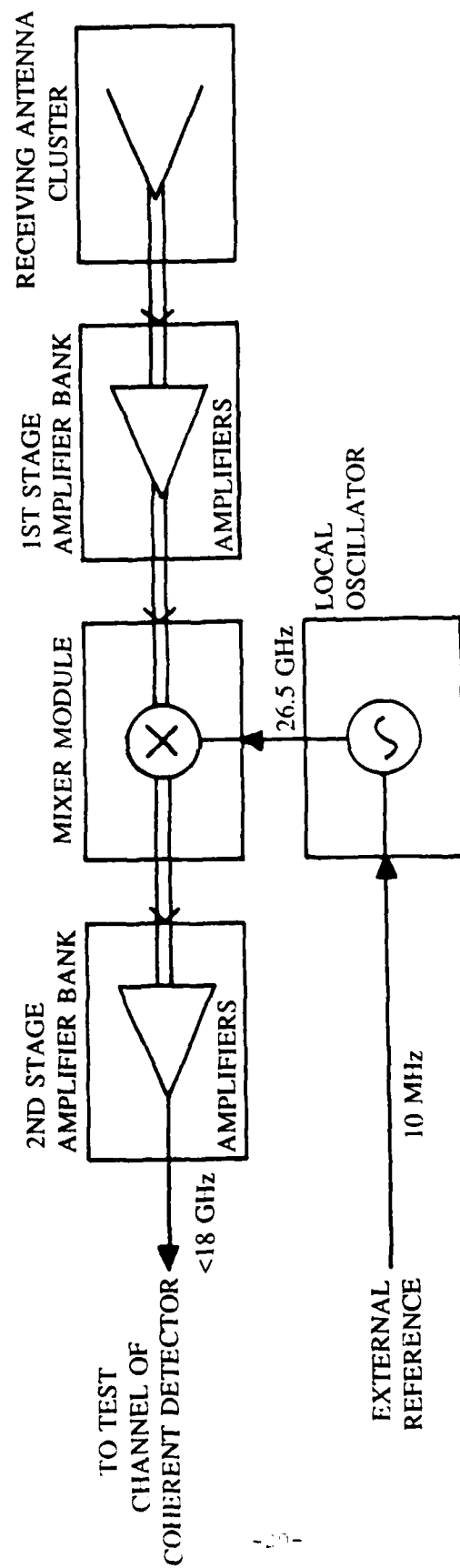


Fig. 10. Simplified version of receiver assembly shown in Fig. 6.

for the mixers. After the downconversion, the signal is passed to the second stage amplifier bank before being relayed by a flexible cable to the coherent detector. The receiver module is therefore translatable and angularly steerable to enable carrying out multistatic measurements.

VII. COHERENT DETECTOR

The coherent detector is the HP-8510A network analyzer system with the HP-8513 reflection/transmission test set. For our purpose, the measurement parameter is set to measure S_{21} , with reference channel input derived from the transmitter assembly and the test channel input derived from the receiver assembly. A simplified version of the receiver assembly given in Figs. 6 and 7 is shown in Fig. 10 in block diagram. A simplified block diagram of the coherent detector (network analyzer) is shown in Fig. 11. The test set acts as a first stage IF converter, downconverting all input RF signals to 20 MHz, which is also the frequency of the reference time base within the HP-8510A. There is a restriction on all signal power at the first harmonic mixers. Too much power will damage the harmonic mixers permanently, and too little will cause the phase-locked loop to lose track. The acceptable power to the mixers should not exceed -10 dBm; damage level is 16 dBm. Reference power to the mixer less than -50 dBm will not be adequate for phase-locking of the internal local oscillator. All the power is referred to the mixer inputs; there is additional 28 dB loss between the reference input and the mixer. Additional attenuation pads may have to be inserted to ensure good measurement accuracy.

The first IFs at 20 MHz enter the HP-8510A for second stage downconversion; this time down to 100 KHz. The second IFs are then sampled and processed to be placed in proper format for feeding to the digital

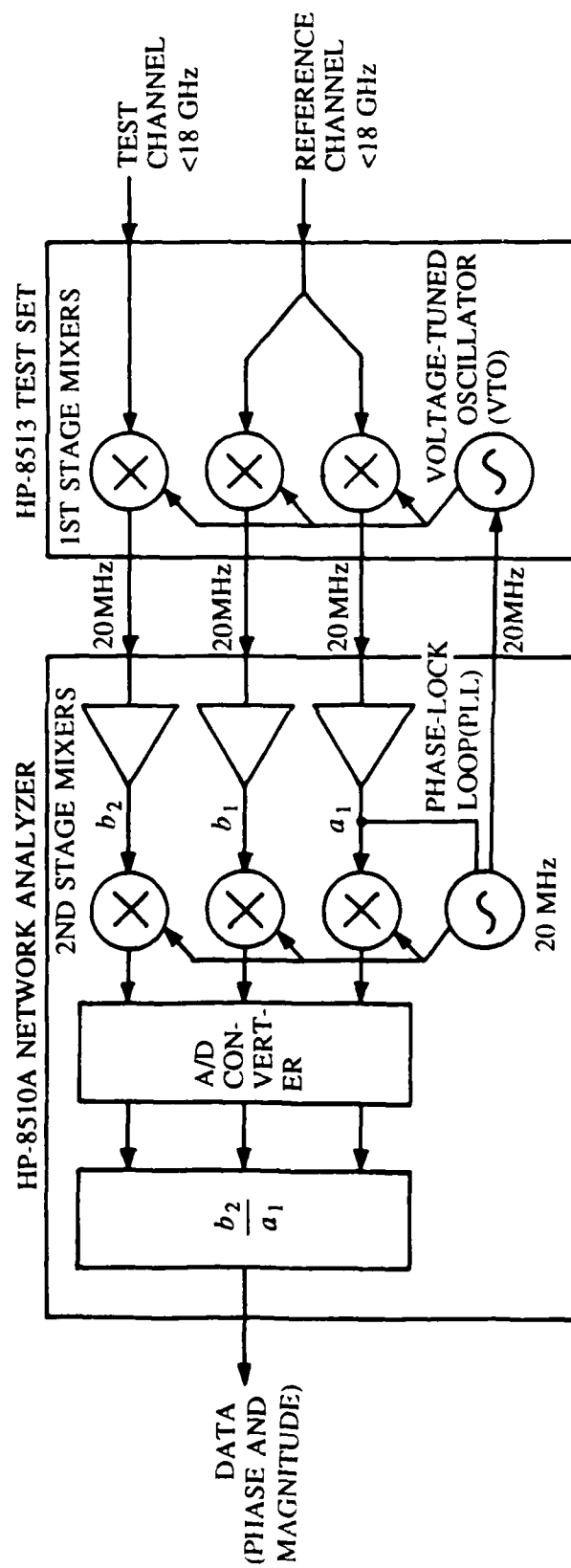


Fig. 11. Simplified schematic of the coherent detector.

phase/amplitude detector of the HP-8510A. The data are read out via the IEEE-488 GPIB, which is also the controlling bus for the HP-8510A.

For our application, the system bus connecting the HP-8510A and the source HP-8340A must be localized in order to control the HP-8340A independently. Due to this localization, some utilities encoded in the operating system of the HP-8510A cannot be used. We'll address this problem in a later section.

VIII. x,y,z, θ , ϕ POSITIONER

The positioner is designed to allow multistatic scattering measurement. To ameliorate the formidable task of having the capability of moving the receiver assembly and the transmitter assembly to arbitrary locations, we opted to provide mobility for the receiver assembly alone. The bulk of the transmitter assembly itself prohibits such mobility. The transmitter assembly is therefore stationary but additional degrees of freedom are achieved by varying the aspect angle of the scattering object. This is accomplished by mounting the test object on a computer controlled elevation over azimuth positioner. Thus the position and direction control is achieved by the combination of moving and steering the receiver assembly, and rotating the test object. A sketch of the x,y,z, θ , ϕ positioner within the anechoic chamber showing its relation to other system components was given earlier (see Fig. 2). Two parallel rails run along the length of the anechoic chamber (x direction), each 48' in length. On these parallel rails moves the transversal rails across the width of the chamber (y direction), 18' in length. A retractable boom (z direction), to the end of which is attached the receiver assembly, rides on the transversal rail, with fully extended length of 18'. There are two additional stepping motors used to

orient the elevational and the azimuthal angles (θ and ϕ) of the receiver assembly such that the antennas can be made to point toward the test object. Thus we have a total of seven stepping motors to be driven independently.

The rails are chromium-plated stainless steel shaft supported intermittently by aluminum rail supporting blocks. The rails are mounted on I-beams made of reinforced fiber glass, chosen to minimize radar cross-section and minimize reflections within the chamber. The parallel rails are attached to the wall of the anechoic chamber, with supporting blocks made of fiber glass. The transversal rails move on the parallel rails by ball-bearing pillow-block riding on stainless shafts. Similarly, the boom is attached to a platform moving on the transversal rails with ball-bearing pillow-blocks underneath. The z-coordinate collapsable boom consists of three sections of fiber glass tubing in different sizes, each section is 6' in length. The three telescoping sections contract within each other and expand under stepper motor control.

To move the positioner, a reference coordinate frame and its origin must be defined with respect to the anechoic chamber. The coordinate is chosen to coincide with the chamber frame, and the origin to be the center of the chamber or the center of rotation of the scattering object O mounted on the elevation over azimuth positioner shown in Fig. 2. Whenever the system is powered up, or before it is being turned off, the x, y, z, θ, ϕ positioner must be relocated to that origin. Therefore there must be a power-up procedure or power-off procedure to initiate the positioner. After that, the movement of the positioner and the steering of the receiving antenna are referred to the origin. Stepper motor pulse counting or mechanical or optical sensors would be incorporated in the positioner to feedback a signal to monitor the position and orientation of the receiver module. For example, by centering

the receiver module at a point representing the center of rotation of the scattering object mounted on the elevation over azimuth positioner an origin for a spherical coordinate system can be defined. The position vector of the receiver module after displacement can then be determined by computing the relative x,y, and z displacements by counting the number of calibrated steps of the x,y,z stepper motors executed to get to that point. The values of x,y and z determined in this fashion enable calculating the radial coordinate $r = (x^2 + y^2 + z^2)^{1/2}$ and the angular spherical coordinates θ' and ϕ' which enable defining the orientation θ and ϕ of the receiver module required to point it towards the object.

IX. SOME DESIGN CONSIDERATIONS

Several aspects of the measurement system design are currently being addressed. The disassociation of the source HP-8340A from the control of the HP-8510A network analyzer is necessitated by the fact that the new system must accommodate measurement at frequencies higher than the capabilities of the HP-8340A/8510A. In normal applications, the HP-8510A, running under the software provided by Hewlett-Packard Co., acts as the controller of the HP-8340A. The HP-8510A is the only instrument to be controlled by the external controller. In the new system, the frequency control of the HP-8340A is relegated from the HP-8510A internal controller to the external controller. Except for the frequency stimulus functions, the remaining utilities offered by the HP-8510A can still be used. The same situation is encountered in the HP and Hughes millimeter-wave network analyzer systems, since these systems also use HP-8510 as the key building block. The operations involving the frequency stimulus must be programmed by the user. More information may be needed from Hewlett-Packard Co. to write such a program.

In designing a network analyzer, efforts are made to maintain the attenuation and phase balance of the test channel and the reference channel. Consider our system as a network analyzer operating in transmission mode with the transmitting section as the reference channel and the receiving section as the test channel. It is ideal that the path length and the attenuation of these two channels are identical. The inequality of path length introduces linear phase difference. Different attenuation causes wrong magnitude ratio reading. Should any nonlinearity exist, e.g., phase instability or excess power in any channel, the measurement errors will be noticeable. We expect programmable power level feature of the HP 8340A synthesized sweeper used will enable precalibration of power levels through the system at different frequencies to alleviate or eliminate any nonlinearity errors.

Every component has a power handling capability such that, within a certain power range, the component is operating in its linear region. Therefore, it is essential to ensure such linear operation for each component; not only to remove nonlinear distortion, but also to use the component at its best performance. To satisfy this consideration, attenuators are inserted at various stages inside the assemblies. The price paid for achieving this is that some power is wasted and the lengths of signal paths becomes unequal. But the gain in performance sanctions such trade-in. The phase difference caused by inequality of signal paths can be eliminated by a calibration procedure which measures the total phase difference of a through connection and stores it as a calibration set, i.e., by measuring and the frequency response of the measurement system itself as was done in the original measurement system. The measurements made afterward are corrected against the calibration data set to compensate the phase

difference. The same calibration procedure can, to a certain degree, correct the residual nonlinearity and power level fluctuations within the system.

Although the design of the system has been for continuous frequency coverage from (2-60) GHz, a few small frequency gaps may exist within the overall bandwidth because of hardware limitations. The missing of these frequencies may not have significant effects on various applications.

The second stage amplification and the frequency downconversion in the receiver assembly are indispensable due to the considerable length of the flexible coaxial cable connecting the receiver assembly to the coherent detector. Flexibility is needed since the receiver assembly must be translatable for multistatic operation. To enable multistatic measurements by positioning the receiver module within the front half of the chamber a 35' coaxial cable is required. A low-loss phase stable coaxial cable must be used. An ideal attractive future alternative is to use a microwave optical fiber link when the bandwidth of such links is made to approach 18 GHz.

The actual data acquisition locations produced by the x, y, z, θ, ϕ positioner are critical in multistatic measurements, especially when frequencies in the millimeter wave range are utilized. In terms of imaging, knowledge of the exact positions where the data are taken is essential to guarantee good image reconstruction. Because of the considerable weight of the transversal rails and the boom, slight bending of the rails is inevitable. We estimate that there will be 0.6" bending in the z direction at most. It would be better if this bending can be compensated, say by retracting or extending the boom. It may become necessary to calibrate the positioner for all locations in the chamber if the position deviations turn out to be appreciably detrimental. Another aspect worth considering is the wobbling of the boom as it changes positions. Adequate time must be allowed

until the boom stabilizes before taking measurement. This would be taken into account in writing data acquisition programs.

Despite the fact that materials chosen are intended to minimize the reflection from the positioner and the receiver assembly, the effect from these reflections can be further minimized by two ways. The first method is to cover reflecting parts of the positioner, including the rails, the boom, and the receiver assembly box with appropriate broadband absorber material. The second method is to measure and store the chamber response for every positioner location on an intended scanning locus, and subtract this response from later measurements. This method may be impractical in that: firstly, the same measurement sequence has to be done twice, one for room clutter, then for test object; secondly, the accuracy, or rather the inaccuracy, of the stepping motors may prevent the positioning repeatability of the two successive measurements. The latter may nullify the very intention for clutter cancellation. A combination of both approaches may offer the best optimal solution.

X. DATA ACQUISITION PROGRAMMING

This section outlines the programming for data acquisition. As we discussed earlier, the x, y, z, θ, ϕ positioner would place itself at the origin of the chamber coordinate, the center of the chamber, before and after data acquisition. This may be done by a start-up program whose sole function is to move the positioner until it finds the chamber origin. This routine should be invoked whenever the system is started and before it is turned off.

We concentrate now on the programming for data acquisition, assuming that the start-up routine has been executed and the positioner is at the origin. Shown in Fig. 10 is the program block diagram of a typical data

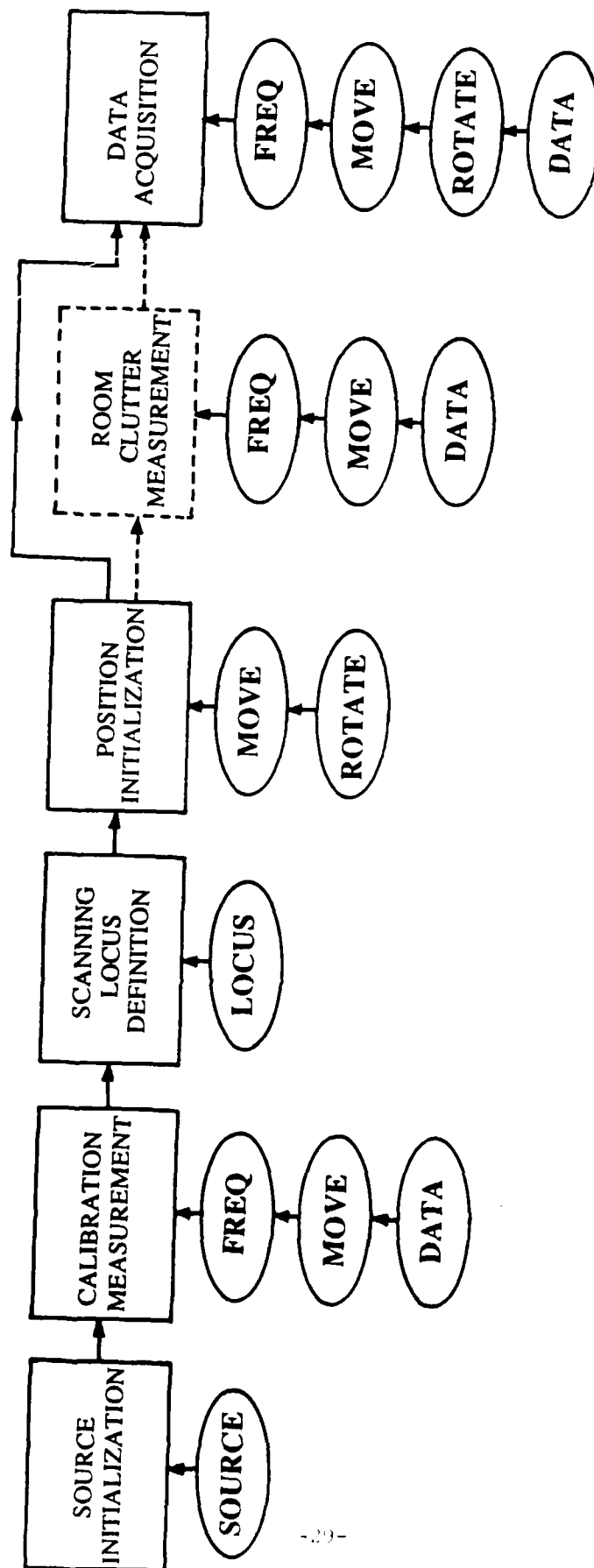


Fig. 12. Conceptual data acquisition programming flow chart.

acquisition session. Also shown below each block are the subroutines needed to perform the function of that block. The principle of modularity in programming is closely observed so that each user can tailor his own program easily using these routines as building blocks. A description of these subroutines is given next:

SOURCE

The source subroutine performs dialogue to accept frequency definitions, e.g., start and stop frequencies, number of frequency samples, power level at each frequency, etc., from the user. From these user-specified parameters, the routine initializes the source and the coherent detector, and generates the switching map for each of the cross-band switches if the frequency range involves cross-band measurement. Also the desired polarization combination is selected.

FREQ

The frequency subroutine uses the parameters generated by SOURCE to perform frequency setting of a single sweep of the specified frequency range. It not only controls the frequency setting and timing, it is also responsible for setting up the proper signal path for cross-band measurement using the switching map generated by SOURCE.

MOVE

The move subroutine controls the relative movement of the x, y, z, θ, ϕ positioner and the orientation θ, ϕ of the receiver module through the control of different stepping motors. The inputs to this routine are the distances in x, y, z directions and the elevation (θ) and azimuthal

(ϕ) angles of the receiver module. All parameters are relative, not related to the absolute coordinates of the chamber. Therefore, these parameters are pre-calculated.

DATA

The data subroutine reads the measurement of one stepped frequency sweep from the network analyzer and delivers the data to the auxiliary storage devices. The data format must be conformed to the other data processing programs.

LOCUS

The locus subroutine calculates the scanning locus of a data acquisition session. It is highly dependent on the specific locus the user intends to synthesize. It is difficult to write a subroutine that gives options for all possible loci, although some regular loci may be implemented. The key parameters to be generated in this routine are the relative changes in positions x, y, z and angles θ, ϕ given a locus definition. The locus definition includes the starting position for scanning, the number of positions, the locus equations, etc.

ROTATE

The rotate subroutine controls the rotation of the test object mounted on the pedestal in order to change its aspect relative to the stationary illuminating antenna and the mobile receiver module. This enables complete multistatic measurement to be carried out.

The aforementioned subroutines are the basic building blocks for any data acquisition program. We describe next the steps in a typical data acquisition session, illustrated in Fig. 12.

The first step is the source initialization. the SOURCE subroutine is the key routine to be called. The functions to be performed at this stage are:

- * Frequency sweep format definition: start and stop frequencies, sweep mode, sampling number.
- * HP-8340A initialization: power level, sweeping time, averaging factor.
- * HP-8510A initialization: measurement parameter S_{21} , system localization, display formats.
- * Switching map calculation for setting the signal path.
- * Selection of polarization states.

After system initialization, a calibration measurement is performed for later data correction. Two subroutines are used in this procedure:

- * Move the receiver assembly to the calibration location by the use of MOVE routine. A good choice of the calibration location is the location closest to the transmitter assembly as if in monostatic arrangement. Also the receiver assembly would be pointing towards the origin of the coordinate (e.g., center of rotation of object on elevation over azimuth positioner).
- * A reference target, a metallic sphere or a metallic cylinder, is centered at the origin of the coordinates.
- * A single frequency sweep of data is taken and stored in the HP-8510A or the computer for later correction. Subroutines used are FREQ and DATA.

After the calibration data measurement, the user enters the locus definition by the use of LOCUS subroutine as follows:

- * Scanning locus definition: starting coordinate, locus equation, and number of scanning positions.
- * Scanning position calculation. Coordinate increments of successive scanning locations are calculated.
- * Scanning angle calculation. Angular increments needed to steer the receiver module toward the object at successive scanning locations are calculated.
- * Define the test object orientation for each scanning location. This step is needed only when more complex loci is desired.

After calculating all the parameters needed, now the positioner is moved to the initial scanning location:

- * Move the positioner to the starting scanning location by the use of MOVE.
- * Rotate the test object to the initial orientation by the use of ROTATE.

The system now is ready to collect the data. The data acquisition consists of the following steps:

- * Collect one frequency sweep of data by the use of FREQ.
- * Get the data from the system and store them by the use of DATA.
- * Move to the next scanning location and orientation of the receiver module by the use of MOVE.
- * Change the object orientation as desired by the use of ROTATE.
- * Repeat the same procedure.

After the end of data acquisition, the positioner and the object are reset to their initial location and orientations.

Note that in Fig. 12, there is an intermediate step of clutter measurement. This step is essentially the same as data acquisition, except that now there is no object placed on the pedestal. The measured quantity is the aspect dependent room clutter. After clutter measurement, the positioner is moved to the initial scanning location.

XI. CONCLUSIONS

The new upgraded system possessing wavelength, polarization, and position diversity measurement capability in the (2-60) GHz range is described. The equipment and components are delineated. Many aspects of the design problems and the viable solutions to these problems are presented. The programming considerations are addressed, with a typical data acquisition session as an example. Most of the components are in hand and in a state of partial assembly. The construction and assembly of the x, y, z, θ, ϕ positioner is about 60% completed. The implementation of the system is a challenging task. However once fully operational, the system will be a unique tool in the study of multistatic scattering, polarization effects, and radar imaging modalities in the (2-60) GHz range. The system will also be invaluable in the generation of high fidelity target representations and signatures in the study and development of automated recognition schemes based on models of neural networks.

The components of the system have been chosen with multifunctionality in mind. For example the components of the frequency agile phase-locked reference oscillator in Fig. 4 can be reconfigured as shown in Fig. 13 to furnish a high-speed synthesized source for illuminating a target for rapid data acquisition that is one to two order of magnitude faster than with the hp 8340A based system.

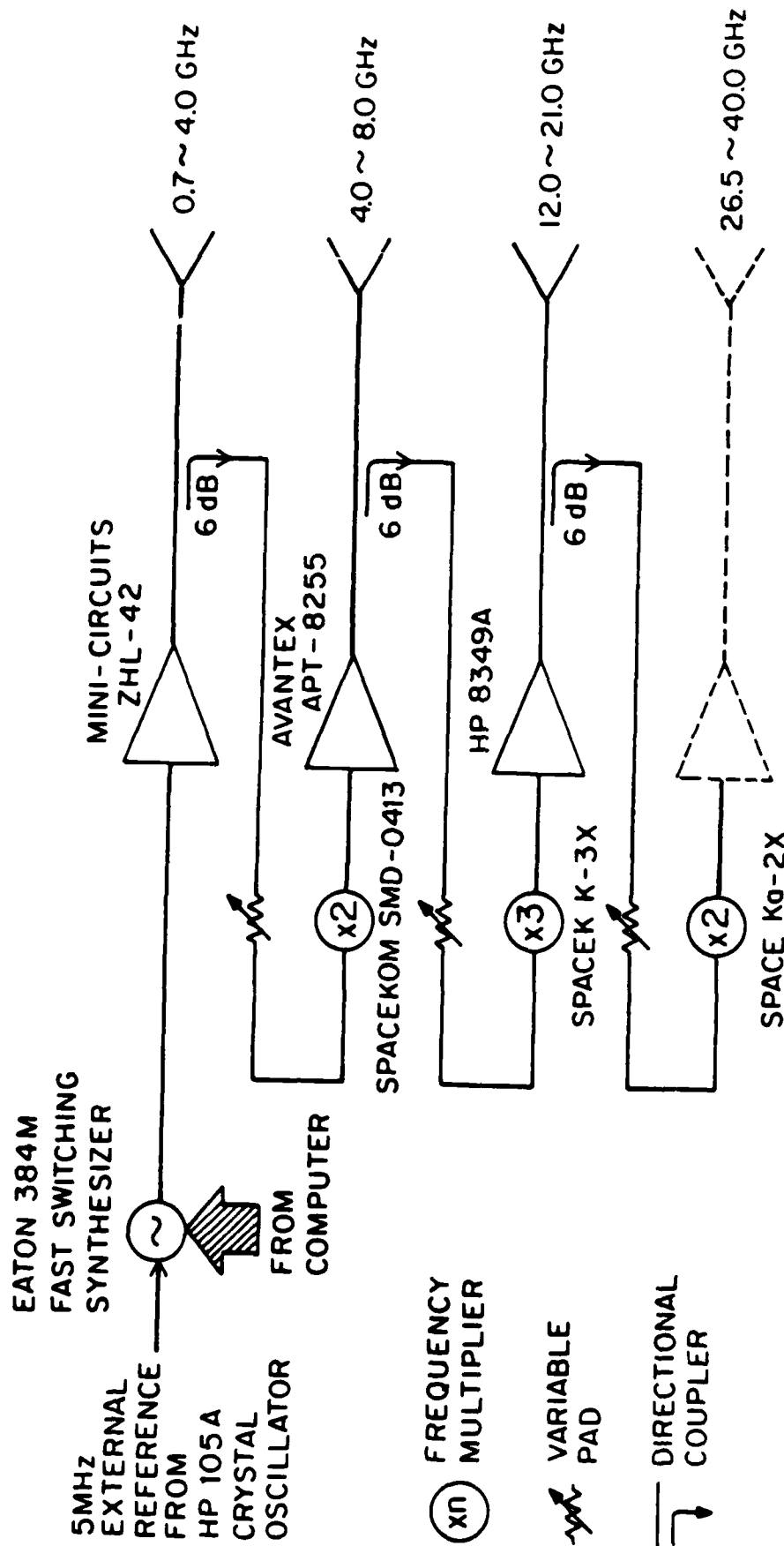


Fig. 13. Fast switching (.7-40) GHz synthesized transmitter module.

OPTICAL ANALOGS OF TWO-DIMENSIONAL NEURAL
NETWORKS AND THEIR APPLICATION IN RECOGNITION OF RADAR TARGETS

N.H. Farhat, S. Miyahara and K.S. Lee
University of Pennsylvania
The Electro-Optics and Microwave-Optics Laboratory
200 S. 33rd Street
Philadelphia, PA 19104-6390

ABSTRACT

Optical analogs of 2-D distribution of idealized neurons (2-D neural net) based on partitioning of the resulting 4-D connectivity matrix are discussed. These are desirable because of compatibility with 2-D feature spaces and ability to realize denser networks. An example of their use with sinogram classifiers derived from realistic radar data of scale models of three aerospace objects taken as learning set is given. Super-resolved recognition from partial information that can be as low as 20% of the sinogram data is demonstrated together with a capacity for error correction and generalization.

INTRODUCTION

Neural net models and their analogs furnish a new approach to signal processing that is collective, robust, and fault tolerant. Optical implementations of neural nets^{1,2} are attractive because of the inherent parallelism and massive interconnection capabilities provided by optics and because of emergent optical technologies that promise high resolution and high speed programmable spatial light modulators (SLMs) and arrays of optical bistability devices (optical decision making elements) that can facilitate the implementation and study of large networks. Optical implementation of a one-dimensional network of 32 neurons exhibiting robust content-addressability and associative recall has already been demonstrated to illustrate the above advantages.³ Extension to two-dimensional arrangements are of interest because these are suitable for processing of 2-D image data or image classifiers directly and offer a way for optical implementation of large networks.⁴

In this paper we will discuss content addressable memory (CAM) architectures based on partitioning of the four dimensional T_{ijkl} memory or interconnection matrix encountered in the storage of 2-D entities. A specific architecture and implementation based on the use of partitioned unipolar binary (u.b.) memory matrix and the use of adaptive thresholding in the feedback loop are described. The use of u.b. memory masks greatly simplifies optical implementations and facilitates the realization of larger networks $\sim (10^3 - 10^4)$ neurons. Numerical simulations showing the use of such 2-D networks in the recognition of dilute point-like objects that arise in radar and other similar remote sensing imaging applications are described. Dilute objects pose a problem for CAM storage because of the small

Hamming distance between them. Here we show that coding in the form of a *sinogram classifier* of the dilute object can remove this limitation permitting recognition from partial versions of the stored entities. The advantage of this capability in super-resolved recognition of radar targets is discussed in the context of a new type of radar diversity imaging, studied extensively in our laboratory, that is capable of providing sinogram information compatible with 2-D CAM storage and interrogation. Super-resolved automated recognition or scale models of three aero-space objects from partial information as low as 20% of a learned entity is shown employing hetero-associative storage where the outcome is a word label describing the recognized object. Capacity for error correction and generalization were also observed.

TWO-DIMENSIONAL NEURAL NETS

Storage and readout of 2-D entities in a content addressable or associative memory is described next. Given a set of M 2-D bipolar binary patterns or entities $v_{ij}^{(m)}$ $m=1,2,\dots,M$ each of $N \times N$ elements represented by a matrix of rank N , these can be stored in a manner that is a direct extension of the 1-D case as follows: For each element of a matrix a new $N \times N$ matrix is formed by multiplying the value of the element by all elements of the matrix including itself taking the self product as zero. The outcome is a new set of N^2 binary bipolar matrices each of rank N . A formal description of this operation is,

$$T_{ijkl}^{(m)} = \begin{cases} v_{ij}^{(m)} v_{kl}^{(m)} & i=k, j=l \\ 0 & \text{otherwise} \end{cases} \quad (1)$$

which is a four dimensional matrix. An overall or composite synaptic or connectivity memory matrix is formed then by adding all 4-D matrices $T_{ijkl}^{(m)}$ i.e.,

$$T_{ijkl} = \sum_m T_{ijkl}^{(m)} \quad (2)$$

This symmetric 4-D matrix has elements that vary in value between $-M$ to M also in steps of two as for the 1-D neural net case and which assume values of $+1$ and -1 (and zeros for the self product elements) when the matrix is clipped or binarized as is usually preferable for optical implementations. Two dimensional unipolar binary entities $b_{ij}^{(m)}$ are frequently of practical importance. These can be transformed in the usual way into bipolar binary matrices through $v_{ij}^{(m)} = (2b_{ij}^{(m)} - 1)$ which are then used to form the 4-D connectivity matrix or memory as described. Also, as in the 1-D neural net case, the prompting entity can be unipolar binary $b_{ij}^{(m)}$, which would simplify further optical

implementations in incoherent light.

Architectures for optical implementation of 2-D neural nets must contend with the task of realizing a 4-D memory matrix. Here a scheme is presented that is based on the partitioning of the 4-D memory matrix into an array of 2-D matrices of rank N.

Nearest neighbor search of the memory matrix for a given entity $b_{ij}^{(mo)}$ is done by forming the estimate,

$$\hat{b}_{ij}^{(mo)} = \sum_{k,l}^N T_{ijkl} b_{kl}^{(mo)} \quad \dots i,j,k,l = 1,2,\dots,N \quad (3)$$

followed by thresholding to obtain a new u.b. matrix which is used to replace $b_{kl}^{(mo)}$ in eq. (3) and the procedure is repeated until the resulting matrix converges to the stored entity closest to the initiating matrix $b_{ij}^{(mo)}$. The operation in eq. (3) can be interpreted as first partitioning of the 4-D T_{ijkl} matrix into an array of 2-D submatrices of rank N: $T_{11kl}, T_{12kl}, \dots, T_{1Nkl}; T_{21kl}, T_{22kl}, \dots, T_{2Nkl}; \dots, T_{N1kl}, T_{N2kl}, \dots, T_{NNkl}$ as depicted schematically in Fig. 1(a) where the partition submatrices are arranged in a 2-D array. This first step is followed by multiplication of $b_{kl}^{(mo)}$ by each of the partition submatrices, on an element by element basis, and summing the products for each submatrix to obtain the first estimate $\hat{b}_{ij}^{(mo)}$. The tensor multiplications and summation operations called for in eq. (3) are carried out in Fig. 1(a) by placing a spatially integrating photodetector (PD) behind each submatrix of the partitioned

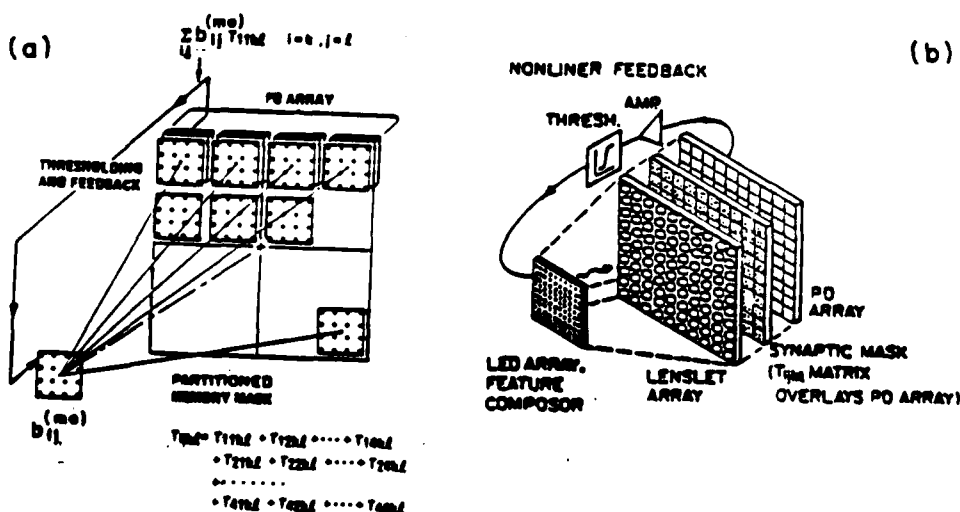


Fig. 1. Optical analog of 2-D neural net. (a) Architecture based on partitioning of connectivity matrix, (b) Opto-electronic embodiment.

memory mask which is assumed for the time being to be realized by pixel transmittance modulation in an ideal transparency capable of assuming negative transmittance values. The input entity $b_{ij}^{(mo)}$ is assumed to be displayed on a suitable LED array. The LED display of $b_{ij}^{(mo)}$ is multiplied by the ideal transmittance of each of the partition submatrices by imaging the display on each of these with exact registration of pixels by means of a lenslet array as depicted in Fig. 1(b). The output of each PD, proportional to one of the components of eq. 3, is thresholded, amplified, and fed back to drive an associated LED. The (i,j) -th LED is paired with the (i,j) -th PD. This completes the interconnection of the 2-D array of $N \times N$ neurons in the above architecture where each neuron communicates its state to all other neurons through a prescribed four dimensional synaptic or memory matrix in which information about M 2-D binary matrices of rank N (entities) have been stored distributively. The number of 2-D entities that can be stored in this fashion is $M \approx N^2/8 \ln N$, which follows directly from the storage capacity formula for the 1-D neural net case by replacing N by N^2 .

The added complexity associated with having to realize a bipolar transmittance in the partitioned T_{ijkl} memory mask of Fig. 1 can be avoided by using unipolar transmittance. This can lead however to some degradation in performance. A systematic numerical simulation study⁵ of a neural net CAM in which statistical evaluation of the performance of the CAM for various types of memory masks (multivalued, clipped ternary, clipped u.b.) and thresholding schemes (zero threshold, adaptive threshold where energy of input vector is used as threshold, adaptive thresholding and relaxation) was carried out. The results indicate that a u.b. memory mask can be used with virtually no sacrifice in CAM performance when the adaptive thresholding and relaxation scheme is applied. The scheme assumes an adaptive threshold is used that is proportional to the energy (total light intensity) of the input entity displayed by the LED array at any time. In the scheme of Fig. 1(b) this can be realized by projecting an image of the input pattern directly onto an additional PD element. The PD output being proportional to the total intensity of the input display is used as a variable or adaptive threshold in a comparator against which the outputs of the PD elements positioned behind the partitioned components of the T_{ijkl} memory mask are compared. The outcomes, now bipolar, are attenuated and each is fed into a limiting amplifier with delayed feedback (relaxation). Each limiter/amplifier output is used to drive the LED that each photodetector is paired with. It was found⁵ that this scheme yields performance equivalent to that of an ideal CAM with multivalued connectivity matrix and zero thresholding. Note that although the initializing 2-D entity $b_{ij}^{(mo)}$ is unipolar binary, the entities fed back after adaptive thresholding and limited amplification to drive the LED array would initially be analog resulting in multivalued iterates and intensity displays. However, after few iterations the

outputs become binary assuming the extreme values of the limiter. The ability to use u.b. memory matrices in the fashion described means that simple black and white photographic transparencies or binary SLMs can be used respectively as stationary or programmable synaptic connectivity masks as suggested by Fig. 1.

SINOGRAM CLASSIFIERS AND HETEROASSOCIATIVE STORAGE

Sinograms are object representations encountered in tomography^{6,7}. They are also useful as object classifiers specially when the objects are point-like and dilute⁸. Given a set of 2-D dilute objects the Hamming distances between their sinogram classifiers will be greater than the Hamming distances between the objects themselves, with both sets digitized to the same number of pixels, making it easier for an associative memory to distinguish between the sinograms⁸. Sinogram classifiers have additional advantages that enable scale, rotation, and shift invariant recognition of radar target which can not be detailed here because of limited space. A sinogram is a cartesian plot of the polar projections of object detail. For example referring to Fig. 2(a) which represents a dilute object consisting of 16 points on a 32x32 pixel grid, the distance that the projection of each point makes on the y axis as measured from the origin when the object is rotated about the origin traces a sinusoidal pattern when plotted against rotation angle as shown in Fig. 2(b). Figure 2(c) is a

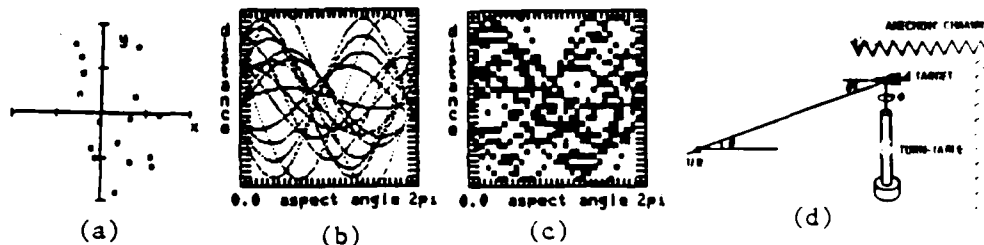


Fig. 2. Sinogram generation. (a) Sparse object, (b) Sinogram, (c) Digitized sinogram, (d) Experimental sinogram generation in radar by range-profile measurement.

digitized version of the sinogram of Fig. 2(b) plotted on a 32x32 pixel grid. The sinogram of a radar target is produced by measuring the differential range or range-profile of the target employing the arrangement of Fig. 2(d). The system basically measures, with high resolution, the differential distance (differential range or range-profile) from the rotation center of the projections of the scattering centers of the object (here scale models of aerospace targets) on the line-of-sight of the radar system. Cartesian plots of the differential distance or range-profile versus azimuthal angle of rotation ϕ results in a sinogram classifier or feature space of the target which characterizes it at any fixed elevation angle θ . The top row of Fig. 3 shows three digitized sinogram classifiers of scale models of three aerospace targets plotted on a 32x32 pixel

grid. These are treated as a learning set and stored hetero-associatively rather than autoassociatively by replacing $v_{kl}^{(m)}$ in eq. (1) by $r_{kl}^{(m)}$ $k, l=1, 2, \dots, 32$; $m=1, 2, 3$ where $r_{kl}^{(m)}$ represents abbreviated word labels shown in the bottom row of Fig. 3 with which the three test objects are to be associated.

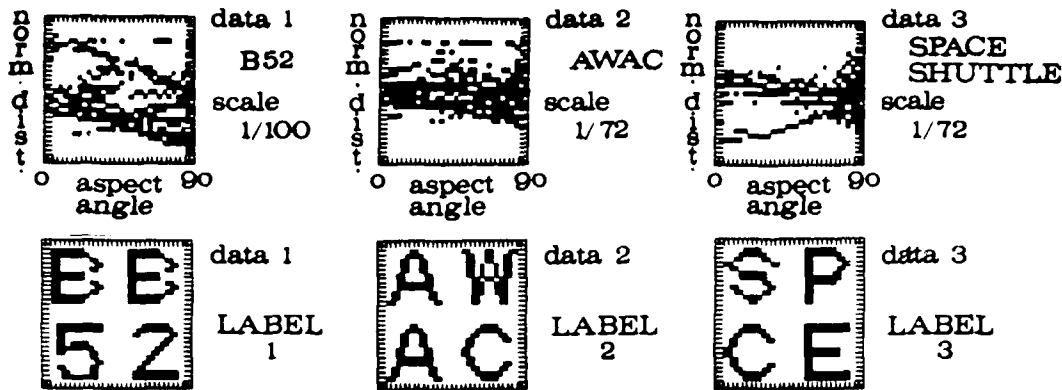


Fig. 3. Hetero-associative storage. Digitized sinograms (top) and associated word labels (bottom).

RESULTS

Representative results of numerical simulation of exercising the heteroassociative memory matrix with complete and partial versions of one of the stored entities in which the fraction η of correct bits or pixels in the partial versions ranged between 1 and .1 are presented in Fig. 4. Reliable recognition was found to occur after one iteration for all entities stored down to $\eta = .2$. For $\eta = .1$ or less successful recall of correct labels was found to depend on the angular location of the partial data the memory is presented with as illustrated in the two

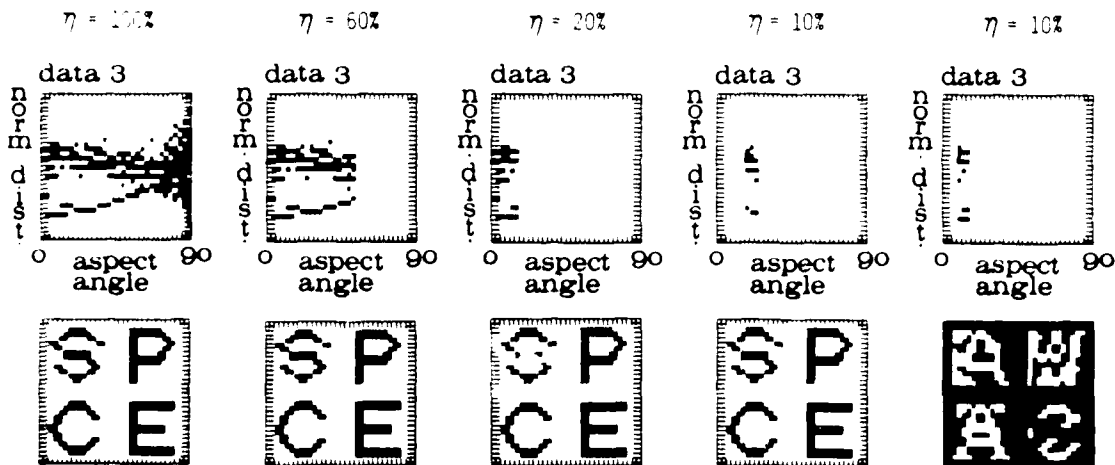


Fig. 4. Example of recognition from partial information. Complete and partial sinograms of data set 3 used as input (top), and final memory state-recognized label (bottom).

right-most examples in Fig. 4. Here the memory could not label the partial input correctly but converged instead onto a label that it did not learn before. This appears to be a generalization (mixture) of the three entities stored earlier. This is quite analogous to the generalization capability of the brain. Note the generalization is contrast reversed as we know that stable states of a memory with symmetric connectivity matrix are not only the entities stored but also their compliments.

CONCLUSIONS

Architectures for optical implementation of 2-D neural nets based on partitioning of the 4-D connectivity matrix are shown to be suitable for use with 2-D object classifiers or feature spaces. An example of their utility in super-resolved recognition (labeling) of radar targets characterized by sinogram classifiers is presented. The results show that neural net models and their opto-electronic analogs furnish a new viable approach to signal processing and automated recognition that is both robust and fault tolerant.

ACKNOWLEDGEMENT

The work described was carried out under a grant from DARPA/NRL, and partial support from AFOSR, ARO, and RCA (GE) Corporation.

REFERENCES

1. D. Psaltis and N. Farhat, Opt. Lett., 10, 98, (1985).
2. A.D. Fisher, et. al., SPIE, 625, 28 (1986).
3. N. Farhat, D. Psaltis, A. Prata and E. Paek, App. Optics, 24, 1469, (1985).
4. N. Farhat and D. Psaltis, Digest OSA Annual Meeting, Wash., D.C., p. 58, (1985).
5. K.S. Lee and N. Farhat, Digest OSA Annual Meeting, Wash., D.C., p. 48, (1985).
6. G. Herman, Image Reconstruction From Projections (Academic Press, N.Y., 1980), p. 11.
7. G.R. Gindi and A.F. Gmitro, Opt. Eng., 23, p. 499, (1984).
8. N. Farhat and S. Miyahara, Technical Digest, Spring 86 OSA Topical Meeting on Signal Recovery and Synthesis II, p. 120, (1986).

A NEW ITERATIVE ALGORITHM FOR EXTRAPOLATION OF DATA AVAILABLE IN MULTIPLE RESTRICTED REGIONS WITH APPLICATION TO RADAR IMAGING

Hsueh-Jyh Li, Nabil H. Farhat and Yuhsyen Shen

The Moore School of Electrical Engineering
University of Pennsylvania
Philadelphia, PA. 19104

I. INTRODUCTION

It is well known that the resolution of microwave diversity imaging systems [1] depends on the spectral and angular (aspect related) windows utilized and on the use of polarization diversity to enhance the amount of information about a scattering object collected by a highly thinned recording aperture. To obtain the range information of the target, one can use a pulsed signal analyzed in the time domain and map thus the range profile of the target as function of aspect angle or use a broad-band CW signal analyzed in frequency domain to yield its frequency response. The range resolution is inversely proportional to the bandwidth coverage of the measurement system. The latter approach is ordinarily easier to implement. In practical situations, however, due to limitation of the measurement system or restriction of bandwidth allocation, the observed data can lie in multiple restricted spectral regions which we call pass bands. Several methods of extrapolating the measured data beyond the observed regions have been proposed and tested [2,3,4] in an attempt to achieve the full resolution of the unrestricted spectral range, when a prior knowledge of the maximum dimension of the object exists, and an iterative procedure is applied.

To increase the resolution obtained from spectral data of such limited extent, techniques of nonlinear power spectrum estimation have been used with notable success [5]. These include autoregression (AR), linear prediction (LP), and maximum entropy method (MEM). For a stationary Gaussian process, the above methods can be shown to be equivalent [5].

Although the spectra estimated by MEM or AR can be very sharp and well resolved, this may not be to advantage in a microwave imaging system. If the data are not sampled densely enough in the spectral domain as the sharp well resolved component may be missed, and the results may not reflect faithfully the actual spectral amplitudes. Besides, image reconstruction from microwave diversity imaging systems involves coherent superposition of the data in the spectra, or range profiles, of the scatterer (obtained at different looks or aspect angle), where these are estimated from partial data available in segmented bands [1]. If the estimated amplitudes of the range profiles obtained by MEM or AR depart from the desired values because of undersampling, image degradation will result. Therefore, to overcome the dense sampling requirement, it may be preferable to extrapolate the data available in the various pass bands into the vacant bands before the spectra or range profile are formed, and image reconstruction is undertaken.

If one wishes to predict the next value in a sequence on the basis of previous samples, one can use the linear prediction model which consists of finding the parameters that minimize the summation of prediction error energies which will be defined in the later section. To extrapolate the data beyond the observed region, an intuitive way is to predict the exterior data by using the same parameters obtained by the linear prediction model. The most popular approach for linear prediction parameters estimation with N data samples is the Burg algorithm [5,6]. For a given number of data samples in a given observation interval, in order to separate the discrete spectra (in this paper, spectrum is defined as the Fourier transform of the observed data), the required model order in the linear prediction method increases as the separation of spectra decreases, i.e., it is easier to model the data sequence for spectra with larger separation than those with closer separation, which translates into well separated scattering centers. In addition, for a given model order and given number of sampling points, it is easier to distinguish the two close spectra components (scattering centers) by a data set with longer observation interval than that by a data set with shorter observation interval. It was also suggested that the model order should not exceed half of the number of data points

for short data segment because otherwise the linear prediction spectral estimate will exhibit spurious peaks [5]. From the above observations, one can conclude that it would be more difficult to resolve two closer point targets (Fourier transform of the observed data in frequency domain) with short data band. If all the observed data within multiple restricted regions can be fully utilized, better resolution can be expected.

It is known that the linear prediction method is especially suited for those cases when the spectra are in discrete type. Under high frequency condition, the scattered fields of a complex target can be ascribed to a few discrete scattering centers and edge diffractions. It will be shown that under the high frequency approximation the locations of the scattering centers and their scattering strengths are independent of the operating frequency for a given transmitter/receiver pair. These phenomena provide the motivation to investigate a new method for extrapolation of scattered field data available in multiple restricted frequency bands.

In this paper, a new iterative algorithm which uses the Burg algorithm to find the linear prediction parameters and an iterative method to modify the prediction parameters is proposed and tested with both simulated and realistic measured data generated in our anechoic chamber experimental microwave imaging and measurement facilities. With this algorithm, one can obtain acceptable extrapolation beyond the observed region if the spectra are in discrete forms and the separation of the spectra are not too close. Both simulation and experimental results are presented to demonstrate as an example the effectiveness of the method in microwave diversity radar imaging.

II. THE NEW ITERATIVE ALGORITHM

The most popular approach to linear prediction parameter estimation with N data samples $\{x_1, \dots, x_N\}$ was introduced by Burg [6]. The linear prediction parameters are obtained by minimizing the sum of the forward and backward prediction error energies ε_p ,

$$\varepsilon_p = \sum_{n=p}^{N-1} |e_{pn}|^2 + \sum_{n=p}^{N-1} |b_{pn}|^2, \quad (1)$$

subject to the constraint that the prediction parameters satisfy a recursion relationship [5], where e_{pn} is the forward prediction error with model order p and is given by

$$e_{pn} = \sum_{k=0}^p a_{pk} x_{n-k}, \quad (2)$$

and b_{pn} is the backward prediction error with model order p and is given by

$$b_{pn} = \sum_{k=0}^p a_{pk}^* x_{n-p+k}. \quad (3)$$

a_{pk} are called linear prediction parameters, and asterisk denotes the complex conjugate operation.

If one is going to extrapolate from the available data beyond the observed region, a straight forward way is to use the estimated prediction parameters a_{pk} and the measured data by the following equations,

$$\hat{x}_{N+j} = \sum_{k=1}^p a_{pk} x_{N+j-k} \quad j > 0; \quad (4)$$

$$\hat{x}_{-j} = \sum_{k=1}^p a_{pk}^* x_{-j+k} \quad j > 0, \quad (5)$$

where the $\hat{}$ denotes the estimated value.

If the data available are confined to multiple separate spectral regions or pass-bands of equal width as illustrated in Fig. 1, and one tries to extrapolate from the observed data to the vacant bands, an intuitive method is to divide the inner vacant band into two parts of equal width and to extrapolate into the left part by using the prediction parameters obtained from the data set of region I and extrapolate into the right part by using the model parameters obtained from the data set of region II.

If the data sequence can be correctly expressed by the prediction parameters, then the extrapolation error, which is defined as the absolute value of the complex difference between the theoretical values and extrapolated values, would be very small. However, if the prediction parameters cannot model the sequence correctly, the error of extrapolation may accumulate.

We have found that the longer the available data string, the larger the model order, the linear prediction model which characterizes the data sequence would be more accurate especially in the presence of noise. However, the model order should not exceed half of the number of the samples because the estimated spectrum will produce spurious peaks [5].

In order to utilize the information available in different regions, a new iterative algorithm using the Burg algorithm to estimate the prediction parameters and a new iterative method is proposed. The procedure illustrated in Fig. 2 is as follows:

1. Divide the inner vacant band into two parts of equal width. Extrapolate into the left part by using the prediction parameters obtained from the data set of region I and extrapolate into the right part by using the prediction parameters obtained from the data set of region II. If the bands are not equal in width, unequal division of the vacant intervening bands may be appropriate.
2. With the "vacant band"s' data together with the observed data, use the Burg algorithm to find a new set of prediction parameters.
3. Using this set of prediction parameters and the data of region I, extrapolate into the left part of vacant bands, and using the same set of prediction parameters and the data in region II, extrapolate into the right part of the vacant bands.
4. Using this set of parameters together with the extrapolated data, estimate the data in the observation region I and II. Calculate the error energy between the measured data and the estimated data in the observation regions. The error energy is denoted by E_1 and is given by:

$$E_1 = \sum_i |x_i - \hat{x}_i|^2 + |x_i - \hat{x}'_i|^2 = \sum_i |e_i|^2 + |b_i|^2, \quad (6)$$

where x_i are the measured data, \hat{x}_i are the forward estimation of x_i , \hat{x}'_i are the backward estimation of x_i , e_i is the forward prediction error, and b_i is the backward prediction error.

5. With the measured data together with the estimated "vacant band"s' data, use the Burg algorithm to find a new set of prediction parameters. From the measured data and this new set of prediction parameters, extrapolate the "vacant band"s' data as described in step 3.
6. Use the same procedure of step 4 to calculate the new error energy of the pass-bands, call it E_2 .
7. Compare E_1 with E_2 , if E_2 is smaller than E_1 , replace the error energy E_1 by E_2 , repeat step 5.
8. If E_2 is greater than E_1 , stop the iteration, and take the extrapolated data of the previous loop as the final result.

In step 1, if the width of a single band (band I and/or band II) is not large enough, the extrapolation errors produced by the prediction parameters obtained from single pass-band data may be very large, in that case, we can set the data in the vacant bands to zero.

The above iterative method can be easily applied to the case where only one single data band is available to extrapolate outside it. The procedures are almost the same except that only one data band sequence is used to extrapolate to the exterior bands and to calculate the extrapolation errors.

III. SCATTERING PROPERTIES OF A METALLIC OBJECT

In this section we shall show that under the high frequency approximation the scattered fields of a metallic object can be expressed as superposition of scattered fields of discrete scattering centers. These phenomena allow us to apply the proposed extrapolation algorithm to radar imaging.

For a metallic object large compared with wavelength, the scattering mechanism can be divided into the following components [7]:

1. Specular scattering points
2. Scattering from surface discontinuity: edges, corners, tips etc.
3. Scattering from surface derivative discontinuities
4. Creeping waves
5. Traveling waves
6. Scattering from concave regions
7. Multiple scattering points

For most situations, the major contributions to the scattered waves are ascribed to the specular scattering points and edge diffractions.

Consider a metallic object seated on a rotated pedestal and illuminated by a plane wave as shown in Fig. 3. The distance between the rotation center O and the transmitter and receiver are R_t and R_r respectively, and the unit vectors in the direction of transmitter and receiver are \hat{l}_t and \hat{l}_r respectively. Under the physical optics and Born approximations, the scattered fields at the receiver under far field condition can be expressed as [1]

$$\vec{E}_s(k) = \frac{jk}{2\pi R_r} e^{-jkR_r} \int_{S_{ill}} 2\hat{n}(\vec{r}') \times \vec{H}_0(k) e^{jk[(\hat{l}_r - \hat{l}_t) \cdot \vec{r}']} dS', \quad (7)$$

where k is the wave number, S_{ill} the illuminated region, $\hat{n}(\vec{r}')$ the unit normal vector at the surface point \vec{r}' , and $\vec{H}_0(k)$ the incident magnetic field at the rotation center.

As k approaches infinity, the asymptotic expression of the above equation can be obtained by applying the stationary phase method [8] to eq. (7). The result is,

$$\vec{E}_s(k) = \frac{jk}{2\pi R_r} e^{-jkR_r} \sum_j \frac{j2\pi}{k\sqrt{S_j}} 2\hat{n}(\vec{r}'_j) \times \vec{H}(k) e^{jk[(\hat{l}_r - \hat{l}_t) \cdot \vec{r}'_j]} \quad (8)$$

where \vec{r}'_j are the vectors such that

$$\left. \frac{d[(\hat{l}_r - \hat{l}_t) \cdot \vec{r}']}{da'} \right|_{\vec{r}' = \vec{r}'_j} = 0, \quad (9)$$

and

$$S_j = \frac{d^2 [(\hat{l}_r - \hat{l}_t) \cdot \vec{r}']}{da'^2} \Big|_{\vec{r}' = \vec{r}'_j} \quad (10)$$

where $\frac{d}{da'}$ is the derivative with respect to the surface curvature. The points \vec{r}'_j corresponding to the solutions of eq. (9) are called stationary points or equi-phase points or the scattering centers, the term $\hat{n}(\vec{r}'_j) \times \vec{H}_0(k) / \sqrt{S_j} = \vec{\alpha}_j$ is called the scattering strength for the particular scattering center at \vec{r}'_j . It is seen that the locations of the scattering centers depend on the directions of \hat{l}_r , \hat{l}_t as well as the shape of the metallic surface. The scattering strength depends on the local properties of the scattering centers. The above analysis illustrates that the object function we would be dealing with in high frequency radar imaging are of discrete form consisting of point scattering centers.

If the received scattered fields have been calibrated with a reference target [1], the corrected fields $\vec{E}'_s(k)$ can be expressed as

$$\vec{E}'_s(k) = \sum_j \vec{\alpha}_j e^{jk[(\hat{l}_r - \hat{l}_t) \cdot \vec{r}'_j]} \quad (11)$$

The Fourier transform of eq. (11) will give the range profile and scattering strength of the scattering centers.

IV. RESULTS

In this section, the performance of the proposed new algorithm using both simulated and realistic data will be evaluated. First, assume for simplicity an object consisting of n point scatterers located at $(r_o + y_j)$ is illuminated by a plane wave, where r_o is the distance between the transmitter/receiver and a reference point of the object and y_j is the differential range of the j th scatterer (range relative to r_o). Under far field condition and ignoring multiple scattering, and considering for simplicity a scalarized version of eq. (11), the corrected scalar field can be expressed as

$$E'_s(k) = \sum_j a_j e^{j2k y_j} \quad (12)$$

In the following simulation, the theoretical values of $E'_s(k)$ are calculated in 200 equally spaced frequency steps covering the frequency range $f_1 = 6$ GHz to $f_{200} = 16$ GHz, with an assumed signal to noise ratio set to 40 dB. These values anticipate the realistic experimental data utilized in testing the algorithm.

Assume the available (computed) data are in the following pass-band (f_{30}, f_{80}) and (f_{120}, f_{170}) . We want to extrapolate the data to the vacant bands (f_1, f_{29}) , (f_{81}, f_{129}) , and (f_{171}, f_{200}) . The range resolution obtained by the DFT method using the whole bandwidth (f_1, f_{200}) is about 1.5 cm. The resolution using a single frequency band is about 5.5cm. The resolution using both frequency bands is about 2.0 cm, however, very high side-lobe level will be produced. We consider a scatterer with seven point scatterers, the location and scattering strength for each point scatterer are $(r_1 = -30$ cm, $a_1 = 0.5)$, $(r_2 = -20$ cm, $a_2 = 0.5)$, $(r_3 = -10$ cm, $a_3 = 0.5)$, $(r_4 = -2$ cm, $a_4 = 1)$, $(r_5 = 10$ cm, $a_5 = 0.25)$, $(r_6 = 20$ cm, $a_6 = 0.25)$, $(r_7 = -30$ cm, $a_7 = 0.25)$. The values of the field at each sampled frequency f_j are calculated using eq. (12).

Define the extrapolation error at frequency f_j as

$$\varepsilon(f_j) = |E'_s(f_j) - \hat{E}'_s(f_j)|, \quad (13)$$

where $\hat{E}'_s(f_j)$ is the extrapolated value at each f_j . The extrapolation errors for different algorithms are compared and shown in Fig. 4(a). The bold solid curve is the amplitude of the theoretically computed fields $E'_s(f_j)$, the thin solid curves are the extrapolation error after 100 iterations using the algorithm proposed in [3], the dashed curves are obtained by using the Burg algorithm to find the prediction parameters from the respective pass-band, and using this set of parameters together with data in each pass-band to extrapolate to the outside regions (bands III and IV). The dotted line curves are obtained using this new algorithm with one iteration and with model order 25. The algorithm proposed in [3] involves basically application of the Gerchberg algorithm to data in the multiple restricted regions. However, no numerical or experimental results are given in that paper. It is clear from the results obtained

here that the algorithm in [3] seems not to be effective in the case considered as the errors can exceed the amplitude of the theoretical fields. Extrapolation from single pass-band are not good in this example, because the model order is not sufficient to model the data series in the presence of noise. The proposed new method after one iteration is seen to produce small error.

The Fourier transform (FT) of the all-band data (i.e, data in region I to IV), pass-band data only, pass-band plus extrapolated data using the algorithm in [3] and pass-band plus extrapolated data with the new proposed method are shown in Fig. 4(b) to 4(e) respectively. Note that the FT of spectral data yields range profile of the scattering object. It is clear that FT using pass-band data only (Fig. 4(c)) has very high side-lobe structure, the FT of the extrapolated data using the algorithm in [3] (Fig. 4(e)) is totally different from the original of Fig. 4(b). The result obtained by Fourier transforming the data generated by the proposed algorithm is shown in Fig. 4(d) which exhibits excellent agreement with the all-band result of Fig. 4(b). The magnitudes of the peaks in Figs. 4(b) and 4(d) depart from the original assigned values because of zero padding used in the fast Fourier transform (FFT) algorithm. This lack of fidelity in scattering strength reconstruction does not have a discernible degrading effect on the quality of image reconstructed as will be illustrated below, but is important and must be dealt with when quantitative analysis of scattering strengths is needed.

If the frequency coverage is increased to ($f_1 = 6$ GHz, $f_{200} = 20$ GHz) with the number of sampling points being fixed to 200 and the pass-bands are kept at (f_{30} , f_{80}) and (f_{120} , f_{170}), the computed fields and the extrapolation errors would be as shown in Fig. 5. It is seen that the extrapolation error indicated by the dashed line becomes smaller. If the frequency coverage is decreased to ($f_1 = 6$ GHz, $f_{200} = 12$ GHz), the results would be as shown in Fig. 6. It is seen that the extrapolation errors indicated by the dashed and dotted curves are now both high. The FFT of the whole band data, pass-band data only, and the extrapolated plus pass-band data using this method are shown in Figs. 6(b) to 6(d) respectively. The results in Figs. 5 and 6 indicate the desirability of using segmented spectral data spanning wider spectral ranges.

The performance of the algorithm using realistic data is also evaluated. The test object, a metalized 100:1 scale model of a B-52 aircraft with 79 cm wing span and 68 cm long fuselage was mounted on a computer-controlled elevation-over-azimuth positioner situated in an anechoic chamber environment. 201 equal frequency steps covering the $f_1 = 6.1$ to $f_{201} = 17.5$ GHz range were used to obtain the frequency response of the object as described in [1]. The target is positioned for a fixed elevation angle of 30° while the azimuth angle was altered between 0° and 90° in steps of 0.7° for a total of 128 angular looks.

The pass-band is first defined as (f_{30}, f_{80}) and (f_{120}, f_{170}) . The measured values and the extrapolated errors of the broad-side look which is 90° from the head-on look are shown in Fig. 7(a). The solid line curve is the amplitude of the range-phase corrected field (see [1]). The dashed curve represents the extrapolation error resulting from extrapolating from each single band (bands I, II) with model order 25 as described in step 1 of the proposed algorithm. The dotted line curves are obtained using the new algorithm with 1 iteration and model order 25. The extrapolation error for measurement is defined in a manner similar to the definition of error in numerical simulation as the magnitude of the difference between the corrected measured fields and extrapolated fields. The Fourier transform from the whole band data, the pass-band data only, and the pass-band together with extrapolated data are shown in Figs. 7(b), 7(c) and 7(d) respectively. Fourier transform of the corrected scattered fields will give the range profile of the target in that view. In this figure, it is seen that the extrapolation errors do not improve after one iteration. The reason can be explained from the plot of the range profile shown in Fig. 7(b). In this view direction, the major contributions to the scattered fields are due to fuselage and primarily those engines and fuel tank which are on the illuminated side. Specular scattering from these points are well separated in time or distance and their number is small. Hence the linear prediction parameters obtained from single pass-band are sufficient to model the data sequence. The extrapolation errors are not as small as those obtained by simulations. The reason of this is that the applicability of linear prediction model to the extrapolation of scattered fields of a metallic object is based on the high

frequency approximation. In the measurement data, however, polarization effects, edge diffraction, multiple scattering and the failure to satisfy the high frequency approximation in the lower region of the frequency band utilized in the measurement will degrade the performance of the algorithm.

The reconstructed images of the test object using data collected in an angular windows of 90° extending from head-on to broadside in 128 looks (see [1] for detail) and different frequency bands are shown in Fig. 8. The transmitting antenna is right-hand circularly polarized and the receiving antenna is left-hand circularly polarized, which constitutes by the convention given in [7] a co-polarized transmitting/receiving system. Figure 8(a) is obtained by using the whole band data; Fig. 8(b) is obtained by using the pass-band data alone. Figures 8(c) and 8(d) are obtained by extrapolating without iteration and after one iteration respectively. The model order used is $M = 25$ in both cases.

If the pass-band is defined as (f_{65}, f_{130}) , the reconstructed images obtained by using the pass-band data alone and by extrapolation without iteration and after 1 iteration are shown in Figs. 8(e), 8(f), and 8(g) respectively. The model order used is also $M = 25$.

It is seen that the image quality of Figs. 8(c) and 8(e) are as good as that of Fig. 8(a). These results show the effectiveness of the application of the proposed algorithm to radar imaging from segmented data bands.

V. CONCLUSION

A new method employing the Burg algorithm and an iterative procedure to extrapolate observed data beyond restricted regions of observation has been proposed and tested. Simulation and experimental results prove the effectiveness of this proposed method. The algorithm is especially effective when the spectra of the collected data (the object range profile in this case) are in discrete form. Possible applications of this new method can be found in diverse fields whenever the data is available in restricted bands. For example, in multiple band microwave imaging system, the quality of the image obtained by extrapolating from a much

smaller bandwidth can be as good as that obtained by data in the full bandwidth. The cost of the imaging system can hence be reduced drastically as the cost of the required gear can be much lower than the cost of the gear to cover the full bandwidth and restrictions on use of frequency bands can be accommodated.

ACKNOWLEDGEMENT

This research was supported by the Air Force Office of Scientific Research, Air Force system Command, under grant AFOSR-81-0240F and by the Army Research Office under contract DAAG 29-83-K-0120-P02.

REFERENCE

- [1] N.H. Farhat, C.L. Werner and T.H. Chu, "Prospects for Three-Dimensional Projective and Tomographic Imaging Radar Networks," *Radio Science*, Vol. 19, No. 5, pp. 1347-1355, 1984.
- [2] R.W. Gerchberg, "Super-Resolution Through Error Energy Reduction," *Optica Acta*, Vol. 21, No. 9, pp. 708-720, 1974.
- [3] Yoshiaki Yamakoshi and Takuso Sato, "Iterative Image Restoration From Data Available in Multiple Restricted Regions," *Applied Optics*, Vol. 21, No. 24, pp. 4473-4480, 1982.
- [4] C.Q. Lan, K.K. Xu and Glen Wade, "Limited Angle Diffraction Tomography and Its Application to Planar Scanning Systems," *IEEE Trans. on Sonics and Ultrasonics*, Vol. SU-32, No. 1, pp. 9-16, 1985.
- [5] Steven M. Kay and Stanley Lawrence Marple, "Spectrum Analysis - A Modern Perspective," *Proc. of the IEEE*, Vol. 69, pp. 1380-1419, November 1981.
- [6] Burg, John P., "A New Analysis Technique for Time Series Data", NATO Advanced Study Institute on Signal Processing with Emphasis on Underwater Acoustics, pp. 12-23, August 1968.
- [7] G. T. Ruck, *et al.*, *Radar Cross Section Handbook*, edited by G. T. Ruck, Chapter 8, Plenum Press, New York 1970.
- [8] Jon Mathews and R.L. Walker, *Mathematical Methods of Physics*, 2nd Ed., W.A. Benjamin, Inc., Menlo Park, California, 1970.

FIGURE CAPTIONS

Fig. 1 Available data in multiple regions. Passband(shaded region) surrounded by vacant bands.

Fig. 2 Schematic diagram of the proposed new iterative extrapolation method.

Fig. 3 Geometry of the scattering measurement system.

Fig. 4 (a) Magnitude of theoretical fields and comparison of extrapolation errors of different methods, $f_1 = 6$ GHz, $f_{200} = 16$ GHz.

—— magnitude of theoretical fields.

----- extrapolation error from a single passband, no iteration.

..... extrapolation errors from new iterative algorithm.

_____ extrapolation errors from algorithm proposed in [3].

(b) FFT of the whole band data.

(c) FFT of the passband data.

(d) FFT of the passband and extrapolated data with 1 iteration.

(e) FFT of the passband and extrapolated data using algorithm proposed in [3].

Fig. 5 Magnitude of theoretical fields and comparison of extrapolation errors with and without iteration, $f_1 = 6$ GHz, $f_{200} = 20$ GHz.

—— magnitude of theoretical fields.

----- extrapolation error from respective passband, no iteration.

..... extrapolation errors from new iterative algorithm.

Fig. 6 (a) Magnitude of theoretical fields and comparison of extrapolation errors with and without iteration, $f_1 = 6$ GHz, $f_{200} = 12$ GHz.

———— magnitude of theoretical fields.

----- extrapolation error from respective passband, no iteration.

..... extrapolation errors from new iterative algorithm.

(b) FFT of the whole band data.

(c) FFT of the passband data.

(d) FFT of the passband and extrapolated data with 1 iteration.

Fig. 7 (a) Magnitude of the measured fields and comparison of extrapolation errors without and with 1 iteration

———— magnitude of theoretical fields.

----- extrapolation error from respective passband, no iteration.

..... extrapolation errors from new iterative algorithm.

(b) FFT of the whole band data.

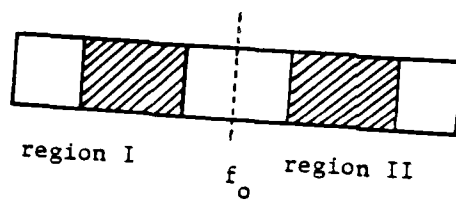
(c) FFT of the passband data.

(d) FFT of the passband and extrapolated data with 1 iteration.

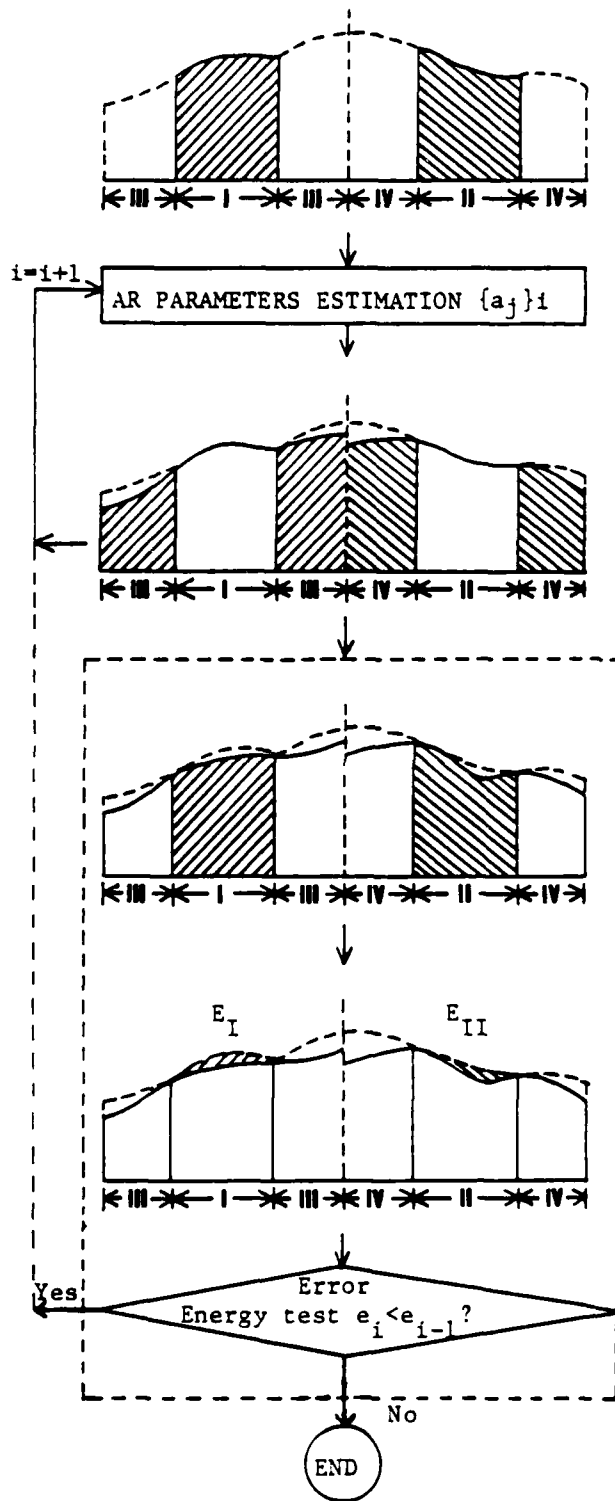
Fig. 8 Reconstructed images of the metalized scale model B-52 aircraft using an angular window of 90° extending from head-on to broad-side in 128 looks and different spectral coverage.

Reconstructions from:

- (a) entire bandwidth (f_1, f_{201}).
- (b) passband (f_{30}, f_{80}), (f_{120}, f_{170}).
- (c) passband (f_{30}, f_{80}), (f_{120}, f_{170})
and extrapolation data (extrapolated data into empty bands) without iteration.
- (d) passband (f_{30}, f_{80}), (f_{120}, f_{170})
and extrapolation data with 1 iteration.
- (e) passband (f_{65}, f_{130}).
- (f) passband (f_{65}, f_{130}) and extrapolation data without iteration.
- (g) passband (f_{65}, f_{130}) and extrapolation data with 1 iteration.



ITERATION ALGORITHM



1. Available data in regions I & II are used to extrapolate into regions III & IV.
2. Use data in regions I + II + III + IV to estimate the parameters $\{a_j\}_i$, where i represents the iteration number.
3. Use data in I and $\{a_j\}_i$ to extrapolate into region III. Use data in II and $\{a_j\}_i$ to extrapolate into region IV.

Convergence Test

- a. Use data in III and $\{a_j\}_i$ to estimate new data values in region I. Use IV and $\{a_j\}_i$ to estimate new data values in region II.
- b. Calculate error

$$e_i = E_I + E_{II}$$
- c. For the resultant data is in step 3: If $e_i < e_{i-1}$, $i+1 \rightarrow i$, go from step 3 to 2 otherwise iteration stopped.

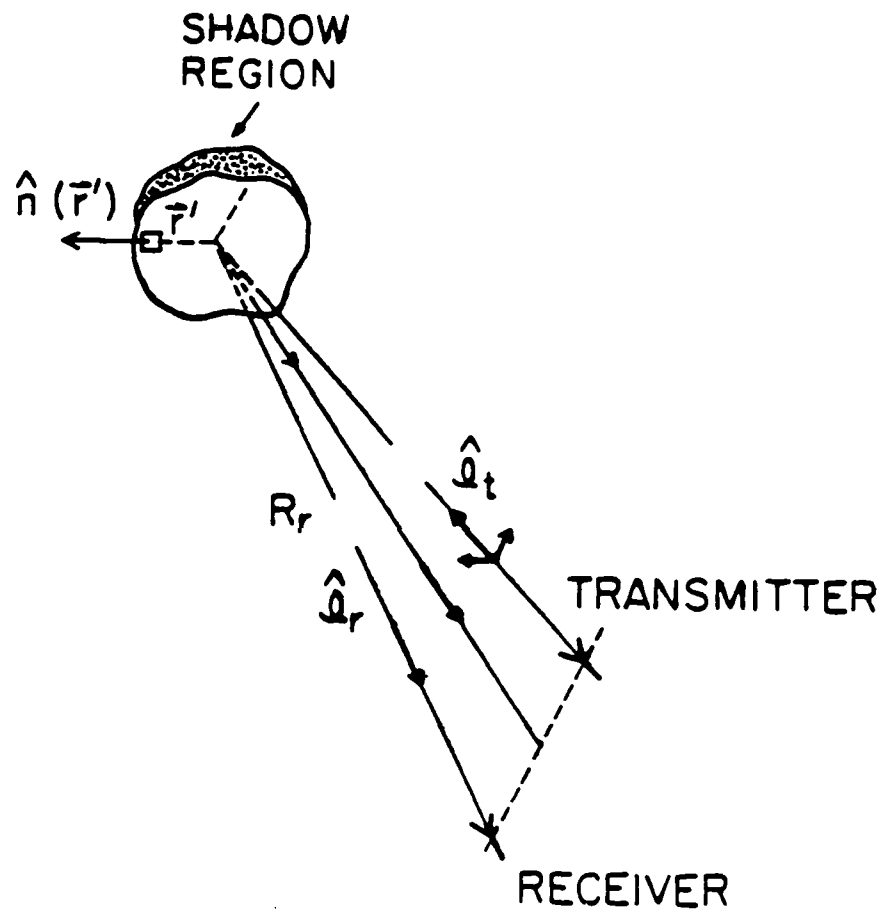
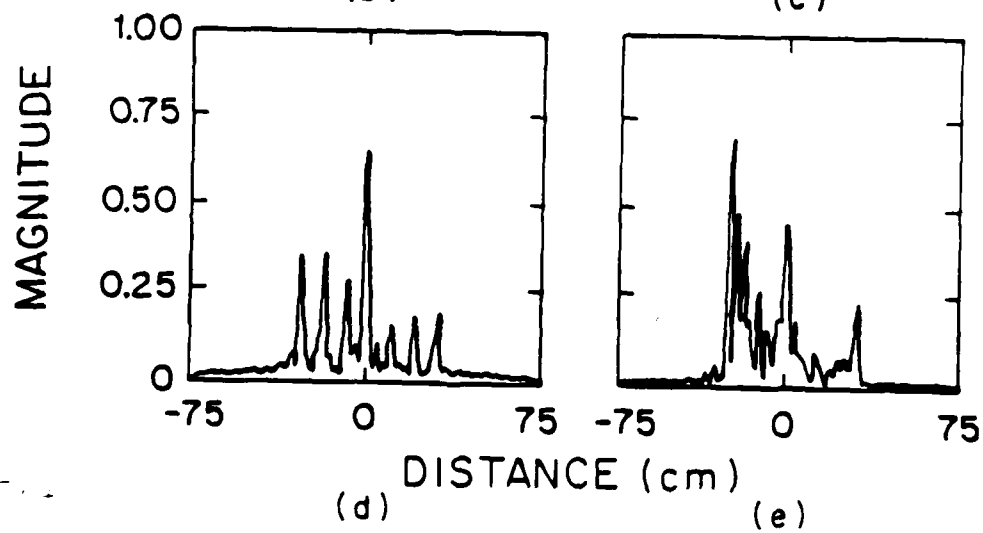
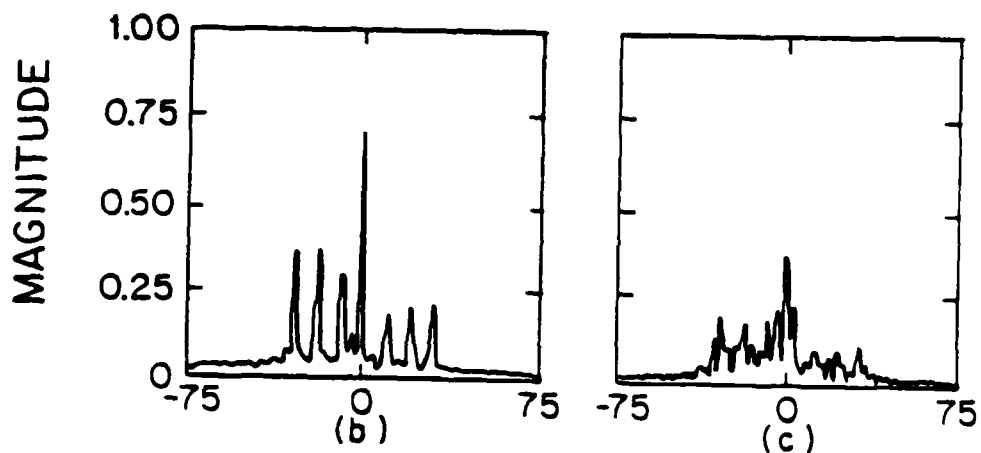
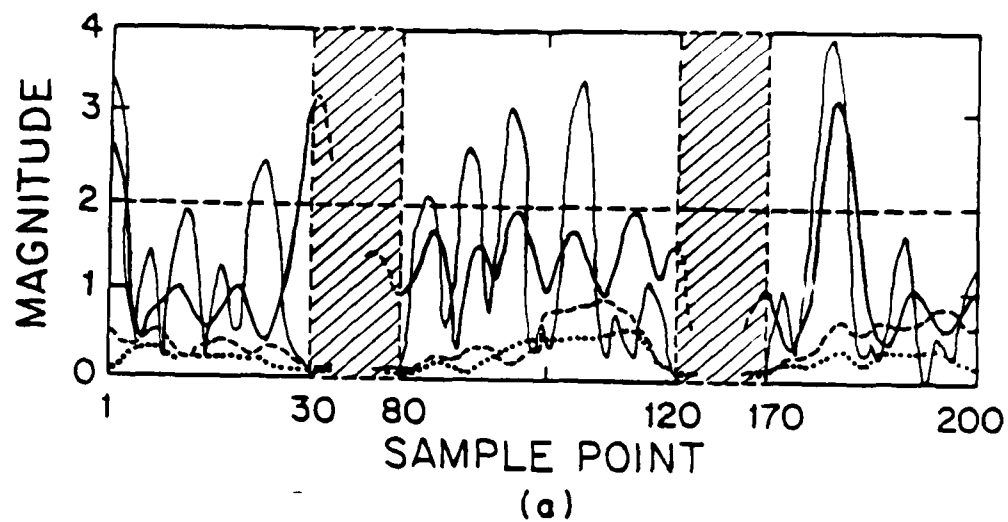


Fig 3



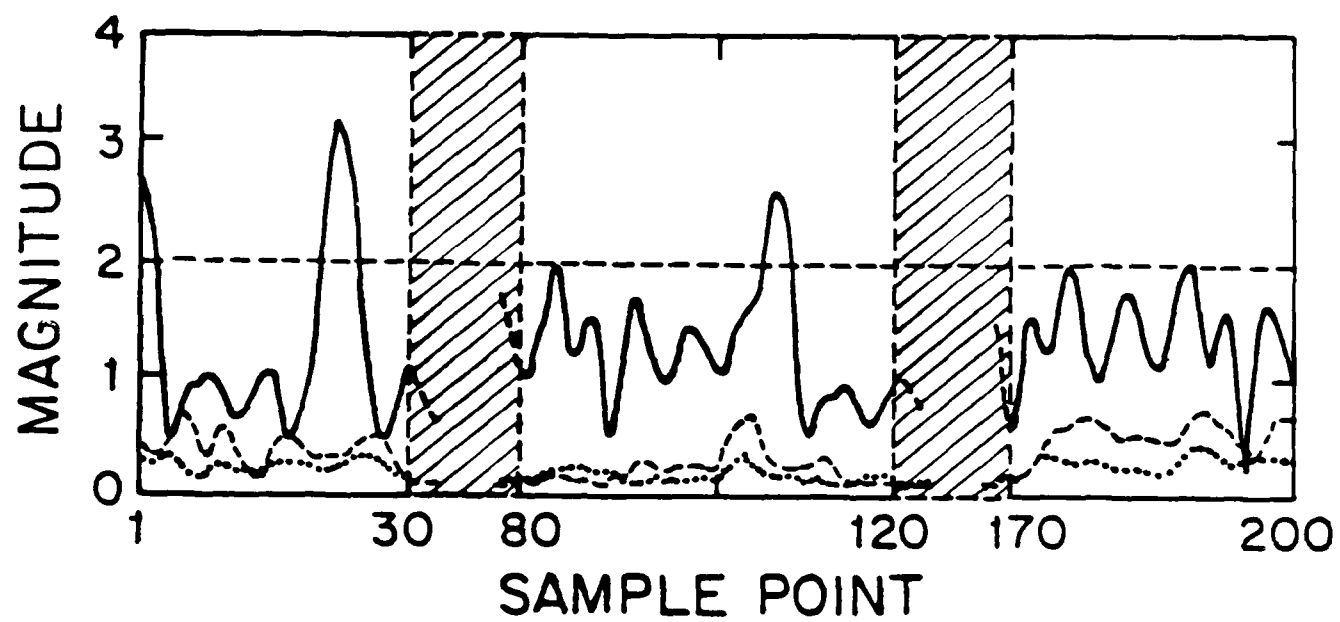
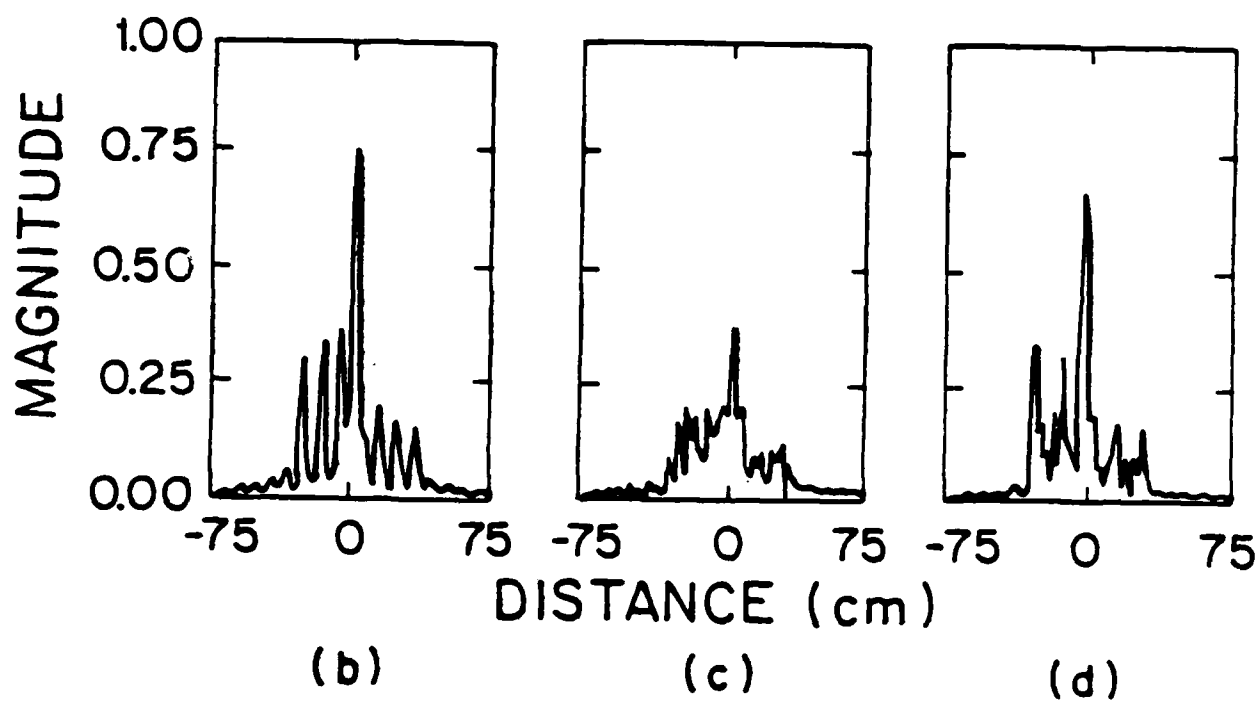
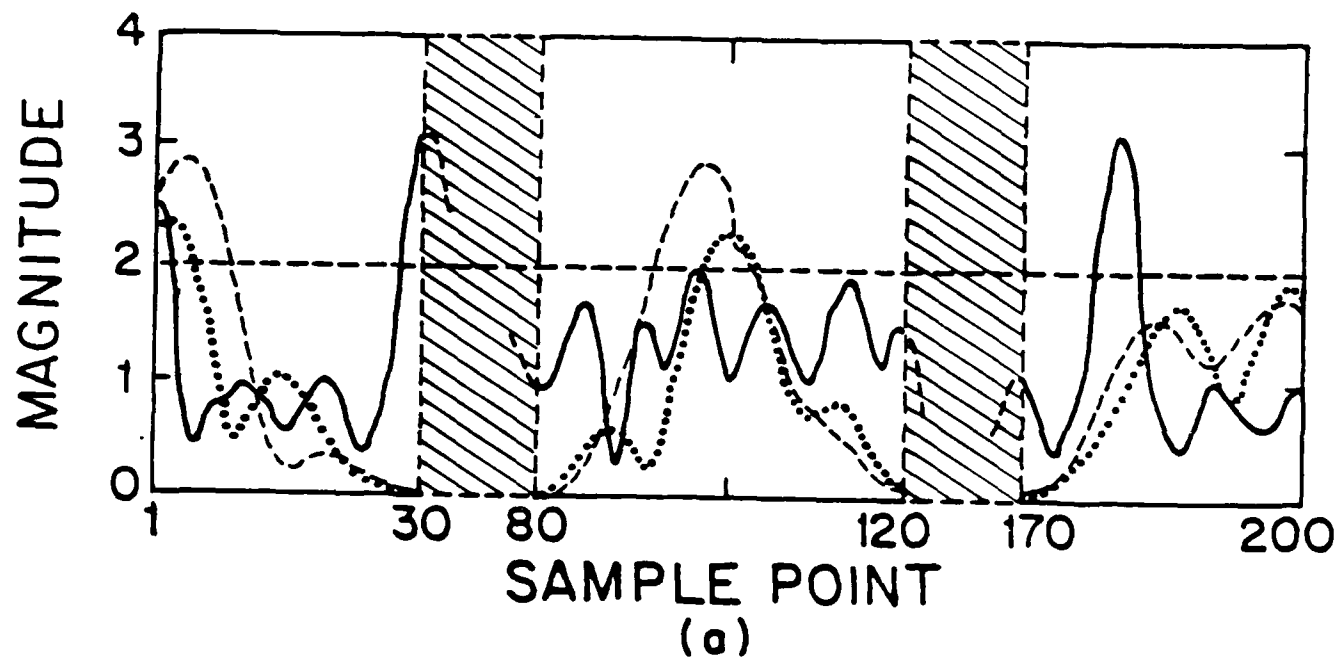
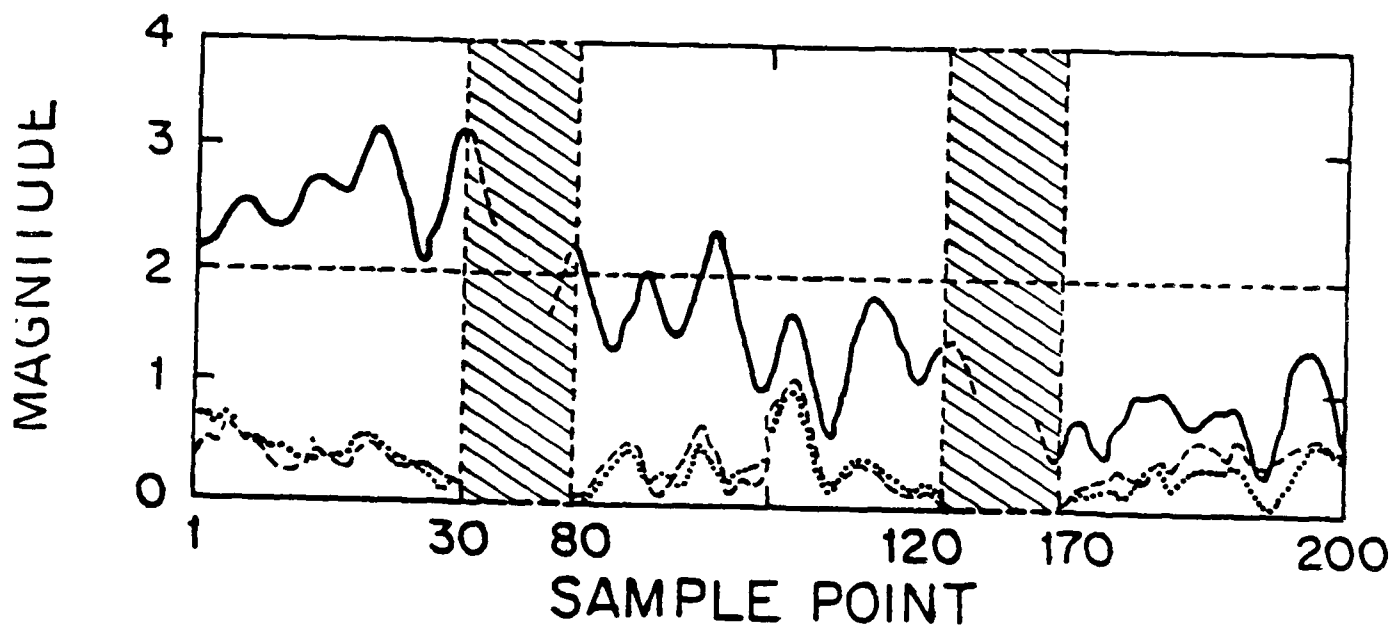
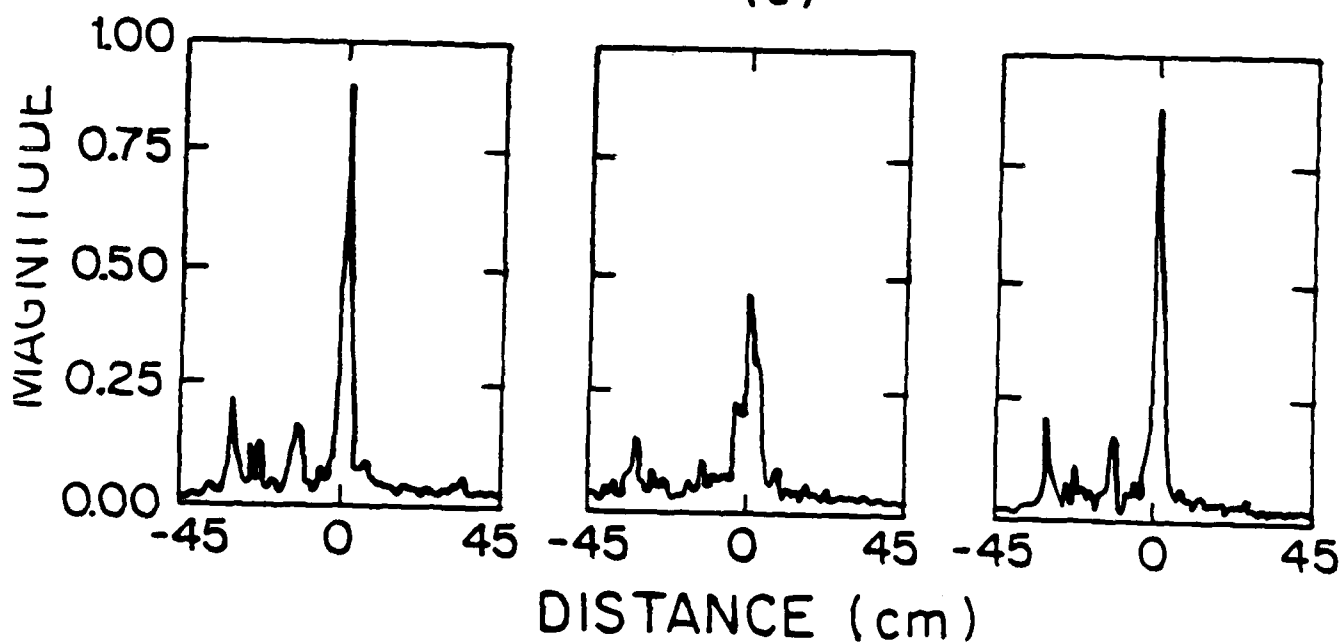


Fig 5





(a)



(b)

(c)

(d)



(a)



(b)



(c)



(d)



(e)



(f)



(g)

APPENDIX VI

ARCHITECTURES FOR OPTO-ELECTRONIC ANALOGS OF SELF-ORGANIZING NEURAL NETWORKS

Nabil H. Farhat
University of Pennsylvania
Electrical Engineering Department
Electro-Optics and Microwave-Optics Laboratory
Philadelphia, PA 19104-6390

Abstract

Architectures for partitioning opto-electronic analogs of neural nets into input/output and internal units to enable self-organization and learning where a net can form its own internal representations of the "environment" are described.

1. INTRODUCTION: In our preceeding work on optical analogs of neural nets, [1],[2], the nets described were programmed to do a specific computational task, namely a nearest neighbor search by finding the stored entity that is closest to the address in the Hamming sense. As such the net acted as a content addressable associative memory. The programming was done by computing first the interconnectivity matrix using an outer-product recipe given the entities we wished the net to store and become familiar with followed by setting the weights of synaptic interconnections or links between neurons accordingly.

In this paper we are concerned with architectures for opto-electronic implementation of neural nets that are able to program or organize themselves under supervised conditions, i.e., of nets that are capable of (a) computing the interconnectivity matrix for the associations they are to learn, and (b) of changing the weights of the links between their neurons accordingly. Such self-organizing networks have therefore the ability to form and store their own internal representations of the entities or associations they are presented with.

Multi-layered self-programming nets have been described recently [3]-[5] where the net is partitioned into three groups. Two are groups of visible or external input/output units or neurons that interface with the outside world i.e., with the net environment. The third is a group of hidden or internal units that separates the input and output units and participates in the process of forming internal representations of the associations the net is presented with, as for example by "clamping" or fixing the states of the input and output neurons to the desired associations and letting the net run through its learning algorithm to arrive ultimately at a specific set of synaptic weights or links between the neurons that capture the underlying structure of all the associations presented to the net. The hidden units or neurons prevent the input and output units from communicating with each other directly. In other words no neuron or unit in the input group is linked directly to a neuron in the output group and vice-versa. Any such communication must be carried out via the hidden units. Neurons within the input group can communicate with each other and with hidden units and the same is true for neurons in the output group. Neurons in the hidden group can not communicate with each other. They can only communicate with neurons in the input and output groups as stated earlier.

Two adaptive learning procedures in such partitioned nets have attracted considerable attention. One is stochastic involving a **simulated annealing** process [6],[7] and the other is deterministic involving an **error back-propagation** process [4]. There is general agreement however; that because of their iterative nature, serial digital computation of the links with these algorithms is very time consuming. A faster means for carrying out the required computations is needed. Never-the-less the work mentioned represents a milestone in that it opens the way for powerful collective computations in multilayered neural nets and in that it dispels earlier reservations [8] about the capabilities of early models of neural nets such as the Perceptron [9] when the partitioning concept is introduced. What is most significant and noteworthy, in our opinion, is the ability to now define buffered input and output groups with unequal number of neurons in a net which was not possible with earlier nets where all neurons participate in defining the initial (input) and final (output) states of the net.

2. ANALOG IMPLEMENTATIONS: Optics and opto-electronic architectures and techniques can play an important role in the study and implementation of self-programming networks and in speeding-up the execution of learning algorithms. We have done some exploratory work in this regard to see how the neurons in an opto-electronic analog of a neural net can be partitioned into groups with specific interconnection patterns. Here, for example, a method for partitioning an opto-electronic analog of a neural net into input, output, and internal units with the selective communication pattern described earlier to enable, stochastic learning, i.e., carrying out a simulated annealing learning algorithm in the context of a Boltzmann machine formalism is described. (see Fig. 1(a)). The arrangement shown in Fig. 1(a) derives from the neural network analogs we described earlier [2]. The

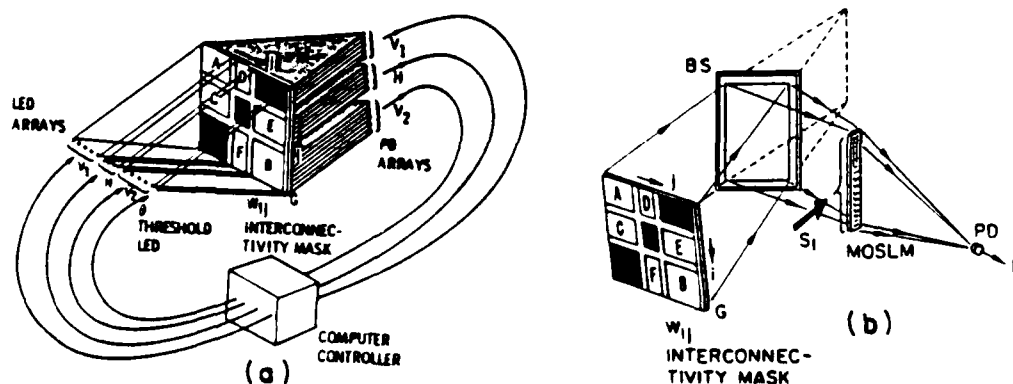


Fig. 1. Partitioning concept (a) and method for rapid determination of the net's energy E.

network, consisting of say N neurons, is partitioned into three groups. Two groups, V_1 and V_2 , represent visible or exterior units that can be used as input and output units respectively. The third group H are hidden or internal units. The partition is such that $N_1 + N_2 + N_3 = N$ where subscripts 1, 2, 3 on N refer to the number of neurons in the V_1 , V_2 and H groups respectively. The interconnectivity matrix, designated here as W_{ij} , is partitioned into nine submatrices, A, B, C, D, E, and F plus three zero matrices shown as blackened or opaque regions of the W_{ij} mask. The LED array

represents the state of the neurons, assumed to be unipolar binary LED on = neuron firing, LED off = neuron not-firing. The W_{ij} mask represents the strengths of interconnection between neurons in a manner similar to earlier arrangements [2]. Light from the LEDs is smeared vertically over the W_{ij} mask with the aid of an anamorphic lens system (not shown in Fig. 1(a)) and light emerging from rows of the mask is focused with the aid of another anamorphic lens system (also not shown) onto elements of the photodetector (PD) array. Also we assume the same scheme utilized in [2] for realizing bipolar values of W_{ij} in incoherent light is adopted here, namely by separating each row of the W_{ij} mask into two subrows and assigning positive values W_{ij}^+ to one subrow and negative values W_{ij}^- to the other, then focusing light emerging from the two subrows separately onto pairs of adjacent photosite connected in opposition in the V_1 , V_2 and H segment of the photodetector array. Submatrix A with $N_1 \times N_1$ elements, provides the interconnection weights of units or neurons within group V_1 . Submatrix B with $N_2 \times N_2$ elements, provides the interconnection weights of units within V_2 . Submatrices C (of $N_1 \times N_3$ elements) and D (of $N_3 \times N_1$ elements) provide the interconnection weights between units of V_1 and H and submatrices E (of $N_2 \times N_3$ elements) and F (of $N_3 \times N_2$) provide the interconnection weights of units of V_2 and H. Units in V_1 and V_2 can not communicate with each other directly because locations of their interconnectivity weights in the W_{ij} matrix or mask are blocked out (blackened lower left and top right portion of W_{ij}). Similarly units within H do not communicate with each other because locations of their interconnectivity weights in the W_{ij} mask are also blocked out (center blackened square of W_{ij}). The LED element θ is always on to provide a fixed or adaptive threshold level to all other units by contributing to the light focused onto only negative photosites of the photodetector (PD) arrays.

By using a computer controlled nonvolatile spatial light modulator to implement the W_{ij} mask in Fig. 1(a) and including a computer/controller as shown the scheme can be made self-programming with ability to modify the weights of synaptic links between its neurons to form internal representations of the associations or patterns presented to it. This is done by fixing or clamping the states of the V_1 (input) and V_2 (output) groups to each of the associations we want the net to learn and by repeated application of the simulated annealing procedure with Boltzmann, or other, stochastic state update rule and collection of statistics on the states of the neurons at the end of each run when the net reaches thermodynamic equilibrium.

For each clamping of the V_1 and V_2 units to one of the associations, annealing is applied, starting from an arbitrary W_{ij} , with switching states of units in H until thermodynamic equilibrium is reached. The state vector of the entire net, which represents a state of global energy minimum, is then stored by the computer. This procedure is repeated for each

association several times recording the final state vectors every time. The probabilities P_{ij} of finding the i -th and j -th neurons in the same state are then obtained. Next with the output units V_2 unclamped to let them free run like the H units the above procedure is repeated for the same number of annealings as before and the probabilities P'_{ij} are obtained. The weights W_{ij} are then incremented by $\Delta W_{ij} = \eta(P_{ij} - P'_{ij})$ where η is a constant that controls the speed and efficacy of learning. Starting from the new W_{ij} the above procedure is repeated until a steady W_{ij} is reached at which time the learning procedure is complete. Learning by simulated annealing requires calculating the energy E of the net [3],[5]. A simplified version of a rapid scheme for obtaining E opto-electronically is shown in Fig. 1(b). A slight variation of this scheme that can deal with the bipolar nature of W_{ij} would actually be utilized. This is not detailed here because of space limitation.

3. REMARKS: The partitioning architecture described is extendable to multilayered nets of more than three layers and to 2-D arrangement of neurons. Learning algorithms in such layered nets lead to multivalued W_{ij} . Therefore high-speed computer controlled SLMs with graded pixel response are called for. Methods of reducing the dynamic range of W_{ij} or for allowing the use of W_{ij} with ternary weights are however under study to enable the use of commercially available nonvolatile SLM devices that are mostly binary e.g., Litton's MOSLM.

4. ACKNOWLEDGEMENT: The work reported was supported by grants from DARPA/NRL, The Army Research Office, and the University of Pennsylvania Laboratory for Research on the Structure of Matter.

REFERENCES:

1. Psaltis, D. and N. Farhat, Digest of the 13-th Congress of Intern. Commiss. on Optics, ICO-13, Saporro, Japan, 1984. Also, Opt. Lett., Vol. 10, pp. 98-100, 1985.
2. Farhat, N.H., et. al., App. Optics, Vol. 24, pp. 1469-1475, 1985.
3. G.F. Hinton, et. al., Carnegie-Mellon University Report No. CMU-CS-84-119, May (1984).
4. D.E. Rumelhart, G.E. Hinton and R.J. Williams, Institute for Cognitive Science Report 8506, Univ. of California, San Diego, Sept. 1985.
5. T.J. Sejnowski and C.R. Rosenberg, Johns Hopkins University, Electrical Engineering and Computer Science Technical Report No. JHU/EECS-96/01 (1986).
6. N. Metropolis, et. al., J. Chem. Phys., Vol. 21, 6, pp. 1087-1092, June, 1953.
7. S. Kirkpatrick, et. al., Science, Vol. 220, pp. 671-680, May 1983.
8. M.L. Minsky and S. Papert, Perceptrons, MIT Press, Cambridge, MA, (1969).
9. F. Rosenblatt, Principles of Neuro-Dynamics: Perceptions and the Theory of Brain Mechanisms, Spartan Books, Wash. D.C., 1962.

Phased Array Antenna Pattern Synthesis By Simulated Annealing

N.H. Farhat and B. Bai

ABSTRACT: A new procedure is described for optimum phased array synthesis. The synthesis is optimized by a simulated annealing process in which the energy function is directly related to the far field intensity of a phased array. Numerical simulation results are presented. A possible optical-digital hybrid implementation that can perform the required computation at higher speed than a pure digital implementation is discussed.

1 INTRODUCTION

For the synthesis of an antenna array with uniformly spaced elements it is well known that, if the current distribution function is not restricted, a Dolph-Chebyshev distribution function over the antenna gives rise to an optimum pattern which has the lowest sidelobe level for a specified mainbeam width [1]. However, if for the purpose of easy practical implementation, the distribution function is restricted to some specific set, other methods have to be investigated and used for optimum synthesis. The simulated annealing method presented here is, by our study, one of the choices for optimum synthesis of phased arrays with restricted distribution functions. The synthesis is optimal in the sense that the lowest sidelobe level is achieved while the specified mainbeam width is maintained. This method can be used for both microwave phased arrays and optical arrays. In our study so far, we have been mainly concerned with optical arrays, which appear to be technologically feasible with present electronic and

*The authors are with the Electro-Optics and Microwave Optics Laboratory, the Moore School of Electrical Engineering, University of Pennsylvania, Philadelphia, PA 19104.

optical technologies. Hence, the parameters assumed in the simulations below are relevant to the optical case, but the method and conclusions apply to phased arrays in general.

2 SIMULATED ANNEALING METHOD

Metropolis *et al.* introduced the simulated annealing algorithm for calculating the properties of any system of interacting individual molecules [2]. The algorithm was previously applied to combinatorial optimization problems, including physical design of computers, and the traveling salesman problem [3]. The method can be extended for general optimization problems. For the system to be optimized, an "energy" or "cost" function E is first established and a dynamic variable T , the "temperature" of the system, is chosen to control the process. Starting at a high "temperature", the system is slowly cooled down, until the system "freezes" and reaches the optimum state in a manner similar to annealing of a crystal during growth to reach a near perfect structure. At each "temperature", a change in the system is made according to a certain rule, and then the "energy" or "cost" change of the system ΔE is calculated. If $\Delta E \leq 0$, the system alteration is retained and the process is continued. The acceptance or rejection of the alteration or change of grain of the system when $\Delta E > 0$ is treated probabilistically. Accordingly, the Boltzman factor $f(\Delta E) = \exp(-\frac{\Delta E}{KT})$ is calculated, where K is a constant whose dimension depends on the dimensions of ΔE and T . Then a random number R uniformly distributed in the interval $[0, 1)$ is chosen. If $R \leq f(\Delta E)$, the change of grain is retained; on the other hand, if $R > f(\Delta E)$, the change is discarded, that is, the system before change is used for the next step of the process. This procedure is repeated for each "temperature" until the system is optimized by arriving at a global energy minimum. The choices of K and the initial T are crucial for the success and speed of convergence of simulated annealing process. Because of the probabilistic Boltzman selection rule of the $\Delta E > 0$ case, the process can always get out of a local minimum of the "energy" or "cost" function in which it could get trapped and proceed to the desired global minimum. This makes simulated annealing different from iterative improvement procedure [3]-[6].

3 PHASED ARRAY SYNTHESIS

For a 2-dimensional phased array with $(2M+1) \times (2N+1)$ identical subapertures, the far field is the product of its subaperture factor and its array factor. The array factor can be written as,

$$Q(f_x, f_y) = \sum_{m=-M}^M \sum_{n=-N}^N W_{mn} \exp[-j2\pi(mAf_x + nBf_y)] \quad (1)$$

where, A and B are the spacing between elements in an orthogonal array coordinate; $f_x = \frac{x}{\lambda R_0}$, $f_y = \frac{y}{\lambda R_0}$, x and y being the transverse far field coordinates, and R_0 is the distance between point (x, y) and the array origin.

Since the subaperture factor is fixed for a given subaperture function and it varies much more slowly than the array factor, the effect of the subaperture factor is insignificant and hence ignored in the present synthesis. The array factor $Q(f_x, f_y)$ will be studied by changing the weighting factor W_{mn} for all possible m and n to achieve the optimum radiation pattern.

The "energy" or "cost" function in simulated annealing can be established in many different ways for phased array synthesis. Since our primary work is done for optical and infrared phased arrays and this kind of array has a relatively large size compared to the wavelength λ used (λ on the order of 10^{-6} m), the beam width is very small (on the order of 10^{-2} degrees). It is important to achieve the lowest sidelobe level. For this purpose, one obvious way to choose the "energy" or "cost" function for phased array synthesis would be the energy outside a specified main lobe. When this energy function is minimized, under the assumption that the total energy remains constant, it could be expected that the energy would become concentrated in the main beam. Consequently, the relative sidelobe level could be minimized. However, from simulations we have run, it turns out that this energy constraint cannot minimize the sidelobe level, since minimizing the energy does not necessarily constrain the peak sidelobe level. In the simulation presented here, the intensity E associated with the highest sidelobe level is used as the "energy" or "cost" function for simulated annealing. Of course, if necessary, a constraint about the beamwidth could be included in the "energy" or "cost" function. When the "energy" is minimized, the relative sidelobe level is now also minimized. The beamwidth at the final run will be taken as the optimum beamwidth associated with the final W_{mn} .

weights. The relationship of beamwidth and sidelobe level is then optimum in the sense of Dolph-Chebyshev, that is, the sidelobe level is the lowest for the given beamwidth.

4 SIMULATION

Since the simulated annealing process is the same for a 2-dimensional array as for a 1-dimensional array and considering the limited computation power of the MICRO PDP-11 computer available for our simulation, a 1-dimensional array is used in our study. The 1-dimensional array is also assumed to be a continuous one with many desired pixels. Each of the pixels acts as a subaperture. The simulation starts with a uniform distribution (all subapertures with 1 or -1). The far field pattern is shown in Fig.1(a) for this uniform distribution case and has the usual $-13.3(dB)$ sidelobe level. The distribution function is restricted to the set of 1, -1 , which means real transmittance with binary phase (phase = 0 or π) modulation. Then, simulated annealing is carried out by just changing the sign of each subaperture in turn, calculating the intensity of the highest sidelobe and applying the algorithm for each change. At each "temperature" for the simulated annealing algorithm, if either the number of accepted changes on randomly selected elements exceeds $\frac{1}{8}$ of the total subaperture numbers or the number of attempts exceeds 10 times the total subaperture numbers, the process goes to the next lower "temperature". If the desired number of acceptances is not achieved at three successive "temperatures", the process is considered "frozen" and the optimum pattern is attained. The final optimum result is given in Fig.1(b). This simulation is done for an array of 41 subapertures. The subaperture size is assumed to be equal to the spacing A between subapertures and is taken to be 61λ (figure relevant for optical arrays). The element distribution function that gives the final optimum result is shown in table 1. This function is seen to be asymmetric. From formula (1) it is seen that two elements with opposite index, say $n = -10$ and $n = 10$ for the 1-dimensional case, have different phases and therefore their contributions to the far field factor are different. In general, the array factor given in formula (1) is a complex quantity. Although it is frequently thought that the optimum array factor is real, there seems to be no reason to exclude a complex quantity as an optimum

array factor. Even if the array factor is a complex quantity and asymmetric, it can be shown that the far field (power) pattern is symmetric for arrays with real weights. In our simulation, the weights are real (1 or -1) and the pattern in Fig.1(b) is therefore symmetric. The distribution function in table 1 for the optimum pattern shown in Fig.1(b) is for elements -18, -15, and -12 with weights equal to -1; if we make elements +18, +15, and +12 also with weights equal to -1, which gives a symmetric array factor, the pattern obtained will be that shown in Fig.1(c) and is seen not to be optimum. From the simulation, it is found that the result of the simulated annealing procedure is relatively robust for different initial distribution functions, that is, it eventually gives the same optimum pattern for different initial distribution functions, as long as the initial distribution function forms a pattern with a single main beam. The final weighting function in table 1 was obtained from a uniform initial distribution function (all weights= 1) and it is interesting that switching of weights happens for only a few elements (three). The function in table 1 gives an optimum pattern only for broad side direction. Like the Dolph-Chebyshev optimum function, the optimum function given by simulated annealing is different for different steering angles, but an optimal weight distribution can be computed for each steering angle. From the simulation result, it is seen that the optimum far field pattern has similar features to the pattern given by the Dolph-Chebyshev distribution function. In the Dolph-Chebyshev pattern, all the sidelobes have the same level for a specified beamwidth. A numerical example in [1] shows an 8-element array (element separation $d = 0.5\lambda$) with 25.8(dB) sidelobe level and 40.8° beamwidth. The optimum pattern given by our simulation shows nearly equal level side lobes which are minimized for the given beamwidth.

5 DISCUSSION

Simulated annealing is a modification of the iterative improvement algorithm [4]. It is physically more meaningful and can be computed more systematically than the iterative improvement [4]. Physically, the simulated annealing process is analogous to the cooling of atoms in crystal growth: careful annealing produces a defect-free crystal, rapid annealing produces a defective crystal or glass [3]. The probabilistic treatment with the probability function $P(\Delta E) = \exp(-\frac{\Delta E}{KT})$

provides a way to accept the unfavorable changes and is easy to compute. From our simulation, it has been found that the simulated annealing algorithm seems always to give better performance than the iterative improvement algorithm.

Since simulated annealing is a modified iterative improvement process, it takes a relatively long time to do an optimization problem just as iterative improvement does in a computer calculation. The phased array synthesis in our simulation runs for one hour or so for an array of 41 elements on a MICRO PDP-11 computer. Finding an efficient scheme to reduce the excessive amounts of computer time on most optimum problems has always been of concern [5]-[7]. Otherwise, if enough computation power is available, iterative improvement can be run from random starts for many times to approach the optimum state. Fast opto-digital computing schemes similar to those described in [8] may also be considered for phased array synthesis by simulated annealing. It is understood that the far field is the Fourier transform of the array distribution function. An optical lens can be used for computing the Fourier transform as the distribution function is inputted to the front focal plane of the lens via, for example, an appropriate computer driven spatial light modulator (SLM). The Fourier transform in the back focal plane can be recorded and fed to the computer/controller to make the simulated annealing decision. The outcome is feedback to the SLM to change the distribution function in the front focal plane. The hybrid opto-digital scheme will do the Fourier transform instantly. In this fashion the computation associated with the Fourier transform can be virtually eliminated assuming a high speed SLM and computer interface are utilized. An opto-electronic Boltzman machine for accelerating the selection rule has also been proposed earlier in [8]. This process can be repeated for every step in simulated annealing. Also, a Cauchy probability selection rule, instead of the Boltzman selection rule, can be used to speed up the whole annealing process further [7].

6 ACKNOWLEDGEMENT

This work was supported by DARPA/NRL and with partial support from the Air Force Office of Scientific Research and the Army Research Office.

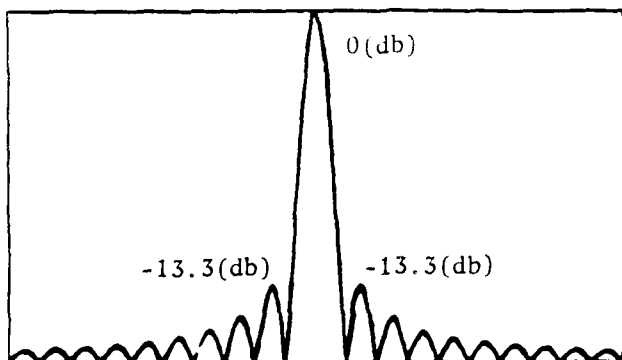
References

- [1] C. L. Dolph, "A current distribution for broadside arrays which optimizes the relationship between beam width and side-lobe level", *Proc. IRE.* 34, pp.335-348, June 1946.
- [2] N. Metropolis, *et al.*, "Equation of state calculations by fast computing machines", *J. Chem. Phys.* 21, pp.1087-1092, June 1953.
- [3] S. Kirkpatrick, *et al.*, "Optimization by simulated annealing", *Science* 220, pp.671-680, May 1983.
- [4] W.E. Smith, *et al.*, "Reconstruction of objects from coded images by simulated annealing", *Opt. Let.* 8, pp.199-201, April 1983
- [5] B. Dunham, "Design by natural selection", *Synthese* 15, pp.254-258, 1963.
- [6] S. Lin, "Heuristic programming as an aid to network design", *Network* 5, pp.33-43, 1975
- [7] H. Szu, "Fast Simulated Annealing with Cauchy Probability Density", *Neural Networks for Computing Conference*, Snowbird, Utah, April 1986
- [8] H. Barrett, *et al.*, "Optical Boltzman Machines", Post-deadline paper, *OSA Topical Meeting on Optical Computing*, Incline Village, NEV. (1985)

ELEMENT	-20	-19	-18	-17	-16	-15	-14	-13	-12	-11	-10	-9	-8	-7	-6	-5	-4	-3	-2	-1	0	1	2	3	4	5	6	7	8	9	10	11	12	13	14	15	16	17	18	19	20
WEIGHT	1	1	-1	1	1	-1	1	1	-1	1	1	1	1	1	1	1	1	1	1	1	1	1	1	1	1	1	1	1	1	1	1	1	1	1	1	1	1	1	1	1	1

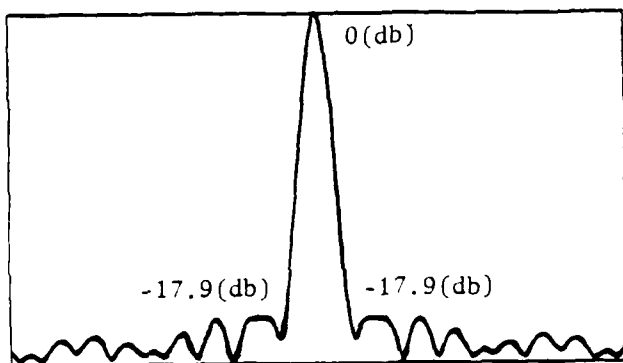
Table 1. The Final Distribution Function Weights for the Optimum Pattern

Fig. 1. Simulated annealing result. (a) Far field pattern for the uniform distribution; (b) Pattern obtained by simulated annealing; (c) Pattern obtained from a symmetrized version of the weights distribution obtained by simulated annealing.



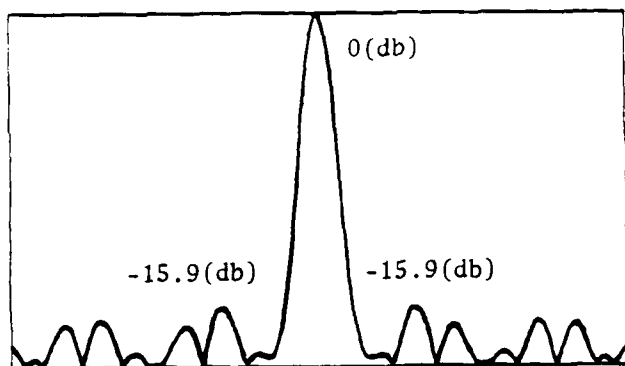
(a)

mainbeam width: 4.58×10^{-2} (degree)
view range: [-3, 3] (degree)



(b)

mainbeam width: 5.5×10^{-2} (degree)
view range: [-3, 3] (degree)



(c)

mainbeam width: 7.7×10^{-2} (degree)
view range: [-3, 3] (degree)

FILMED
5-8